



# THE UNIVERSITY *of* EDINBURGH

This thesis has been submitted in fulfilment of the requirements for a postgraduate degree (e.g. PhD, MPhil, DClinPsychol) at the University of Edinburgh. Please note the following terms and conditions of use:

- This work is protected by copyright and other intellectual property rights, which are retained by the thesis author, unless otherwise stated.
- A copy can be downloaded for personal non-commercial research or study, without prior permission or charge.
- This thesis cannot be reproduced or quoted extensively from without first obtaining permission in writing from the author.
- The content must not be changed in any way or sold commercially in any format or medium without the formal permission of the author.
- When referring to this work, full bibliographic details including the author, title, awarding institution and date of the thesis must be given.

**THE UNIVERSITY *of* EDINBURGH**  
**School of Engineering**  
**Institute for Materials and Processes**



**Thin Polymer Films of Block Copolymers and  
Blend/Nanoparticle Composites**

**Michail Kalloudis**

**A thesis submitted to the University of Edinburgh, for the  
Degree of Doctor of Philosophy**

**February 2013**

In memory of my uncle Amvrosios

## Declaration

I declare that this thesis has been composed by myself and is all my own work except where otherwise stated.

---

Michail Kalloudis

February 2013



## Acknowledgements

During the long period that I have worked on this thesis there have been many people that have assisted me along the way. I would like to take the opportunity to acknowledge in this part the individuals that have made the difference during this time. This work would have not been possible without their help, guidance and support.

First and foremost, I would like to thank my principal supervisor Dr. Vasileios Koutsos, Reader at the School of Engineering, The University of Edinburgh. During my 4 years of studies, he has offered me both his expert advice and encouragement as I have overcome technical issues and experimental frustration. Vasileios was always next to me, giving me advice and guidance not only in the academic field, but also in the life outside academia. Without doubt his help has been crucial in the completion of this thesis.

It would have been almost impossible to write this thesis, without the scientific inspiration and guidance, as well as the experimental support of Dr. Emmanouil Glynos, Post-Doctoral Research Fellow in the Department of Materials Science and Engineering, University of Michigan. Our 4 years of collaboration proved very helpful to fulfil a very demanding project. Despite of the distance issue, his ideas and advice were very effective.

I am also very grateful to my collaborator Dr. Paul Clegg, Senior Lecturer in the School of Physics, The University of Edinburgh, for his excellent and unlimited guidance and suggestions to both theoretical and experimental parts of my thesis. During the 2 and half years of collaboration, he was always there to provide me with

a detailed feedback on my manuscripts, experiments and reports. I strongly believe that his contribution to writing this thesis is exceptional.

I am very thankful to Dr. John Walker, who helped me with the training on the atomic force microscope (AFM). He dedicated plenty of his valuable time to share all his knowledge and experience on the AFM. Everything I know about this machine started from Dr. John Walker.

The exceptional support of Dr. Andrea Hamilton, Director of the materials laboratories in Edinburgh University and Jim Hutcheson, technician in the materials laboratories, should also be acknowledged. They were always next to me providing guidance, problem solutions and new ideas during my life in the laboratories.

I feel very thankful also, to my colleagues and friends Miss Julia Morris, Mr. Ibrahim Ahmed Albaijan, Miss Ares Gomez, Mr. Danié Orezon, Miss Olga Kapetanou, Mr. Pedro Saenz, Mr. Tom Barraclough, Mr. Tamas Parkanyi, Ms Samantha Ela, Dr. Jovana Radulovic, Dr. Gerasimos Skouvaklis, Dr. Anne Hansen and Dr. Eirini Theofanidou for their endless support in scientific and personal issues. I would also like to thank my colleague and best friend Dr. Apostolos E.A.S. Evangelopoulos. The combination of his scientific support and our strong friendship helped me overcome many problems in my academic and personal life. I feel very lucky having a friend and a colleague in a person like Apostolos.

Furthermore, I am very grateful to my collaborators outside the University of Edinburgh. Dr. Stergios Pispas from the National Hellenic Research Foundation in Greece provided me with the main substance of my experiments for Chapter 3, the

diblock copolymers. Apart from this, meetings and discussions with Dr. Pispas proved very useful for the completion of this thesis. In addition, I would like to thank Dr. Alex Winkel from JPK Instruments (Berlin, Germany) for his help with the QI™ mode AFM measurements and for his willingness to help me with many of the AFM-related issues related to the experiments with the JPK instrument. Furthermore, I feel very grateful to Prof. Joachim Loos and his PhD student Mr. Marco Bigatti from the School of Physics, Glasgow University for their valuable help on the transmission electron microscopy (TEM) technique. Marco in particular proved an excellent collaborator, performing the TEM experiments in accordance with my guidance and suggestions in the laboratories of School of Physics in the University of Glasgow. He was more than willing to answer all my questions and respond to all to my experimental demands.

I would also like to thank my girlfriend Miss Evangelia Athanasiou, MSc graduate from the School of Engineering, The University of Edinburgh, for her endless love, help and patience she showed to me all this time.

Finally and most importantly I would also like to thank my family. My father Philippos, my mother Eleni, my grandmother Filia, my sister Erifili, her fiancé Romain Tanzer, my aunt Stavriana and my uncle Georgios for their unconditional love and support, even though this meant that we had to be apart for such long period of time. When things were becoming really difficult, my family was always next to me helping me stand up and move on.

For funding me during my PhD, many thanks go to the Institute for Materials and Processes, School of Engineering, The University of Edinburgh.

## Abstract

In this thesis, atomic force microscopy (AFM), transmission electron microscopy (TEM) and optical microscopy techniques were used to investigate systematically the self-assembled nanostructure behaviour of two different types of spin-cast polymer thin films: poly(isoprene-*b*-ethylene oxide), PI-*b*-PEO diblock copolymers and [poly(9,9-dioctylfluorene-*co*-benzothiadiazole)]:poly[9,9-dioctylfluorene-*co*-N-(4-butylphenyl)-diphenylamine], F8BT:TFB conjugated polymer blends. In the particular case of the polymer blend thin films, the morphology of their composites with cadmium selenide (CdSe) quantum dot (QD) nanoparticles was also investigated. For the diblock copolymer thin films, the behaviour of the nanostructures formed and the wetting behaviour on mica, varying the volume fraction of the PEO block ( $f_{\text{PEO}}$ ) and the average film thickness was explored. For the polymer blend films, the effect of the F8BT/TFB blend ratio (per weight), spin-coating parameters and solution concentration on the phase-separated nanodomains was investigated. The influence of the quantum dots on the phase separation when these were embedded in the F8BT:TFB thin films was also examined.

It was found that in the case of PI-*b*-PEO copolymer thin films, robust nanostructures, which remained unchanged after heating/annealing and/or ageing, were obtained immediately after spin coating on hydrophilic mica substrates from aqueous solutions. The competition and coupling of the PEO crystallisation and the phase separation between the PEO and PI blocks determined the ultimate morphology of the thin films. Due to the great biocompatible properties of the PEO

block (protein resistance), robust PEO-based nanostructures find important applications in the development of micro/nano patterns for biological and biomedical applications.

It was also found that sub-micrometre length-scale phase-separated domains were formed in F8BT:TFB spin cast thin films. The nanophase-separated domains of F8BT-rich and TFB-rich areas were close to one order of magnitude smaller (in the lateral direction) than those reported in the literature. When the quantum dot nanoparticles were added to the blend thin films, it was found that the QDs prefer to lie in the F8BT areas alone. Furthermore, adding quantum dots to the system, purer F8BT and TFB nano-phase separated domains were obtained. Conjugated polymer blend thin films are excellent candidates for alternatives to the inorganic semiconductor materials for use in applications such as light emitting diodes and photovoltaic cells, mainly due to the ease of processing, low-cost fabrication and mechanical flexibility. The rather limited optoelectronic efficiency of the organic thin films can be significantly improved by adding inorganic semiconducting nanoparticles.

# Table of Contents

Dedication .....	ii
Declaration .....	iii
Acknowledgements .....	iv
Abstract .....	vii
Table of Contents .....	ix
Chapter 1 Introduction .....	1
Chapter 2 Basics of Polymers on Surfaces, Polymer Blends, AFM and TEM.....	6
2.1 General Aspects of Polymers on Surfaces .....	7
2.2 Thermodynamics of Polymer Mixtures .....	9
2.2.1 Flory-Huggins Solution Theory .....	11
2.3 Introduction to Atomic Force Microscopy .....	13
2.4 Contact Mode AFM .....	15
2.5 Tapping Mode AFM .....	16
2.6 Phase Imaging AFM .....	17
2.7 Amplitude Imaging AFM .....	17
2.8 Force Spectroscopy .....	17
2.9 Limitations of AFM .....	20
2.10 Introduction to Transmission Electron Microscopy .....	21
2.10.1 Mass-thickness contrast .....	22
2.10.2 Bright Field Contrast.....	23
2.10.3 Limitations of TEM .....	23
2.11 References.....	24
Chapter 3 Diblock Copolymer Nanostructures Self-Assembled on Mica.....	27

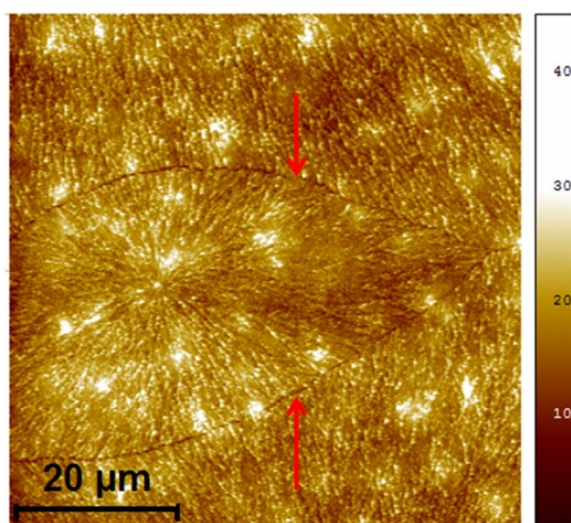
3.1	Introduction.....	28
3.2	Background.....	29
3.3	Experimental.....	34
3.3.1	Materials and Characterization .....	34
3.3.2	Sample Preparation and AFM measurements .....	36
3.4	Results and Discussion .....	39
3.4.1	Monolayer Formation on Mica .....	42
3.4.2	Thicker Areas: Cone-Like Lamellae and Crystalline Lamellae.....	48
3.5	Conclusions.....	55
3.6	References.....	59
Chapter 4	Thin Films of Conjugated Polymer Blends.....	66
4.1	Introduction.....	67
4.2	Background.....	69
4.2.1	Semiconductor Materials and Light Emitting Diodes.....	69
4.2.2	Conjugated Polymers .....	71
4.2.3	Polyfluorene-Based Conjugated Polymer Blends.....	74
4.3	Experimental.....	83
4.3.1	Materials.....	83
4.3.2	Polymer Solutions and Thin Films Preparation .....	83
4.3.3	Atomic Force Microscopy.....	85
4.3.4	Transmission Electron Microscopy .....	86
4.4	Results.....	86
4.4.1	F8BT:TFB Polymer Blends with concentration 20 mg/ml.....	87
4.4.2	F8BT:TFB Polymer Blend thin films from concentration 14 mg/ml ..	92
4.5	Discussion.....	101

4.5.1	Thin film nano-phase separation: effect of spin coating, annealing and concentration parameters .....	107
4.5.2	Lateral Size Transition of the Phases from F8BT:TFB with 1:2 to 1:4 by weight blend ratio.....	109
4.6	Conclusions.....	110
4.7	References.....	113
Chapter 5	Thin Films of Conjugated Polymer Blend-Nanoparticle Composites	117
5.1	Introduction.....	118
5.2	Background.....	120
5.2.1	Inorganic Nanoparticles and Quantum Dots .....	124
5.2.2	Mixing Nanoparticles with Conjugated Polymer Blends for Solar Cell and LED production.....	127
5.2.3	F8BT:TFB Polymer Blends mixed with Quantum Dots to Produce Composite Thin Films for use in Semiconducting Devices.....	131
5.3	Experimental.....	137
5.3.1	Materials.....	137
5.3.2	Inorganic Nanoparticle - Polymer Solutions.....	138
5.3.3	Ultra-Thin-Film Preparation .....	140
5.3.4	Atomic Force Microscopy.....	141
5.3.5	Transmission Electron Microscopy .....	143
5.4	Results and Discussion .....	144
5.4.1	CdSe Quantum Dots on Mica .....	144
5.4.2	F8BT and TFB thin films mixed with QDs .....	145
5.4.3	Thin films of F8BT:TFB polymer blends mixed with 3 different weight ratios of CdSe quantum dots. ....	147
5.4.4	CdSe Quantum Dots Detection in F8BT:TFB thin films.....	157



5.5	Conclusions.....	171
5.6	References.....	175
Chapter 6	General Conclusions and Future Work.....	180
6.1	General Conclusions .....	181
6.1.1	Diblock Copolymer Nanostructures Self-Assembled on Mica.....	181
6.1.2	Thin Films of Conjugated Polymer Blends.....	181
6.1.3	Thin Films of Conjugated Blend-Nanoparticle Composites.....	182
6.2	Future Work.....	182
6.2.1	Diblock Copolymer Nanostructures Self-Assembled on Mica.....	182
6.2.2	Thin Films of Conjugated Polymer Blends.....	183
6.2.3	Thin Films of Conjugated Blend-Nanoparticle Composites.....	183
6.3	References.....	185
Appendices A & B & C	.....	186
Appendix A:	Further Images and Height Profiles.....	187
Appendix B:	Cross-Section Analysis of TFB thin film .....	196
Appendix C:	Publications, Talks and Presentations based on PhD .....	197

## Chapter 1 Introduction



AFM topography image of poly(isoprene-*b*-ethylene oxide) PI-*b*-PEO thin film spin cast on mica. Colour-scale is in nanometres. Red arrows in the inset indicate the crystal boundaries. (Kalloudis *et al.* Langmuir, 2013, 29, 2339-2349).

Polymer thin films have many uses in a wide range of industrial, biomedical and micro/nano-electronic applications. Polymer-based thin films are in fact a part of our daily lives due to their presence in paints, coatings, packaging, adhesives, dielectrics and in many other applications. At the same time the continuing expansion of polymer thin films into new technologies and applications has attracted the interest of scientists to further investigate their properties and responses to various interfaces [1] and intermixing with other inorganic materials [2].

More precisely, polymer blends and block copolymer thin films can be tailored to exhibit specific mechanical, optical, electric and chemical properties. For example functional surfaces have been produced using polymer blend and diblock copolymer films, which may serve as templates for nanolithography [3] or in biomedical field [4]. Furthermore, in the rapidly growing field of polymer electronics, optoelectronic properties of polymer films (mainly blends of polymers) have been investigated and the first devices have appeared on the market [5].

Polymer blends and block copolymers form various nano-structures or nano-patterns on surfaces via the process of self-assembly. Self-assembly is a breakthrough technique as a manufacturing method in nanotechnology. In polymer self-assembly the desired structural morphology is a consequence of the properties of the molecules that are used. Conversely, in conventional techniques such as lithography, the desired structure must be separated from a larger block of matter. In general, self-assembly manufacturing (or so called “bottom-up”) is an excellent alternative to lithography (or so called “top-down”) due to lower costs, easier processing and faster production of materials in larger quantities [6].

In this thesis we study the self-assembled structural morphology at the nano-scale produced by a diblock copolymer and polymer blends on surfaces. To investigate the nano-structures we exploited the imaging capabilities (at the molecular scale) of atomic force microscopy (AFM). We also use other techniques such as transmission electron microscopy (TEM) and optical microscopy.

This work has been divided in the following chapters and appendices:

In **Chapter 2**, some general aspects of polymers on surfaces and polymer blends are presented and the experimental techniques of atomic force and transmission electron microscopy are described.

In **Chapter 3**, we study the nanostructure morphology of a series of amphiphilic semi-crystalline poly(isoprene-*b*-ethylene oxide) diblock copolymers with various block fractions spin cast on mica from aqueous solutions. We used atomic force microscopy to reveal the effect of the different block lengths on the nanostructural evolution; both near and away from the mica surface.

In **Chapter 4**, AFM and TEM are used to investigate the morphology of low molecular weight conjugated polymer-blend spin-cast thin films. The polymers are: F8BT (poly[9,9-dioctylfluorene-*co*-benzothiadiazole]) and TFB (poly[9,9-dioctylfluorene-*co*-N-(4-butylphenyl)-diphenylamine]). We consider the effect of the polymer blend ratio, annealing, spin-coating speed/time and the solution concentration on the lateral and vertical morphology of the phase separated domains at the nanoscale.

In **Chapter 5**, AFM and TEM techniques were used to investigate the structural morphology of the F8BT:TFB polymer blends mixed with inorganic nanoparticles, cadmium selenide quantum dots (CdSe QDs) for the first time. We investigated the dispersion of the quantum dots in the F8BT:TFB polymer matrix and surface and the effect of the QDs on the nanophase separation of the blends.

In **Chapter 6**, conclusions and plans for future work are presented.

Finally in **Appendices A & B & C**, we present some additional AFM images, height profiles for the systems studied (A & B) and the publications, talks and presentations came out of this thesis (C).

**References**

1. Liang G-D, Xu J-T, Fan Z-Q, Mai S-M, and Ryan AJ. *The Journal of Physical Chemistry B* 2006;110(48):24384-24389.
2. Colvin VL, Schlamp MC, and Alivisatos AP. *Nature* 1994;370(6488):354-357.
3. Cox JK, Eisenberg A, and Lennox RB. *Current Opinion in Colloid & Interface Science* 1999;4(1):52-59.
4. Khor HL, Kuan Y, Kukula H, Tamada K, Knoll W, Moeller M, and Hutmacher DW. *Biomacromolecules* 2007;8(5):1530-1540.
5. Burroughes JH, Bradley DDC, Brown AR, Marks RN, Mackay K, Friend RH, Burns PL, and Holmes AB. *Nature* 1990;347(6293):539-541.
6. Ulman A. *Chemical Reviews* 1996;96(4):1533-1554.

**Chapter 2 Basics of  
Polymers on Surfaces,  
Polymer Blends, AFM and  
TEM**



**AFM phase image of a symmetric poly(isoprene-*b*-ethylene oxide) PI-*b*-PEO thin film spin cast on mica (the size of the image is  $20 \times 20 \mu\text{m}^2$ ).**

## **2.1 General Aspects of Polymers on Surfaces**

Polymeric materials find widespread applications due to their adaptable properties, cost-efficiency and relatively simple production techniques. The science, which is dedicated to the synthesis of polymers, is able to almost fully control the structural behaviour of these materials in their bulk state. However, the situation becomes more complicated when the polymeric materials are transferred onto solid surfaces (polymer thin films). The interaction between the polymeric material and the substrate, along with the thickness of the polymeric film, leads to the formation of different structures compared with the structures in the bulk of the polymer [1]. The interactions and confinement effects of polymers when in the vicinity of solid surfaces constitute an important scientific field with consequences for technological fields such as nanotechnology, nano-electronics, biotechnology and biomedical applications.

Polymers, which are adsorbed onto a solid surface, or polymers, which are close to the surface, exhibit interesting properties. Polymers on surfaces are great candidates for use in colloidal stabilization [2], nanoscale surface patterning [3], friction modification [4], DNA microarrays [5] and adhesion [6]. There are two basic ways that the polymers can be attached on the substrate: chemisorption (i.e. anchoring with chemical bonds, grafting – strong interactions) or physisorption, where the chains of the polymer and the surface interact with van der Waals forces (weak interaction). The physisorption and the resulting conformational relaxation of the polymer chain are driven by the competition between the entropic repulsion and the drop in energy from binding monomers to the substrate [7]. Several previous



studies have been focused on the thin film properties of polymer systems such as block copolymers [8], polymer blends [9] and end-grafted polymers [10,11].

Blending of polymers has been proved to be a cost-effective and easy processing technique for preparing materials with flexible applications. The physical properties of the blends on surfaces depend strongly on the resulting morphology on submicrometre length scales, sizes which can be difficult to characterise by conventional microscopy techniques. Furthermore, the morphologies of block copolymers and their blends in bulk and on solid surfaces has been an important subject of research over recent decades [12]. The mechanical properties of the polymer blends depend on their composition, morphology and interface structure. The blend morphology mainly depends on the interface parameters and the polymer composition [13]. Thus, in order to understand and control the phase separation, miscibility, adhesion, and interface phenomena of polymers, it is crucial to extensively investigate the nanometre-scale structures and morphologies of polymers and their blends. Transmission electron microscopy techniques (TEM) have been extensively and successfully applied in order to investigate the bulk and thin film morphology of the polymer blends and block copolymers [14]. However several limitations of the TEM technique have made atomic force microscopy (AFM) techniques the most popular imaging and characterisation tool in the science, which deals with the polymer on surfaces [15].

## 2.2 Thermodynamics of Polymer Mixtures

Mixing two polymers usually results in a system that exhibits a complete phase separation due to the repulsive forces between the compounds occurred by the chemical incompatibility between the polymers [16]. For complete mixing of two polymers the following condition is required:

$$\Delta G_m = \Delta H_m - T\Delta S_m < 0 \quad (2.1)$$

where  $\Delta G_m$ ,  $\Delta H_m$ , and  $\Delta S_m$  are the changes of the Gibb's free energy, the enthalpy and the entropy of mixing at given temperature  $T$ , respectively.

For one-phase stable systems of binary mixtures with composition  $\phi$  (in some cases, e.g. copolymers, also denoted by  $f$ ) at a given temperature  $T$  and pressure  $p$ , the criteria for phase stability are:

$$\Delta G_m < 0, \left( \frac{\partial^2 \Delta G_m}{\partial^2 \phi} \right)_{p, T} > 0 \quad (2.2)$$

Miscible, is a polymer blend which exhibits homogeneity at the molecular level and associated with the negative value of the free energy of mixing and the domain size is comparable to the dimensions of the macromolecular segment. The value of  $T\Delta S_m$  is always  $> 0$  since there is an increase in the entropy on mixing. Consequently, the  $\Delta G_m$  depends on the value of the enthalpy of mixing  $\Delta H_m$ . *The polymers mix to form a single phase only when the entropic contribution to free energy is higher than the enthalpic contribution:*

$$\Delta H_m < T\Delta S_m \quad (2.3)$$

In general, the miscibility of the polymer blends increases with the increase of the pressure. The effect depends on the enthalpy (or heat) of mixing  $\Delta H_m$ : when  $\Delta H_m < 0$ , the miscibility is increased by compression, while when  $\Delta H_m > 0$ , the miscibility is decreased.

Figure 2.1 presents a schematic phase diagram obtained from Utracki [16], highlighting the three regions with different degree of miscibility: a) the single-phase miscible region lying between the binodals, b) the four metastable (fragmented) regions between the binodals and the spinodals and c) the two phase-separated immiscible regions, lying over and below the spinodals. The diagram highlights also the two critical solution temperature points, the lower point (LCST) at higher temperature and the upper (UCST) at lower temperature. Phase diagrams with both the LCST and the UCST points usually refer to low molar mass mixtures. Phase diagrams of polymer blends usually show either LCST (most commonly) or UCST [16].

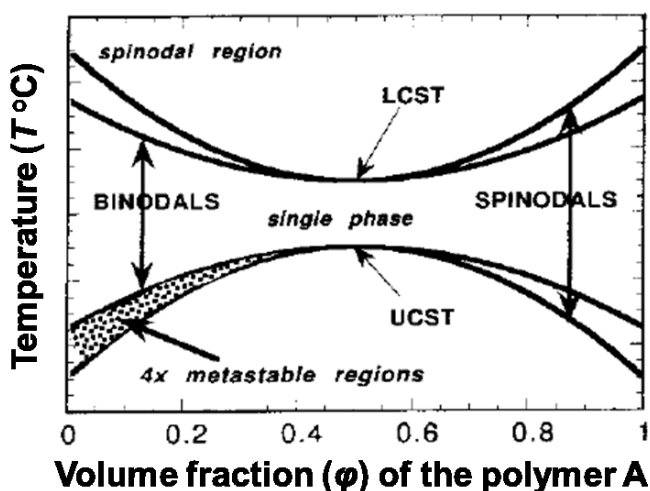


Figure 2.1 Phase diagram for liquid mixtures obtained from ref. [16], with the upper and the lower critical solution temperatures, UCST and LCST respectively.

The binodals, shown in Figure 2.1, separate the one-phase (miscible) and the metastable region, while the spinodals separate the metastable and the two phase-separated regions. The conditions for phase-separation are given by the following [16]:

$$\text{Spinodal:} \quad \left( \frac{\partial^2 \Delta G_m}{\partial^2 \phi} \right)_{p, T} = 0 \quad (2.4)$$

$$\text{Critical point:} \quad \left( \frac{\partial^2 \Delta G_m}{\partial^2 \phi} \right)_{p, T} = \left( \frac{\partial^3 \Delta G_m}{\partial^3 \phi} \right)_{p, T} \quad (2.5)$$

The phase-separation process occurs when a single-phase system suffers a change of composition or temperature or pressure that drives it to pass into either the metastable or the spinodal region. In the particular case, where the system enters from the single-phase to the metastable region, the phase separation occurs by the mechanism of slow *nucleation* followed by growth of the phase separated domains. In contrast, when the system jumps from a single-phase into the spinodal region of immiscibility the phases separate spontaneously by a mechanism called *spinodal decomposition* [16].

### 2.2.1 Flory-Huggins Solution Theory

Flory-Huggins solution theory [17, 18] is a simple mathematical model of thermodynamics, which deals with the polymer solutions. This model considers that no-change in the volume during mixing occurs ( $\Delta V_m = 0$ ), the entropy of mixing is given only by the number of re-arrangements during polymer mixing and that the enthalpy of mixing is caused by interactions of different segments. Given that this

theory is based on a mean-field model, only average interactions are taken into account. The main challenge was to find a better estimation for the entropy of mixing, as the polymer solutions exhibit substantial deviations from values expected for ideal solutions. This challenge was successfully overcome independently by Flory and Huggins using a cubic lattice model [17, 18].

According to Flory and Huggins, assuming random mixing of two polymers and  $\Delta V_m = 0$ , the entropy of mixing in polymer solutions is given by:

$$\Delta S_m = -R \left[ \frac{\varphi_1}{r_1} \ln \varphi_1 + \frac{\varphi_2}{r_2} \ln \varphi_2 + \chi \varphi_1 \varphi_2 \right] \quad (2.6)$$

where,  $\varphi$  is the volume fraction of the components in the solution,  $r$  is the number of polymer segments, which is proportional to the degree of polymerization  $N$  and  $R$  is the gas constant. As it can be seen from the eq. 2.6 the entropy of mixing is inversely proportional to the length of polymer components (degree of polymerisation).

Furthermore, the Flory-Huggins theory estimates that the enthalpy of mixing (considering nearest neighbour interactions between the two components) is given by:

$$\Delta H_m = RT\chi\varphi_1\varphi_2 \quad (2.7)$$

where,  $\chi$  is the so-called Flory-Huggins binary interaction parameter. A high positive  $\chi$  indicates a repulsive interaction between the polymers and leads to positive  $\Delta H_m$ , which tends to inhibit the solution process. On the other hand, a negative  $\chi$  implies an

attractive interaction and leads to negative  $\Delta H_m$ , which results in complete dissolution.

Finally, the free energy of mixing in the Flory-Huggins theory for binary systems is given by [19]:

$$\Delta G_m = RT \left[ \frac{\varphi_1}{r_1} \ln \varphi_1 + \frac{\varphi_2}{r_2} \ln \varphi_2 + \chi \varphi_1 \varphi_2 \right] \quad (2.8)$$

The first two terms in the eq. 2.8 are related to the entropy of mixing and the last term is related to the enthalpy of mixing.

### **2.3 Introduction to Atomic Force Microscopy**

In general, scanning probe microscopy (SPM) is a family of advanced techniques which are widely used for surface analysis [20]. The most versatile and most adaptable member of the SPM family is atomic force microscopy (AFM). The atomic force microscope was first reported by Binnig, Quate and Gerber of IBM in 1986 [21] and followed on from their work on scanning tunnelling microscopy (STM) [22], for which they were awarded the Nobel Prize for Physics [23]. It was suggested as a means of studying non-conducting surfaces on an atomic scale, combining the principles of the STM and a stylus profilometre, and imaging by effectively “feeling” the sample surface. AFM provides unparalleled topography, adhesion and mechanical sample details in the order of the sub-nanometre scale. Polymers on surfaces, a continuously expanding field of research from biotechnology to nano-electronics, have been extensively studied by AFM [15]. The ability to

manipulate the polymeric materials in the nanometre and molecular scales has increased the importance of AFM applications to polymer technology [15].

In the atomic force microscope the surface is scanned with a sharp tip, which is mounted on a miniature cantilever as shown in the schematic of the AFM in Figure 2.2. The tip is one of the AFM's most important parts, as it "touches" the surface, giving rise to the image through its force interaction with the specimen's surface. Usually the tips have a pyramidal shape. Typical pyramidal tips have pyramid height  $\sim 2 - 3 \mu\text{m}$  and  $\sim 30 - 50 \text{ nm}$  radius apex. The tip is important, as it the one which determines the capabilities of the system to provide atomic resolution analysis of the sample's surface.

The tip, which is mounted at the end of the cantilever, approaches and then touches the surface through a piezoelectric (piezo) cylinder the "z-scanner" as shown in Figure 2.2. The scanners in the AFM are made from piezoelectric materials, which expand and contract proportionally to an applied voltage. The sensitivity of the scanners depends on the piezo movement and on the piezo voltage. The deflection of the cantilever is monitored through an optical element. A laser beam is aligned to focus on the cantilever's end and is reflected from its top side onto a photodetector, which is capable of detecting movement of the tip in the atomic scale. The electronics of the system guide the tip to scan the study area through the  $x -$  and  $y -$  piezo ( $x y -$  scanner in Figure 2.2). Finally, the AFM images are recording the force interaction between the surface and the tip, during sample scanning. The whole scanning process is illustrated in Figure 2.2.

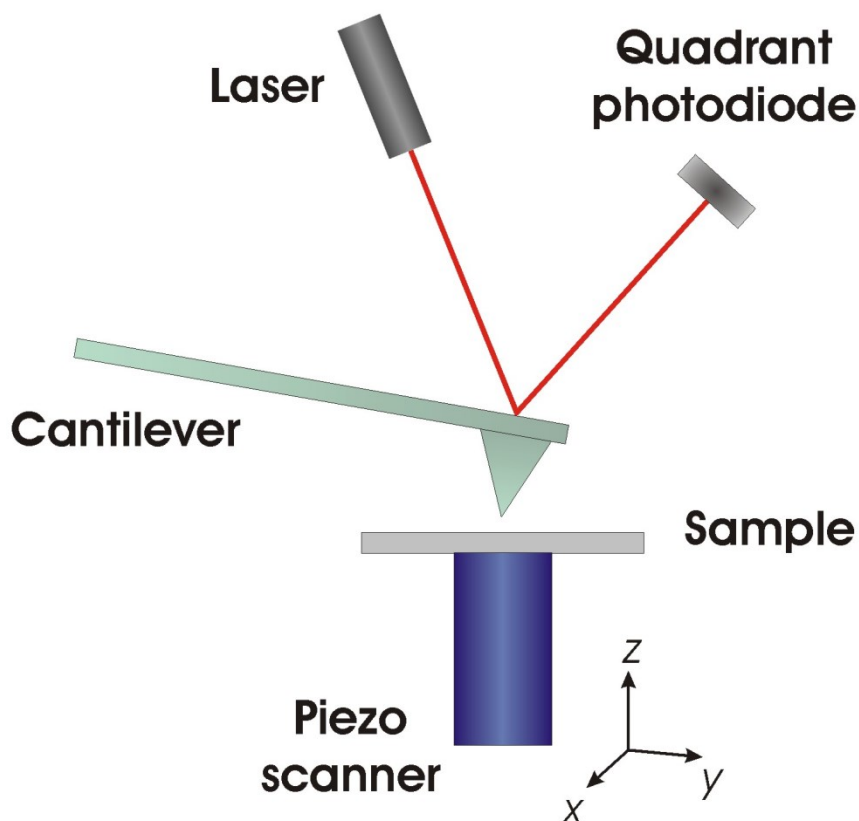


Figure 2.2 Schematic drawing of the AFM (obtained from Baclayon and co-workers [33]).

Typically the AFM works in two basic modes: *Contact mode*, where the tip apex is in continuous contact with the surface [15] and *tapping mode*, where the tip is in intermittent contact with the surface [24].

## 2.4 Contact Mode AFM

The contact mode, where the tip scans the sample in close contact with the surface, is the common mode used in atomic force microscopy. When using this mode the sample is driven in  $z$ -direction by the  $z$ -piezo, forcing the cantilever to be deflected. As soon as the surface reaches the tip, the deflection of the cantilever can be pre-specified through the electronics. This process is known as the instrument's



operating set-point. During scanning, if the measured deflection is different from the set-point (the tip meets objects on the surface), the feedback applies a signal to the piezo to raise or lower the sample relative to the cantilever to reinstate the desired value of deflection. The signal that the feedback applies to the piezo is a measure of the height of objects on the scanning surface. However, due to the constant contact of the tip with the surface, problems with the excessive tracking forces applied by the tip to the sample are likely to occur. For this reason, soft samples such as polymer surfaces are not best studied in contact mode.

## **2.5 Tapping Mode AFM**

The constant need to develop an AFM technique to avoid surface damage is one of the largest reasons for the development of tapping mode AFM [24]. In this mode, short, intermittent contacts between the tip and the surface minimize the deformation of the sample. During scanning, the cantilever vibrates at close to its resonance frequency [15] and moves in the direction of the sample to a distance smaller than its oscillation amplitude. During scanning, as soon as the tip reaches the sample's surface, the feedback will always try to keep the cantilever at constant amplitude. This constant amplitude can be defined by the system user and is called amplitude set-point ( $A_{sp}$ ). Consequently, when the tip meets an object the cantilever has a less space to oscillate, leading to a decrease in amplitude. On the other hand, when the tip meets a well-like structure, then it has more space to oscillate and the amplitude increases. In both situations, the feedback modifies the  $z$ -position of the piezo in order to maintain the cantilever amplitude at the user-defined set-point.

## **2.6 Amplitude Imaging AFM**

We have already mentioned in the Tapping mode of operation, the feedback loop tries to maintain the amplitude of oscillation constant adjusting the z-piezo. The voltage needed to keep the amplitude constant can be collected into an (error signal) image. The advantage of this imaging is that provides a high (sharp) contrast between the features on the studied film surface.

## **2.7 Phase Imaging AFM**

Phase imaging is a powerful extension of tapping mode AFM, which provides nanometre scale information about surface structure often not revealed by other scanning probe microscopy techniques. By performing phase mapping during a tapping mode scan, phase imaging goes beyond simple topographical mapping to detect variations in composition, adhesion, friction, viscoelasticity, and perhaps other properties. In phase imaging, the phase shift of the cantilever oscillation relative to the signal sent to the cantilever's piezo driver is simultaneously monitored and recorded by the AFM's controller. The phase shift is very sensitive to variations in material properties such as adhesion and viscoelasticity [25].

## **2.8 Force Spectroscopy**

Until now we have highlighted the high-resolution imaging capabilities of the AFM, but it is also a powerful tool for sensitive force measurements. The AFM tip is able to probe an extremely small interaction area and this gives it a high sensitivity to small forces. The cantilever that holds the tip acts as a very soft spring, which makes these forces accessible. These cantilevers are usually made of silicon or silicon

nitride  $\sim 100 - 200 \mu\text{m}$  long, allowing measurable forces at the scale of pico-Newtons. These forces are of the order of magnitude needed to break a hydrogen bond for example [26]. In general, the tip moves towards and away from the sample in the normal direction. The vertical position of the tip, along with the deflection of the cantilever, are recorded and converted to force-distance curves. The application of these experiments range from the nano-mechanical investigations of elastic properties to protein unfolding [27].

Figure 2.3 (left) presents a typical force-distance curve, consisting of the approach (dashed line) and the retrace (line) parts. In Figure 2.3 (right), the movement of the cantilever and the tip during the force-spectroscopy experiment is depicted. The cantilever approaches the surface from a starting ‘safe’ distance from the surface in order not to incur any interactions between the tip and the surface and the deflection of the cantilever does not change (region A in Figure 2.3). As the distance between the tip and the sample decreases, the cantilever starts to bend (jumps to contact), due to the van der Waals forces between the tip and the surface (region B in Figure 2.3). After the contact between the surface and the tip, the cantilever bends away from the surface, changing its deflection and giving rise to the straight line of the force-distance curve (region C in Figure 2.3). Subsequently, depending on the relative stiffness of the cantilever and depending also on the nature of the sample, the tip can indent or compress the surface. After the maximum approach, the cantilever then is withdrawn and a hysteresis might appear due to the attractive tip-surface interactions, such as adhesive forces (regions D, E in Figure

2.3). Finally, as the withdrawal continues, the tip loses contact with the surface and returns to its initial position (region F in Figure 2.3).

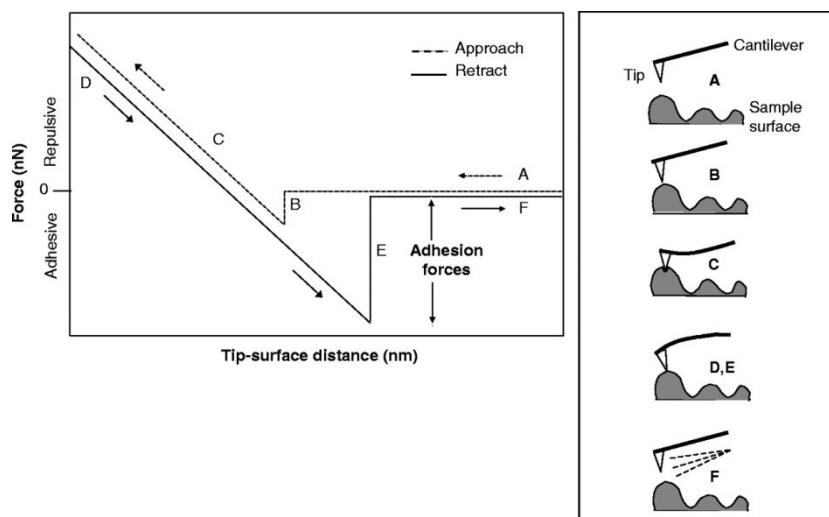


**Figure 2.3** “Idealized force-distance curve describing a single approach-retract cycle of the AFM tip, which is continuously repeated during surface scanning. The AFM tip is approaching the sample surface (A). The initial contact between the tip and the surface is mediated by the attractive van der Waals forces (contact) that lead to an attraction of the tip toward the surface (B). Hence, the tip applies a constant and default force upon the surface that leads to sample indentation and cantilever deflection (C). Subsequently, the tip tries to retract and to break loose from the surface (D). Various adhesive forces between the sample and the AFM tip, however, hamper tip retraction. These adhesive forces can be taken directly from the force-distance curve (E). The tip withdraws and loses contact to the surface upon overcoming of the adhesive forces (F).” Figure obtained from Shahin and *co-workers* [28].

The result of a force measurement is a measure of the photodetector current,  $I_p$  and the height position of the piezo,  $Z_p$ . In order to generate a force-distance curve, the  $I_p$  and the  $Z_p$  need to be converted into force and distance respectively [29].

In order to obtain meaningful results from the force-distance analysis, the exact spring constant of the cantilevers used is required. Cantilevers purchased by

manufacturers are generally delivered together with a data sheet, which gives the cantilever specifications. Properties such as the spring constant have generally been calculated from the cantilever geometry, and have not been experimentally measured. There are two major methods to accurately determine the cantilever's accurate spring constant; the measurement of the spring constant using a reference cantilever and the measurement of the spring constant using the thermal noise. More details about these two methods, as well as other methods can be found in the review paper of Cappella et al. [34]. In the present study, the thermal noise method was used to determine the spring constant.

## **2.9 Limitations of AFM**

Although the AFM can be used to investigate the surface of a wide variety of materials (polymers, metals, glasses, semiconductors, cells, bacteria etc.), it suffers from limitations in achieving atomic resolution. The tip attached on the cantilever is not ideally sharp. As a result an AFM image does not reflect the actual sample topography, but the interaction between the tip and the surface of the studied material. Advanced sharper probes (typically made by a carbon nanotube) have been produced in order to overcome this limitation; however the cost of these probes does not allow their use in everyday AFM imaging.

Finally, it should be noted that the AFM used for imaging the samples of this thesis, was calibrated approximately twice per year in the  $x$ ,  $y$ ,  $z$ -directions using a calibration grid.

### ***2.10 Introduction to Transmission Electron Microscopy***

Transmission electron microscopy (TEM) operates on the same basic principles as the light microscopes, but it uses electrons instead of light. It is well known that what can we see with light microscopes is limited by the wavelength of light. TEM uses electrons as a “light source” and their much shorter wavelength (de Broglie wavelength) make it possible to get a resolution a thousand times better than with a light microscope. The instrument is able to study small details in the cell or different materials down to near atomic levels, which is tens of thousands times smaller than the smallest resolvable object in a light microscope. The capability for high magnifications has made the TEM a valuable tool in medical, biological, polymer and materials research.

In general, TEM is a technique in which a beam of electrons is transmitted through a specimen and interacts with the specimen as it passes through. An image is produced from the interactions of electrons transmitted through the specimen. As shown in Figure 2.4, a light source at the top of the microscope emits the electrons, which pass through a column of the machine under vacuum. Condensed electromagnetic lenses are used in order to focus the electrons in a very thin beam. Subsequently, the focused beam passes through the specimen. Depending on the density of the specimen some of the electrons of the beam are scattered and disappear. The electrons which have not been scattered reach a fluorescent screen at the bottom of the microscope, giving rise to a ‘shadow image’ of the specimen. The different parts of the specimen are displayed in varied darkness, according to their density. The image is generated and captured mainly through a CCD camera. There

are three important mechanisms which generate image contrast in the TEM: mass-thickness contrast, diffraction contrast-bright field and phase contrast [29-32]. In this thesis we used mass-thickness and bright-field mechanisms.

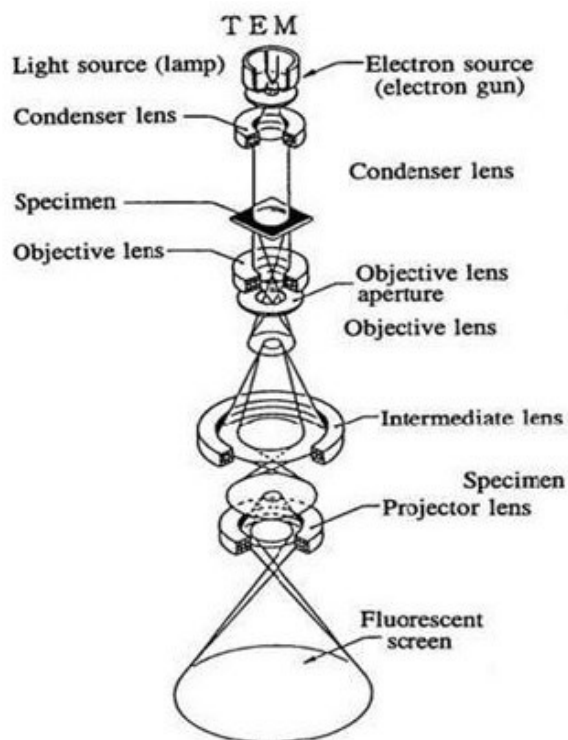


Figure 2.4 General outline of a TEM describing the route of electron beam in a TEM (Taken from JEOL 2000FX Handbook)

### 2.10.1 Mass-thickness contrast

Mass-thickness contrast is the basic imaging mechanism in biological and non-crystalline (e.g. glass) TEM applications [32]. It is well known that the interaction between heavy atoms and electrons is stronger than the interaction with light atoms. If the thickness of the films is relatively homogeneous, the areas in which the heavy atoms are concentrated appear with darker contrast than the contrast of the light atoms (mass contrast). In addition, when the focused beam reaches the sample more

electrons will be scattered from the thick areas than the thin. As a result thick areas appear dark (thickness contrast). However, it is likely that a thick area with light atoms may exhibit the same contrast as a thinner area with heavier atoms.

### **2.10.2 Bright Field Contrast**

Bright field (BF) or the reversible Dark Field (DF) is the most common contrast mechanism for crystalline materials. A small aperture (diameter  $\sim 5 - 70 \mu\text{m}$ ) is inserted in the objective lens to intercept the diffracted beam and only allow the transmitted beam to form an image. This process is known as BF or DF imaging.

### **2.10.3 Limitations of TEM**

Regardless of the great advantages and capabilities of the TEM, this technique exhibits several drawbacks. In TEM imaging the resolution is inversely proportional to the volume of the sample. The smaller the volume the higher the resolution, thus TEM is suitable only for low volume samples. In addition, TEM images are two-dimensional projections of three-dimensional structures. Furthermore, TEM uses a high energy beam, which may cause damage to the sample. Finally, the sample preparation process (thin specimens containing no volatile components) for TEM, increases the limitations of the system. All the limitations mentioned above may be overcome by using atomic force microscopy techniques as mentioned in the previous parts. On the other hand, AFM is a surface specific technique, giving few or no information about the composition inside the film. Combining both techniques a detailed analysis of the surface structural behaviour and compositions can be achieved.



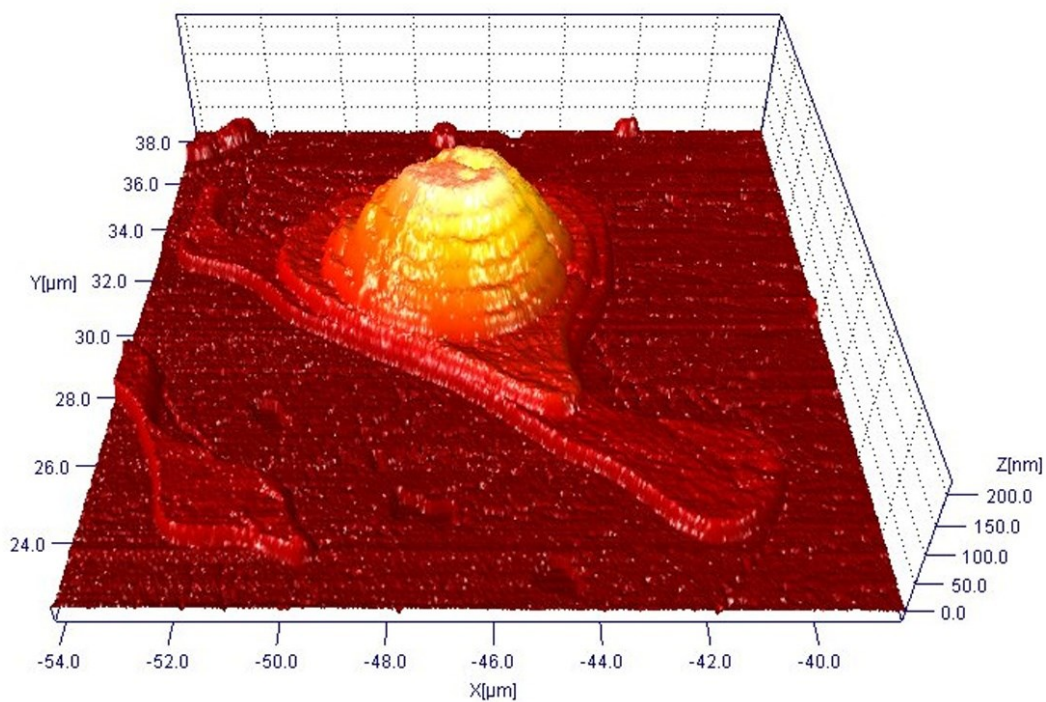
### **2.11 References**

1. Jones R and Richards R. *Polymers at Surfaces and Interfaces*. Cambridge: Cambridge University Press, 1999.
2. Gast AP and Leibler L. *Macromolecules* 1986;19(3):686-691.
3. Cox JK, Eisenberg\* A, and Lennox RB. *Current Opinion in Colloid & Interface Science* 1999;4(1):52-59.
4. Brown HR. *Science* 1994;263(5152):1411-1413.
5. Collins and Francis S. *Nature Genetics*.
6. Pludeman E and Collins N. *Adhesion Science and Technology*. New York: Plenum Press, 1975.
7. Chremos A, Glynos E, Koutsos V, and Camp PJ. *Soft Matter* 2009;5(3):637-645.
8. Hamley IW. *The Physics of Block Copolymers*. Oxford: Oxford University Press, 1998.
9. Viswanathan R, Tian J, and Marr DWM. *Langmuir* 1997;13(6):1840-1843.
10. Koutsos V, van der Vegte EW, Pelletier E, Stamouli A, and Hadziioannou G. *Macromolecules* 1997;30(16):4719-4726.
11. Koutsos V, van der Vegte EW, and Hadziioannou G. *Macromolecules* 1999;32(4):1233-1236.
12. Lohse DJ and Hadjichristidis N. *Current Opinion in Colloid & Interface Science* 1997;2(2):171-176.

13. Bar G, Thomann Y, and Whangbo MH. *Langmuir* 1998;14(5):1219-1226.
14. Sawyer LC and Grubb DT. *Polymer Microscopy*. New York: Chapman and Hall, 1987.
15. Magonov SN and Reneker DH. *Annual Review of Materials Science* 1997;27(1):175-222.
16. Utracki LA. *Thermodynamics of Polymer Blends*. Dordrecht: Kluwer Academic Publishers, 2002.
17. Flory PJ. *The Journal of Chemical Physics* 1941;9(8):660.
18. Huggins ML. *The Journal of Chemical Physics* 1941;9(5):440.
19. Merfeld GD and Paul DR. *Polymer-Polymer Interactions Based on Mean Field Approximations*. New York: Wiley-Interscience Publ., 2000.
20. Chen CJ. *Introduction to Scanning Tunneling Microscopy*. Princeton: Princeton Univ. Press, 1993.
21. Binnig G, Quate CF, and Gerber C. *Physical Review Letters* 1986;56(9):930-933.
22. Binnig G, Rohrer H, Gerber C, and Weibel E. *Physical Review Letters* 1983;50(2):120-123.
23. Press Release: The 1986 Nobel Prize in Physics. 1986.
24. Zhong Q, Inniss D, Kjoller K, and Elings VB. *Surface Science* 1993;290(1-2):L688-L692.

25. Magonov SN, Elings V, and Whangbo MH. *Surface Science* 1997;375(2-3):L385-L391.
26. Butt H-J, Cappella B, and Kappl M. *Surface Science Reports* 2005;59(1-6):1-152.
27. Janshoff A, Neitzert M, Oberdörfer Y, and Fuchs H. *Angewandte Chemie International Edition* 2000;39(18):3212-3237.
28. Shahin V, Ludwig Y, Schafer C, Nikova D, and Oberleithner H. *Journal of Cell Science* 2005;118(13):2881-2889.
29. Ortiz C and Hadziioannou G. *Macromolecules* 1999;32(3):780-787.
30. Williams DB and Barry Carter C. *Transmission electron microscopy : a textbook for materials science*. New York: Springer, 2009.
31. Reimer L and Kohl H. *Transmission electron microscopy: physics of image formation*. New York: Springer, 2008.
32. Bozzola J and Russell L. *Electron microscopy : principles and techniques for biologists*. Boston: Jones and Bartlett, 2006.
33. Baclayon M, Wuite GJL and Roos WH. *Soft Matter* 2010;6:5273-5285.
34. Cappella B, Dietler G. *Surface Science Reports* 1999;34:1-104.

**Chapter 3    Diblock  
Copolymer Nanostructures  
Self-Assembled on Mica**



**PI-*b*-PEO,  $f_{\text{PEO}} = 0.49$ , spin coated on mica at 4,000 rpm. The average polymer thickness is ~ 13 nm.**

### 3.1 Introduction

Amphiphilic semi-crystalline block copolymers composed of hydrophobic-hydrophilic blocks have attracted the attention of scientists in fields of nano-electronics and in bio-technology [1]. The great variety of self-assembled nanostructures exhibited by these polymers, either in bulk or dispersed in solvents, is the result of the interaction between the molecular structure and the interplay of the blocks. Both the stable phase separation of the blocks and the polymer's capacity to respond under selective physical or chemical conditions have been exploited in lithography and as sensors (surface responsive materials) [2].

Herein, the structural behaviour of three amphiphilic semi-crystalline poly(isoprene-*b*-ethylene oxide) block copolymers (PI-*b*-PEO) with different PEO volume fraction ( $f_{\text{PEO}} = 0.32, 0.49$  and  $0.66$ ), spin coated on mica surfaces in ambient conditions from aqueous solutions, was investigated by atomic force microscopy. We focus on the dependence of the resulting thin film nanostructures on the molecular characteristics ( $f_{\text{PEO}}$  and molecular weight) and the adsorbed amount – quantified by the average polymer thickness (APT). The nanostructures obtained immediately after spin coating were proven to be robust and remained unchanged after heating/annealing and/or ageing. The affinity of the PEO block for the highly hydrophilic substrate (freshly cleaved mica) and the tendency of the hydrophobic and low surface energy PI to dewet and be at the free interface, caused the soft PI-*b*-PEO micelles to collapse leading to the formation of two-dimensional, crystallised, dendritic networks over mica. We show that for all three polymers, the monolayer thickness can be predicted by a model consisting of a PEO crystallised layer (directly

on top of mica) of the same thickness in all cases and a PI brush layer on top. In thicker areas, polymer material self-assembled into cone-like multi-lamellar bilayers on top of the crystallised monolayer and oriented parallel to the substrate for both symmetric and asymmetric diblock copolymers with the lowest  $f_{\text{PEO}}$ . We also compare the lateral morphology of the films and discuss the thickness heterogeneity, which results from the complex coupling and competition of crystallisation kinetics, phase separation and wetting/dewetting phenomena highlighting the role of the two blocks to inhibit or enhance certain morphologies. We show that the deviation of the  $f_{\text{PEO}} = 0.32$  thin film from its bulk phase structure (cylinders in hexagonal lattice) continues for several lamella bilayers away from the substrate. For the asymmetric PI-PEO polymer with the higher PEO volume fraction ( $f_{\text{PEO}} = 0.66$ ) and higher APT, laterally extensive stacks of flat-on (2D) lamellae crystallites formed on the surface, demonstrating the crucial role of crystallisation of the PEO block in this case.

### **3.2 Background**

Diblock copolymers, macromolecules composed of two chemically distinct blocks that are covalently linked together, are one of the most well-known self-assembling systems [3]. They have received considerable attention as the building blocks for advanced nanotechnologies based on “bottom-up” fabrication methods [4]. Thin films of diblock copolymers have shown promise for use and applications in various technological sectors spanning from biotechnology [5] to nanoelectronics [6]. In contrast to the lithographic methods (“top-down” fabrication) the formation of nanopatterns driven by the self-assembly of diblock copolymers offers a combination of simple preparation, “low-cost” processing and efficient nanodevices [7].

Poly(isoprene-*b*-ethylene oxide) block copolymers (PI-*b*-PEO) in particular, have been used as structure-directing molecules for the fabrication of mesostructured inorganic materials which find applications in molecular engineering (catalysis, membranes and separation technology) [8]. The low glass transition temperature ( $T_g$ ) of both the PEO and the PI blocks ( $\sim -60$  °C), leads to high mobility at room temperatures resulting in *fast developing* of long-range nano-domains [8].

Thermodynamic incompatibility between the blocks could drive the diblock copolymer molecules to develop self-assembled periodic ordered nanostructures via microphase separation. The microphase separation of diblock copolymers is primarily determined by the overall degree of polymerization  $N$ , the temperature dependent [1] A-B segment–segment interaction (Flory-Huggins) parameter  $\chi$ , and the volume fraction of the A or B block,  $f_A$  or  $f_B$  [9]. The parameter  $\chi N$  determines the degree of segregation of the blocks. When  $\chi N < 10$ ; entropic terms between the blocks prevail resulting in a disordered phase. When  $\chi N > 10$ ; enthalpic terms dominate causing an order-to-disorder (ODT) transition where the unlike blocks segregate into a variety of ordered periodic microstructures [1]. Below the temperature where the order-disorder transition occurs ( $T_{ODT}$ ), the diblock copolymers undergo microphase separation between the unlike blocks which form into ordered structures [10]. For nearly symmetric compositions ( $f_A \approx f_B$ ), the blocks tend to phase separate into domains with alternate layers, known as lamellar phase. For asymmetric compositions, phases such as hexagonal and spherical could be obtained [1].

When the diblock copolymer is composed of a crystallisable block and an amorphous block; the complexity of the system increases significantly [11-14]. The microphase morphology in such systems depends on the melting temperature  $T_m$  of the crystallisable block, the glass transition temperature ( $T_g$ ) of the amorphous block ( $T_g < T_m < T_{ODT}$ ) [15], the copolymer composition and the phase separation strength ( $\chi N$ ) [1,11]. In particular, the phase behaviour of a series of PI-*b*-PEO has been studied by Floudas *et al.* [16,17], using small-angle *X*-ray scattering (SAXS). They have constructed a detailed phase diagram of the PI-*b*-PEO system based on block copolymers spanning the composition range  $0.05 < f_{PEO} < 0.8$ , where  $f_{PEO}$  is the PEO volume fraction. Typical areas of the phase diagram are: cylinders packed in a hexagonal lattice for  $f_{PEO} \approx 0.30$ ,  $\chi N > 45$  and  $f_{PEO} \approx 0.75$ ,  $45 < \chi N < 53$ ; for  $\chi N > 55$  and  $0.35 < f_{PEO} < 0.8$  the phase reverts to crystalline lamella ( $L_c$ ); while for  $f_{PEO} \approx 0.50$  and between  $40 < \chi N < 55$  the phase is (amorphous) lamellae (Lam).

When diblock copolymers are confined into supported thin films, the nature and strength of the interfacial interactions in the asymmetric interfaces (polymer/solid and polymer/air interface) influence the thin film morphology, phase separation and orientation of the blocks [1]. For symmetric diblock copolymers ( $f \approx 0.5$ ) the lamellar structure remains the typical thin-film morphology. If there is preference of one of the blocks for any of the interfaces involved (substrate or free interface), parallel to the substrate orientations of the lamella are observed [1]. If the same block has a higher affinity for both the free surface and substrate, then this block will wet both interfaces (symmetric wetting) and the film thickness is given by  $nL_0$ , where  $n$  is an integer corresponding to the number of the period, and  $L_0$  is the



length of the period of the microdomain morphology. On the other hand, if different types of blocks segregate to the interfaces (asymmetric wetting) the film thickness is given by  $(n + 1/2)L_0$  [18]. However, if the thickness of the thin film is not commensurate with these quantized thicknesses, for overall thickness below  $\sim L_0$  the substrate is only partly covered while for a higher thickness, holes and islands are formed [19].

For asymmetric diblock copolymer thin films ( $f \neq 0.5$ ) the affinity of one block to the substrate can alter the bulk morphology (cubic, hexagonal) to lamella [20], which is also theoretically shown by Turner *et al.* [21] for asymmetric hexagonal phase diblocks. Recently, Papadakis *et al.* [22] have studied the morphology of spin-cast thin films of low-molar-mass cylinder-forming PI-PEO diblock with  $f_{\text{PEO}} \approx 0.28$ , from toluene solutions onto silicon wafers. Upon spin-coating, their films were annealed above the  $T_m$  of the PEO block (32 °C) for several minutes. AFM images revealed the formation of hexagonally packed, amorphous PEO cylinders lying parallel to the substrate and surrounded by a PI matrix. However, several months later, they have observed that the surface morphology had dramatically changed. Terraced finger-like bilayer lamella patterns with the PI on top were formed over a monolayer located directly on the silicon wafer. They argued that this structural transition, from hexagonal to lamellar is due to a significant but slow mass transport (in a period of about 5 months), which ultimately leads to terracing. The annealing was not capable of bringing the system into lamella formation which is attained only after significant aging. In an earlier study on PI-PEO diblocks performed by Glynos and *co-workers* [23], it was shown that the “gentle” deposition of PI-*b*-PEO ( $f_{\text{PEO}} \approx$

0.66) micelles from aqueous solutions on freshly cleaved mica substrates resulted in the collapse of the micelles producing flat polymer nanoislands of well-defined thickness. The favourable interaction between the ultrathin water layer of mica and the hydrophilic PEO block [23], as well as the flexibility of the PI block played a crucial role for the dissociation of the micelles resulted in close-to equilibrium structures in cast films.

PEO-based thin films have important biomedical applications as PEO is biocompatible and exhibits protein resistance [24,25]. Although one of the unique attractions of PEO is its water solubility [26,27] (which is related to its biomedical properties), studies of the fundamentals of PEO-based thin films have mainly used organic solvents combined with heat treatment for the formation of micro/nanopatterns on surfaces. In this study, we focus on the formation of thin films of PEO-based diblock copolymers from water solutions and we show that the use of water solutions and the hydrophilic freshly-cleaved mica gave the mobility needed for the PEO-based copolymers to form rapidly robust multi-layered structures without requiring any prior annealing or ageing. We used three different poly(isoprene-*b*-ethylene oxide), PI-*b*-PEO, block copolymers with  $f_{\text{PEO}} = 0.32, 0.49,$  and  $0.66$  (and the corresponding homopolymers for comparison) so that we study the effect of the volume fraction of the hydrophilic and crystallisable block in the thin film morphology. We considered the effect of the polymer film thickness to establish the differences between ultrathin and thicker films; i.e. approaching-bulk behaviour. We present and discuss the dependence of the nanostructures on the surface coverage, the molecular weight, and the composition ( $f_{\text{PEO}}$ ) of the polymers. We

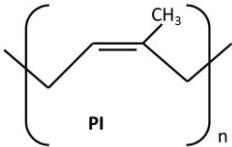
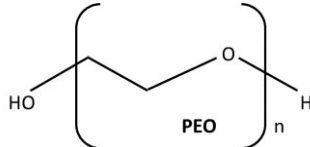
found that immediately after spin coating both the symmetric and asymmetric polymers formed a stable dendritic monolayer on top of mica, nucleated at the thicker areas of the film. We show that a model consisting of a PEO crystallised layer (directly on top of mica) with a set thickness (as measured for two PEO homopolymers) and a PI brush above compares very well with the experimental results. Above the monolayer the symmetric,  $f_{\text{PEO}} = 0.49$ , and the asymmetric polymer with lower percentage of PEO,  $f_{\text{PEO}} = 0.32$ , formed multi-lamellae bilayer terraces. However, when the fraction of the PEO block took a value of 0.66, we observed the formation of 2D layered spherulitic-like areas. We discuss the complex interplay of wetting/dewetting, phase separation and crystallisation kinetics which affects the lateral morphology of the films.

### **3.3 Experimental**

#### **3.3.1 Materials and Characterization**

A series of poly(isoprene-*b*-ethylene oxide), PI-*b*-PEO, block copolymers were synthesised using anionic polymerization high vacuum techniques by Pispas and *co*-workers [23] and their molecular characteristics along with their molecular structures are shown in Table 3.1.

**Table 3.1 Chemical and Physical Properties of the three PI-*b*-PEO copolymers.**

Code	$M_w^a$ (kg/mol)	$M_w/M_n$	% wt PI <sup>b</sup>	$f_{PEO}^c$	$M_{w, PEO}$ (kg/mol)	$M_{w, PI}$ (kg/mol)	$T_m^d$ (°C)	$T_c^d$ (°C)	$\chi N^e$
IEO1	22.8	1.05	63	0.32	8.4	14.4	52	26	131
IEO2	16.4	1.08	46	0.49	8.9	7.6	55	29	99
IEO3	20.7	1.03	29	0.66	14.7	6.0	60	39	140
									

<sup>a</sup> From size exclusion chromatography (SEC) <sup>b</sup> From <sup>1</sup>H NMR. <sup>c</sup> Block copolymer composition, calculated from  $N_n^* = N_{n,PI}^* + N_{n,PEO}^* = N_{n,PI} (\rho_{EO}^*/\rho_{PI}^*)^{1/2} + N_{n,PEO} (\rho_{PI}^*/\rho_{EO}^*)^{1/2}$  and  $f = N_{n,PEO}^*/(N_{n,PI}^* + N_{n,PEO}^*)$ , where  $N_{n,i}$  are the degrees of polymerisation of each block  $k$  and  $\rho_i^*$  are the molecular densities. For the densities we have used the values 0.895 and 1.120 g/cm<sup>3</sup> for PI and PEO, respectively [17]. <sup>d</sup> From DSC measurements (temperature ramp 10° C/min, values from second cycle). <sup>e</sup>  $\chi = 65/T + 0.125$  [16],  $T \approx 300$  K.  $N$  is the degree of polymerization. We note that the order-disorder transition temperature is  $T_{ODT} \approx 473$  K [17].

Although the polymers are of similar total molecular weight we note the following: for the first two polymers, the PEO molecular weight is essentially the same (8.4 kg/mol for  $f_{PEO} = 0.32$  and 8.9 kg/mol for  $f_{PEO} = 0.49$ ), but the  $f_{PEO}$  is different because the molecular weight of PI is different (14.4 kg/mol for  $f_{PEO} = 0.32$

and 7.6 kg/mol for  $f_{\text{PEO}} = 0.49$ ). Only in the case of  $f_{\text{PEO}} = 0.66$ , we increased substantially the PEO molecular weight (14.7 kg/mol) while the PI block has a smaller molecular weight of 6.0 kg/mol. The asymmetric polymer with  $f_{\text{PEO}} = 0.66$  (IEO3) in aqueous solutions forms spherical micelles, while the other two polymers with less volume fraction of PEO form cylindrical and spherical micelles [23, 28].

### 3.3.2 Sample Preparation and AFM measurements

Water solutions (deionised water, DI, with resistivity of 18.2 M $\Omega$ ·cm) of the different PI-PEO block copolymers were prepared in three different concentrations ( $\sim 10^{-3}$  g/g,  $\sim 2 \times 10^{-3}$  g/g,  $\sim 10^{-2}$  g/g). The solutions were heated at 60 °C overnight before use to ensure the complete dilution of the sample [28,29]. Films were prepared by spin-coating filtered droplets of the solutions onto freshly cleaved mica substrates. The spin coating speed and time remained constant in all cases. The samples were then gently dried under a stream of nitrogen. Subsequently, they were imaged in ambient conditions at relative humidity of 30 – 38 %, in tapping mode. We used two AFM instruments: a Bruker AFM Multimode/Nanoscope IIIa (Bruker, Santa Barbara, CA, USA), equipped with a *J*-scanner ( $x$ - $y$  range  $\approx 140$   $\mu\text{m}$ ) and the NanoWizard II JPK AFM (JPK Instruments AG, Berlin, Germany). RTESP and/or RTESPA Bruker cantilevers with a nominal spring constant and resonance frequency of 40 N/m and 300 kHz, were used to image the samples. In order to minimize the interaction force between the tip and the substrate (but without losing contact) “light tapping” was used by keeping the set-point amplitude ratio  $r_{\text{sp}} = A_{\text{sp}}/A_0$  close to 1 (where  $A_0$  and  $A_{\text{sp}}$  are the free oscillation amplitude and the reduced scanning set-point amplitude of the cantilever, respectively) [30-32]. Images were processed and

the layer heights were measured using the software Scanning Probe Image Processor (SPIP, Image Metrology, Hørsholm, Denmark).

Generally, thin films of semi-crystalline diblock copolymers prepared by spin-coating in ambient conditions, result in the crystallisation of the film leading to the some thickness heterogeneity [33]. For this reason, the average thickness of each polymer film was determined by calculating the total volume per unit area of the observed structures (eq. 3.1); we refer to this thickness as the average polymer thickness (APT). For polymer concentrations  $\sim 1 \times 10^{-3}$  g/g the APT was found to be  $\approx 7 \text{ nm} \pm 1 \text{ nm}$ , for concentrations  $\sim 2 \times 10^{-3}$  g/g the APT was  $\approx 13 \text{ nm} \pm 2 \text{ nm}$  and for concentrations  $\sim 1 \times 10^{-2}$  g/g the APT was  $\approx 41 \text{ nm} \pm 5 \text{ nm}$ . It is worthwhile noting that we have imaged several sample surfaces after about 7 months or more (stored in controlled humidity/temperature environment) and the images showed the same morphology signifying that our preparation protocol produced stable structures as far as ageing is concerned. In addition no changes were observed when the different PI-PEO thin film samples were annealed at  $65 \text{ }^\circ\text{C}$  (i.e. above melting temperature) for several minutes and cooled at room temperature.

$$\text{APT} = \frac{\text{pixel volume} \times \text{number of pixels}}{\text{area of scan}} \quad (3.1)$$

Furthermore, we used two molecular weights of PEO:  $M_w = 8 \text{ kg/mol}$  ( $M_w/M_n = 1.04$ , Polymer Source Inc. Quebec, Canada) and  $M_w = 14 \text{ kg/mol}$  ( $M_w/M_n = 1.08$ ) synthesized by Pispas and *co-workers* and one molecular weight of PI:  $M_w = 10 \text{ kg/mol}$  ( $M_w/M_n = 1.05$ ) synthesized by Pispas and *co-workers* by anionic polymerization [34,35] to investigate the behaviour of the corresponding

homopolymers at the same conditions as the diblocks. Separate DI water solutions of PEO and toluene solutions of PI were prepared (same concentrations as with diblocks) and spin cast thin films on mica (using the same protocol) were prepared and imaged with AFM (Figure 3.1). PEO forms flat dendrite-like patterns, which become *denser* as the solution concentration increases (Figures 3.1a, b and c). In contrast, PI forms spherical caps on mica which become *less frequent but larger* with concentration were (Figures 3.1d, e, f). These results confirmed the tendency of the hydrophobic PI to *dewet* on mica, unlike the hydrophilic PEO which prefers to spread on mica.

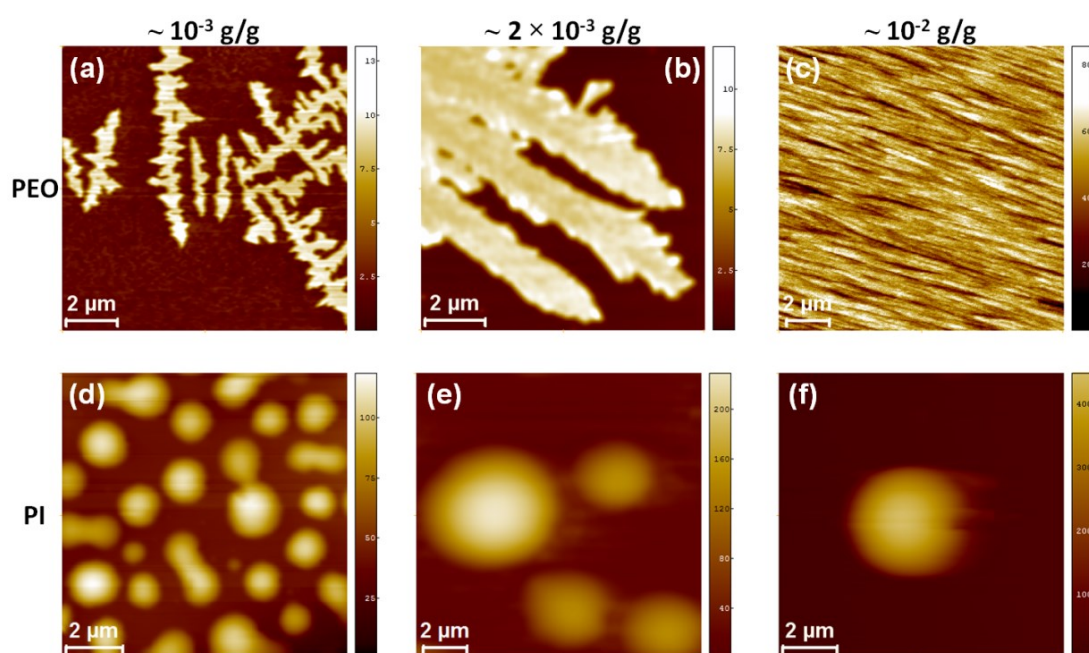


Figure 3.1 Typical AFM height images (maximum values in the colour scales are: 15, 14, 85, 125, 215, 410 nm for a, b, c, d, e, f, accordingly) of (a), (b), (c) PEO and (d), (e), (f) PI thin films from three different solution concentrations ( $10^{-3}$  g/g,  $2 \times 10^{-3}$  g/g and  $10^{-2}$  g/g).

### 3.4 Results and Discussion

Figure 3.2 shows typical AFM images from the polymer films measured in this study. It is clear that the observed structures formed on mica depend on the PI-*b*-PEO polymer characteristics and the average polymer thickness, APT. In all cases a thin first layer which has a 2D dendrite morphology was formed directly on the mica surface. On top of the first layer, and depending on the APT and the  $f_{\text{PEO}}$ , we observed thicker flat layers the thicknesses of which are approximately double of the thickness of the first layer as shown in Figure 3.3, which summarizes measurements based on cross-sections of many AFM images (some examples are given in the Appendix A). In what follows, we discuss in detail the formation and structure of the first layer and then we proceed to morphology of the thicker layers as the average polymer thickness increases from  $\text{APT} \approx 7$  to 13 and 41 nm.



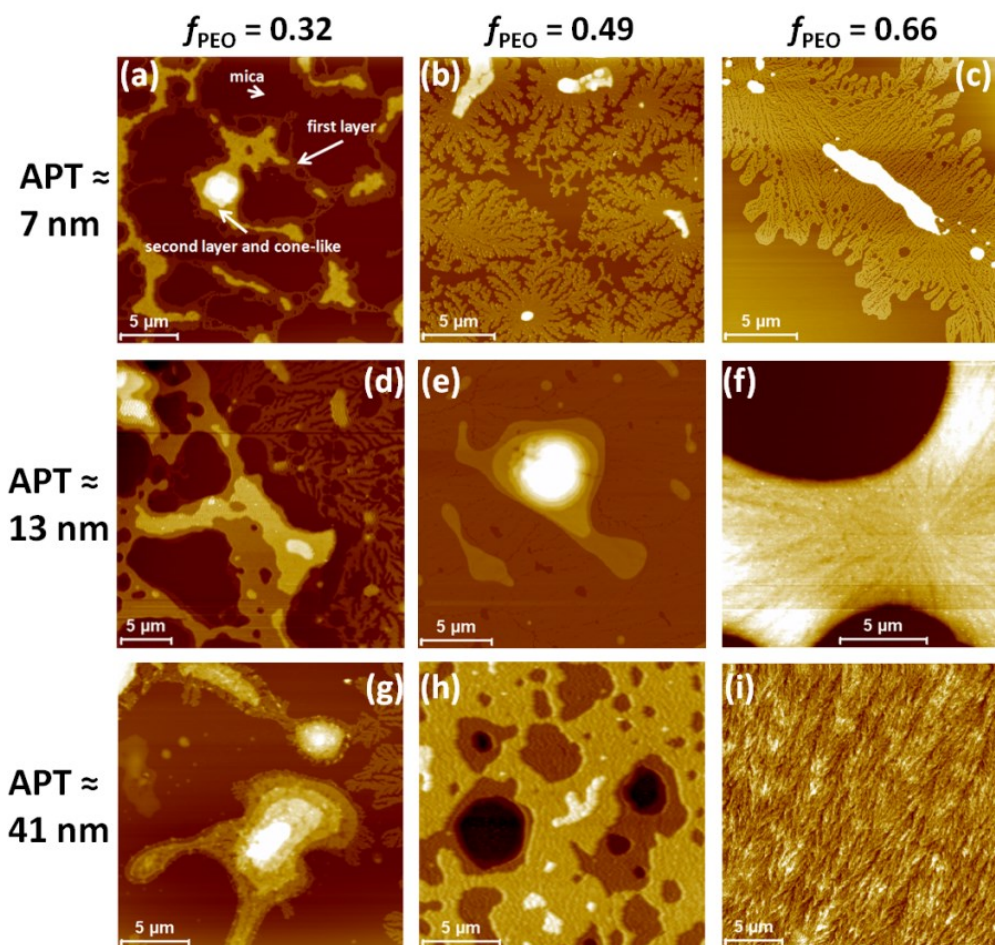


Figure 3.2 AFM height images demonstrating the typical thin film morphologies for  $f_{\text{PEO}} = 0.32$ , 0.49 and 0.66 PI-*b*-PEO block copolymers in relation to their average polymer thickness (resulting from different concentrations used during spin coating). The height scale for the images from a - i is: 157 nm, 73 nm, 49 nm, 233 nm, 242 nm, 190 nm, 160 nm, 113 nm, 43 nm, respectively.

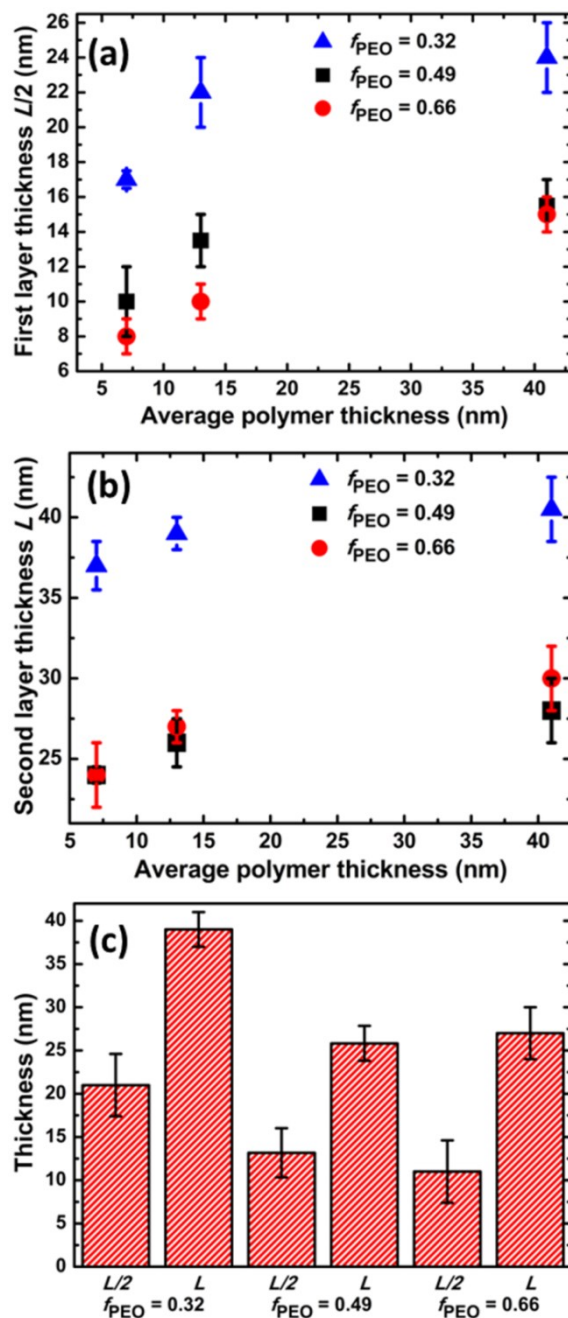


Figure 3.3 (a) First thin layer thickness against the average polymer film thickness for each of the three PI-*b*-PEO diblock copolymers (blue triangle bullets:  $f_{\text{PEO}} = 0.32$ ,  $M_w = 22.8$  kg/mol, black square bullets:  $f_{\text{PEO}} = 0.49$ ,  $M_w = 16.4$  kg/mol and red circle bullets:  $f_{\text{PEO}} = 0.66$ ,  $M_w = 20.7$  kg/mol); (b) thickness of the second layer (on top of the first thin layer) plotted against the average polymer thickness of the PI-*b*-PEO; (c) thickness of the first and second layer for the three PI-*b*-PEO diblock copolymers. We note that thickness values resulted from several height profiles taken across the observed structures. Some additional typical ones are presented in detail in the Appendix A (Figures A1 – A3).

### 3.4.1 Monolayer Formation on Mica

It is important to point that all the polymer concentration solutions used in our study were above the critical micelle concentration (cmc) of the corresponding PI-PEO polymers. Hence, when in solution, the PI-PEO had micellar structures. Nevertheless, upon spin coating the micelles were deformed and eventually disassociated. The combination of the soft/flexible PI core and the strong affinity of the PEO corona with the water layer of mica is the cause of the break-up of the micelles. This argument is also supported by a previous study, where they found that PI-*b*-PEO micelles, which were gently deposited on mica from water solutions, dissociated forming thin polymer monolayer islands with the PEO block wetting the substrate while the PI block dewetted mica [23]. The disassociation of the micelles upon deposition on surfaces has also been seen in other systems [36,37]. Mica in ambient conditions is hydrophilic owing to its polar character [38-41] and wetted with an ultrathin water layer [42]. The hydrophilic/water soluble PEO block aided by the presence of water, has the tendency to wet the substrate (Figure 3.1). The PI block prefers to wet the free interface (film/air) due to its lower surface tension compared to PEO ( $\gamma_{PI} \approx 33$  mN/m,  $\gamma_{PEO} \approx 45$  mN/m) [43,44].

Figure 3.3a indicates that the thickness of the first layer (monolayer) formed at mica substrate is strongly related to the APT on each film. The higher the APT, the greater the thickness of the monolayer is; nevertheless, there seems to be an asymptotic behaviour to a maximum value as the surface coverage increases. Increasing the APT causes a higher surface coverage of the PI-PEO molecules on the substrate. At high surface coverage, the PI-PEO molecules attached by the PEO

block to the mica, *stretch away* from the substrate to avoid overlapping resulting in a thicker layer; this is similar behaviour to a dense polymer ‘brush’ [45]. We also observe that the  $f_{\text{PEO}} = 0.66$  polymer forms thinner monolayers (see also Figures and height profiles in the Appendix A) compared to the other two polymers; as the fraction of the PEO decreases (the fraction of the PI block increases) the thickness of the monolayer increases accordingly. This could be attributed to a thinner brush formed due to the short length of the PI molecules resulting in thinner monolayers. To confirm this point we have calculated the thickness of the monolayer. AFM studies on PEO (8 kg/mol and 14 kg/mol) thin films on mica revealed that the average thickness ( $D_{\text{PEO}}$ ) of a dendrite structure formed on mica is  $\sim 6.5 \text{ nm} \pm 1 \text{ nm}$  (Appendix A, Figures A4 and A5). The thickness value remained *unaffected* by any change of the solution concentrations and by the change of the PEO molecular weight. The chain lengths of the fully extended PEO of  $M_{\text{W}} 8 \text{ kg/mol}$  and  $14 \text{ kg/mol}$  are  $L_{\text{PEO}} = l_{\text{u}}N_{\text{PEO}} = 51 \text{ nm}$  and  $89 \text{ nm}$  respectively (the PEO monomer length is  $l_{\text{u}} = 0.2783 \text{ nm}$ ) [46]. In order to match the fully extended values of the PEO chains with the average thickness of the PEO on mica, the PEO chain must be folded approximately 8 times for the PEO 8 kg/mol and 13 times for the PEO 14 kg/mol [16]. Thus, we expect that the PEO block chains in the PI-*b*-PEO systems would be approximately 8 times folded for  $f_{\text{PEO}} = 0.32$  ( $M_{\text{w,PEO}} = 8.4 \text{ kg/mol}$ ) and  $f_{\text{PEO}} = 0.49$  ( $M_{\text{w,PEO}} = 8.9 \text{ kg/mol}$ ) and 13 times folded for  $f_{\text{PEO}} = 0.66$  ( $M_{\text{w,PEO}} = 14.4 \text{ kg/mol}$ ) on mica, respectively [16]. In PI-*b*-PEO thin films, a unit cell of PEO has an area  $A = ab\sin(\beta)$ , where  $a = 0.805 \text{ nm}$ ,  $b = 1.304 \text{ nm}$  and  $\beta = 125.4^\circ$  and contains 4 fully stretched chains/parts of chains [22,46]. In our case, for  $f_{\text{PEO}} = 0.32, 0.49$  the PEO

block is folded in a way to correspond to  $\sim 9$  fully stretched parts of chain, and thus each PI block is confined to an area of  $\sim 2.3A$ . For  $f_{\text{PEO}} = 0.66$ , the PEO is folded so that it contains  $\sim 14$  stretched parts and thus each PI block is confined to an area of  $\sim 3.5A$ . The volume of the PI block for each PI-PEO system (Table 3.2) is calculated based on its density ( $0.895 \text{ g/cm}^3$ ) [17] and molecular weight ( $M_{w,\text{PI}}$ , see Table 3.1). This volume is divided by the corresponding area and provides the thickness of the PI brush layer presented in Table 3.2. Finally, the sum of the average PEO thickness on mica ( $D_{\text{PEO}} \sim 6.5 \text{ nm}$ ) and the thickness of the PI brush ( $D_{\text{PI}}$ ), gives the thickness of the PI-PEO monolayer on mica shown in Table 3.2. These values compare very well and are within the thickness range of the measured by AFM average PI-PEO monolayer thickness presented in Table 3.2 and also in Figure 3.3a.

**Table 3.2 Calculation details for the PI brush**

Polymer, $f_{\text{PEO}}$	Average thickness of PEO monolayer, $D_{\text{PEO}}$ (nm)	Number of stretched parts of chain	Interfacial area for each PI block ( $\times A$ )	PI block volume ( $\text{nm}^3$ )	Thickness of PI brush, $D_{\text{PI}}$ (nm)	$D_{\text{PEO}} + D_{\text{PI}}$ (nm)	Average first layer thickness (nm)
0.32	6.5	9	2.3	26.7	13.6	20.1	$21.0 \pm 3.6$
0.49	6.5	9	2.3	14.0	7.1	13.6	$13.0 \pm 2.8$
0.66	6.5	14	3.5	11.1	3.7	10.2	$11.0 \pm 3.6$

The monolayer has a two-dimensional dendrite morphology. The dendrites started growing from the thicker areas of the film (nucleation points) and are typical for the crystallisation of PEO homopolymers and copolymers containing PEO-blocks in ultrathin film geometries [1,13,33,47-50]. We note that at room temperature our system is below  $T_m \approx 55$  °C. The thicker areas act as a ‘reservoir’ feeding the dendrite formation as water evaporates in similar fashion to other studies, where the feeding proceeds during cooling from molten state [47]. Their expansion- growth across the substrate is associated with a diffusion-limited crystallisation mechanism [51,52]. Although most of the studies based on PEO homopolymer and copolymers require annealing above the melting point of the PEO block in order to form the dendritic monolayer, in all our thin films on mica dendrite formation was formed without any prior heat treatment. Moreover, we annealed several thin films above the corresponding  $T_m$  (see Table 3.1) and we observed no changes to the dendrite structures on mica; the structures were unaffected. To investigate further this behaviour, we spin coated PI-PEO thin films on (lightly cleaned by 50/50 isopropanol/methanol mixture) silicon (with a native silicon oxide surface) substrates. Typical AFM images of PI-PEO ( $f_{\text{PEO}} = 0.49$ , APT = 13 nm) thin films on mica and on silicon substrates are presented in Figures 3.4a and b respectively. Over mica we observed the formation of the dendritic structures, while over the silicon substrate (which was lightly cleaned by 50/50 isopropanol/methanol mixture) a more flat and featureless monolayer was formed. The results showed no evidence of dendrite patterns, which agrees with other studies of amphiphilic diblock copolymer films prepared from selective solvent solutions on less-hydrophilic substrates [41].

Hence our data highlight the importance of the highly hydrophilic mica surface (when freshly cleaved) and its hydrated ultrathin surface layer on the formation of the observed structures; the presence of water is enhanced as we use aqueous solutions. These conditions provide the necessary mobility required for the quasi-2D diffusion limited crystallisation [49].

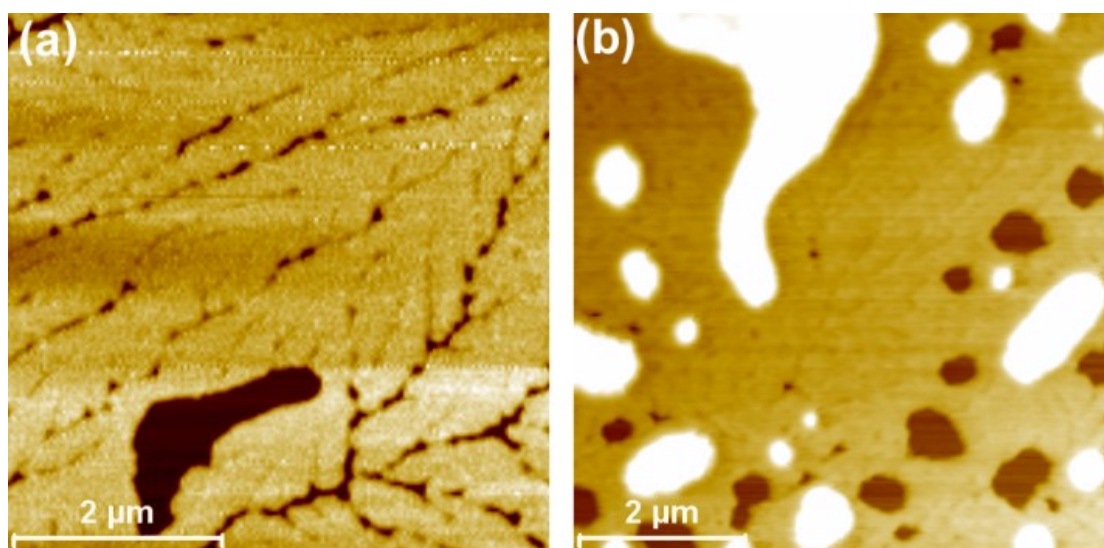


**Figure 3.4 (a) AFM topography image of the 13 nm film (PI-b-PEO block copolymer with  $f_{\text{PEO}} = 0.49$ ) (b) AFM topography image of the same film on Si wafer. The focus is on the morphology of the first layer (monolayer).**

When the average thickness of the polymer material on the substrate is less than the thickness of the half lamellar period in the bulk (for asymmetric wetting as in our case), the amount of polymer is not enough to form a full monolayer [33,39,53]. The half lamellar bulk values for our polymers can be approximated by the half of the asymptotic bilayer thickness values (Figure 3.3) and are roughly 20.5, 14 and 15 nm for  $f_{\text{PEO}} = 0.32$ , 0.49 and 0.66, respectively; these values are in agreement with measurements of the bulk lamella thickness of similar molecular weights of the same polymer [16]. Thus, for an average film thickness (APT) of 7 nm

we expect only partial coverage in all cases as actually seen in the corresponding images (Figures 3.2a-c). At  $APT = 13$  nm, we are still away from the half lamella thickness for  $f_{PEO} = 0.32$  and to some extent for 0.66, but for  $f_{PEO} = 0.49$  we are close to half lamella and full coverage (Figure 3.2e).

For  $f_{PEO} = 0.66$  in particular at higher concentrations, we have observed that there is a tendency for the monolayer to be covered by the excess material which could be due to PEO crystallisation which proceeds faster when away from the substrate [33]. This faster crystallisation during the rapid spin-coating process could deplete material and prevent full coverage. At even higher concentrations ( $APT = 41$  nm) the substrate is fully covered as expected (Figure 3.2i) and also for the polymer with  $f_{PEO} = 0.49$  (the occasional holes in Figure 3.2h are due to the dewetting on top of the monolayer to be discussed later) but surprisingly for  $f_{PEO} = 0.32$  the monolayer is far from being completely formed (Figure 3.2g). We note that there is a complex coupling and competition between wetting and phase separation into lamella layers at high segregation strengths ( $\chi N = 131$  at  $T \approx 300$  K [17] according to the mean field theory [9], for  $f_{PEO} = 0.32$ ) [54]. Furthermore, this last outcome could be the result of the rapid formation of the thin film due to spin-coating and (i.e. the kinetics of the process). It seems that the polymers which contain higher volume fractions of PEO are capable of more rapid evolution. Reiter and *co-workers* [33], who have extensively studied the kinetics of the crystalline dendrite patterns on the substrate from annealed semi-crystalline diblock systems, found that this is a relatively slow process compared to the formation of lamellar or crystalline lamellar structures away from the substrate. The dendrite patterns started growing from the thicker areas



towards the substrate and that the maximum length of dendrite patterns significantly varied. In our case, for  $f_{\text{PEO}} = 0.32$  the influence of the large hydrophobic PI block could perturb the diffusion/crystallisation of the diblock on the substrate and slow things even more, resulting in partial coverage.

### 3.4.2 Thicker Areas: Cone-Like Lamellae and Crystalline Lamellae

The symmetric polymer thin film behaviour ( $f_{\text{PEO}} = 0.49$ ) is characterised by the formation of thick multilayer cone-like structures on top of the dense dendrite layer (Figure 3.2e and Figure 3.5). The excess material dewetted autophobically on the chemically identical monolayer [55]. More precisely, the different chain conformation between the molecules attached on mica and molecules which are free in the overlying layers introduces entropic effects which inhibit the polymer to spread on a surface of the same material [56,57]. Autophobic phenomena driven by entropy differences have been reported in other polymer brush as well as in cross-linked systems [57-61]. The reason for cone-like terraced lamellar structures stems from the competition between the edge tension, which drives polymer from the higher smaller layers to lower larger ones, and the edge repulsion which inhibits two neighbouring edges approaching each other [62,63]. Each step corresponds to a lamella bilayer, arranged as PI-PEO/PEO-PI (as shown in the schematics of Figure 3.5f). The terraced structures observed consisted from 4 up to 8 lamella layers, with lamellar height  $L \approx 26$  nm which is approximately double the thickness of the corresponding first monolayer ( $L/2$ ) as shown in the graph of Figure 3.3c as well as in the height profile of Figure 3.5d and in the Appendix (Figure A2). This is the typical asymmetric wetting structures for symmetric block copolymer thin films

[1,19,62,64,65]. The thickness  $L$  of the second layer (Figure 3.3b) depends on the total molecular weight of the polymers and this compares well with other study, where an increase in the lamella thicknesses with increasing the  $M_w$  of the diblock copolymer chain has been reported [66].

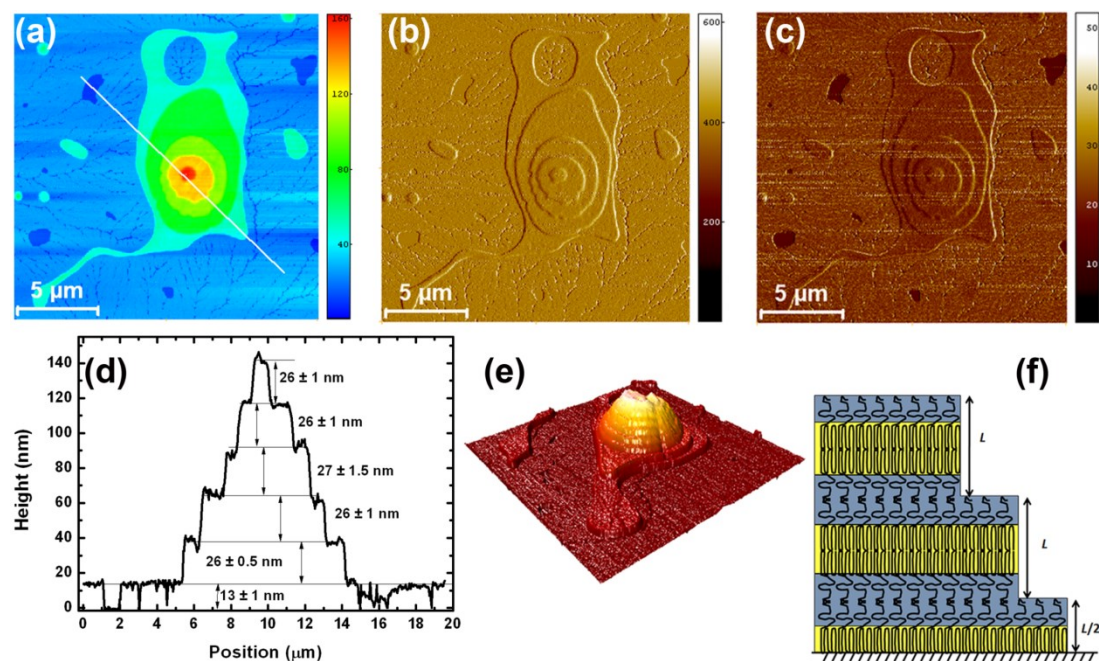


**Figure 3.5** (a) High contrast AFM topography image highlighting the cone-like terraced structure in the PI-PEO with  $f_{\text{PEO}} = 0.49$ , APT  $\approx 13$  nm; (b) AFM amplitude image (amplitude scale: 616 mV) of (a); (c) AFM phase image (angle units: degrees) of the area presented in (a); (d) Height profile of the corresponding image, the cone-like structures consist of 5 layers; (e) AFM 3D image of a different cone-like terraced area of the 13 nm film (PI-*b*-PEO block copolymer with  $f_{\text{PEO}} = 0.49$ ) containing 8 layers, the size of the image is  $20 \times 20 \mu\text{m}^2$  and the  $z$ -scale is 242 nm; (f) Schematic representation of the first thin monolayer directly over the mica substrate and the lamella orientation on top of the monolayer.

The asymmetric wetting behaviour (affinity of PEO block with the mica substrate and segregation of PI at the free interface, due to its lower surface tension compared to the PEO counterpart) is also confirmed by the phase imaging of Figure 3.5c. It is clear that the areas occupied from the polymeric structures appear with the same colour (orange); indicating the material is the same, i.e. the PI block is on top in all cases. We note that the main contrast difference in the phase [30,67,68] arises in

the areas where the hole reaches the mica substrate (dark brown colour) and stems from the differences in the mechanical/adhesive properties between the viscoelastic PI areas and stiff mica: similar behaviour (low surface energy block in the free interface) was found in the studies of the PB-PEO systems [69] and the PS-PEO systems [33,70].

In the case of the  $f_{\text{PEO}} = 0.32$ , cone-like structures and terraces (Figure 3.6 and Figures 3.2a, d, g) are present but not as well formed. The amplitude signal images reveal more clearly the fine details of the topography (compare Figures 3.5b and 3.6c). The steps/edges are much sharper for the symmetric polymer (see also Figures 3.5 and 3.6b). It is important to point out that in the asymmetric case of the PI-PEO with  $f_{\text{PEO}} = 0.32$  the bulk structure is a hexagonal phase as reported by Floudas and *co-workers* [17]. The lamella structure in the thin film geometry occurs due to the strong affinity of the PEO block with mica; i.e. interfacial interactions induce lamellar ordering. Li *et al.* studied an asymmetric polyethylene-*b*-poly(styrene-*r*-ethylene-*r*-butene) (short crystalline – long amorphous blocks as in our case for  $f_{\text{PEO}} = 0.32$ ) on silicon wafer substrates (annealed for several hours at 77 °C) and they observed that the lamella structure was retained for only one bilayer [20]. In our case the presence of water and the strongly hydrophilic mica when freshly cleaved, drive the formation of the lamellar structures without any heat treatment, i.e. as-cast films. Furthermore, in our case, we show that the lamella continues to several layers albeit with decreasing order. The thickness of the lamellar spacing, or else the thickness of the layers, decreased significantly only after the third terrace as shown in Figure 3.7. The lamella morphology becomes unfavourable for this asymmetric polymer as we

move away from the substrate and the system will eventually obtain its bulk structure.

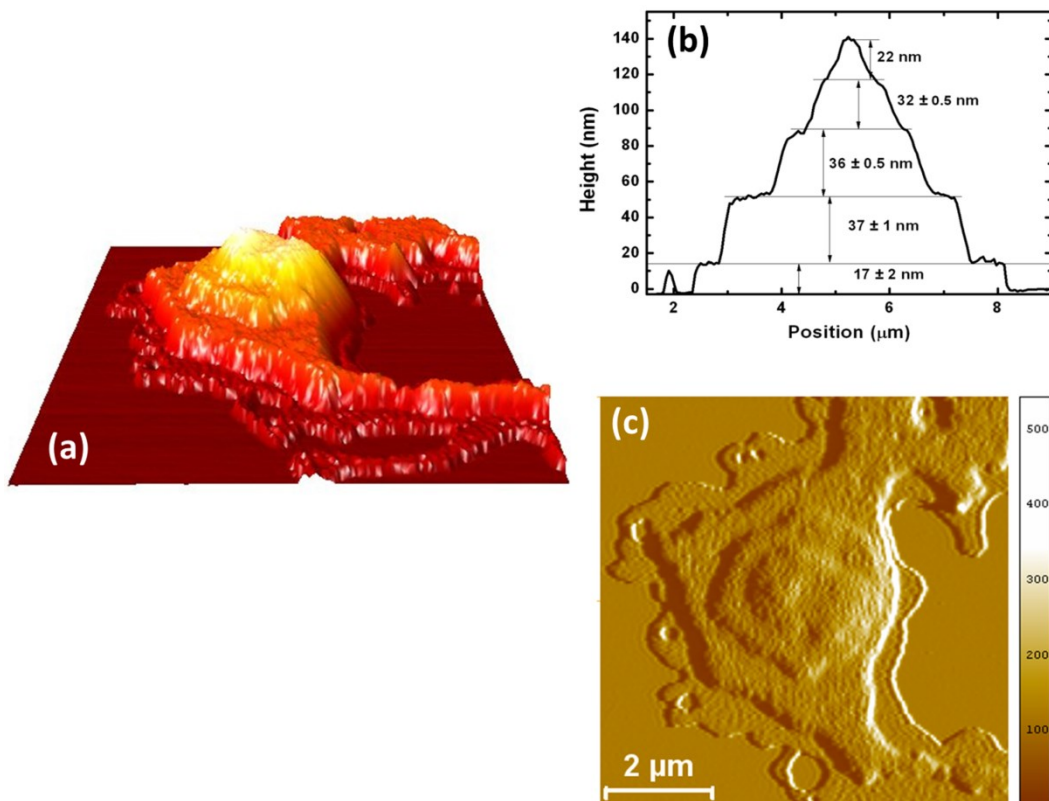
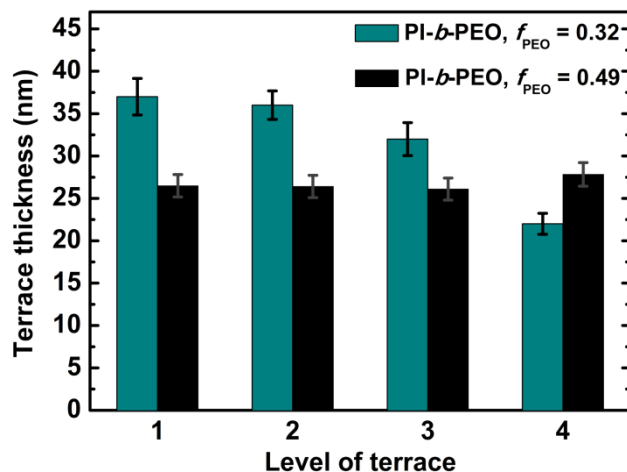


Figure 3.6 (a) AFM 3D topography image highlighting the cone-like terraced structure in the PI-PEO with  $f_{\text{PEO}} = 0.32$ ,  $\text{APT} \approx 7$  nm; the size of the image is  $9 \times 9 \mu\text{m}^2$  and the  $z$ -scale is 147 nm; (b) height profile of the corresponding image, the cone-like structures consist of 4 layers on top of the first layer; (c) AFM amplitude image (amplitude scale: 542 mV) of (a).



**Figure 3.7 (a)** Thickness/height of consecutive terraces/layers of a cone-like structure (moving away from the substrate), for two different PI-*b*-PEO diblock copolymers (asymmetric and symmetric).

Papadakis *et al.* [22] studied the morphology of spin cast thin films of asymmetric PI-*b*-PEO ( $f_{\text{PEO}} \approx 0.28$ ), on silicon wafers. They found the formation of hexagonally packed PEO cylinders (lying parallel to the substrate plain) in a PI matrix in their films on top of silicon wafer substrates after spin coating and short annealing times (several minutes). The cylinder PEO domains were not crystallised at this 'right after preparation' stage. However, several months later they found an amorphous flat layer formed on the substrate with a crystallised PEO dendrite layer forming on top surface. The initial hexagonal packed morphology was destroyed by the PEO crystallisation, resulting in crystalline lamellae structures, oriented parallel to the substrate. The crystallised dendrite layer was terraced (multi-lamellar structure). This very slow crystallisation process was explained in terms of the necessary significant mass transport that has to take place in order the terraced structured to be formed. Slow crystallisation is typical in similar systems [44]. In our case, we acquire similar terraced crystallised structures immediately after spin-

coating and drying. The reason for such an enhanced crystallisation process can be attributed to the strong hydrophilic nature of the freshly cleaved mica substrate along with the use of aqueous solutions and consequently the presence of water which aids in the attainment of such surface structures; such a system could accommodate an enhanced mass transport that is necessary for the crystallised terraced structures.

It is important to point out that our results cannot be explained by any swelling effects of the PEO block due to the water solutions used. Although water plays an important role in the formation of films its thickness on top of mica is of the range of 0.2 to 2 nm [71,72] and cannot result in a significantly swollen PEO block. In case of swelling, our symmetric polymer system ( $f_{\text{PEO}} = 0.49$ ) should have different morphological behaviour (behave like  $f_{\text{PEO}} \gg 0.5$ ), other than lamellae with equal thickness bilayers formed on top of the monolayer. Also, annealing the films above the melting temperature or leaving the films in ambient conditions for months did not produce any significant difference in the morphology of the structures which were proven thus, to be very robust.

For the symmetric polymer film and for larger APT (Figure 3.2h), the typical morphology involves extensive and uniform lamellar layers, covering large portions of the monolayer (which covers the whole mica surface). Holes give details for the number of layers formed on the monolayer and indicate autophobic dewetting. A recent study from Zhang and *co-workers* [54] on the nearly symmetric poly(styrene)-block-poly( $\epsilon$ -caprolactone) diblock thin films, revealed that lamellae structures (although they usually appear after annealing) are in fact metastable structures,

resulting from the coupling of dewetting (autophobic behaviour) and microphase separation. However, although these structures are metastable, if one of the blocks is semi-crystalline, below  $T_m$ , they are robust [20,70].

For the  $f_{\text{PEO}} = 0.66$ , the mica substrate has been fully covered and the film structure consists of two to three dense dendrite layers formed on top of a dense dendritic monolayer with clear crystal boundaries (Figure 3.8a). The AFM image in Figure 3.8b highlights the 2D spherulitic-like morphology of this film. The morphology is spherulitic-like with radial centrosymmetric organization, typical for PEO-based systems [48,73,74]. These semi-crystalline structures indicate that the crystallised PEO block dominates the overall morphology of the film and the growth occurs along the mica surface. The abundance of crystallised PEO molecules led to the formation of stacks of ‘flat-on’ crystalline lamellae in accordance with the bulk properties of this polymer [17]. The ‘flat-on’ orientation of the crystalline lamella compares well with similar studies on thin films (thinner than 200 nm) [48,75]. The crystallisation of a lower PEO layer induces the crystallisation of the subsequent PEO layer, with the amorphous PI molecules lying within the crystallized layers [33,70,73]. Lamellar bilayers, guided by the crystallisation of the PEO were also observed at Neto *et al.* study in a PS-*b*-PEO system with  $f_{\text{PEO}} \approx 0.65$  [70].



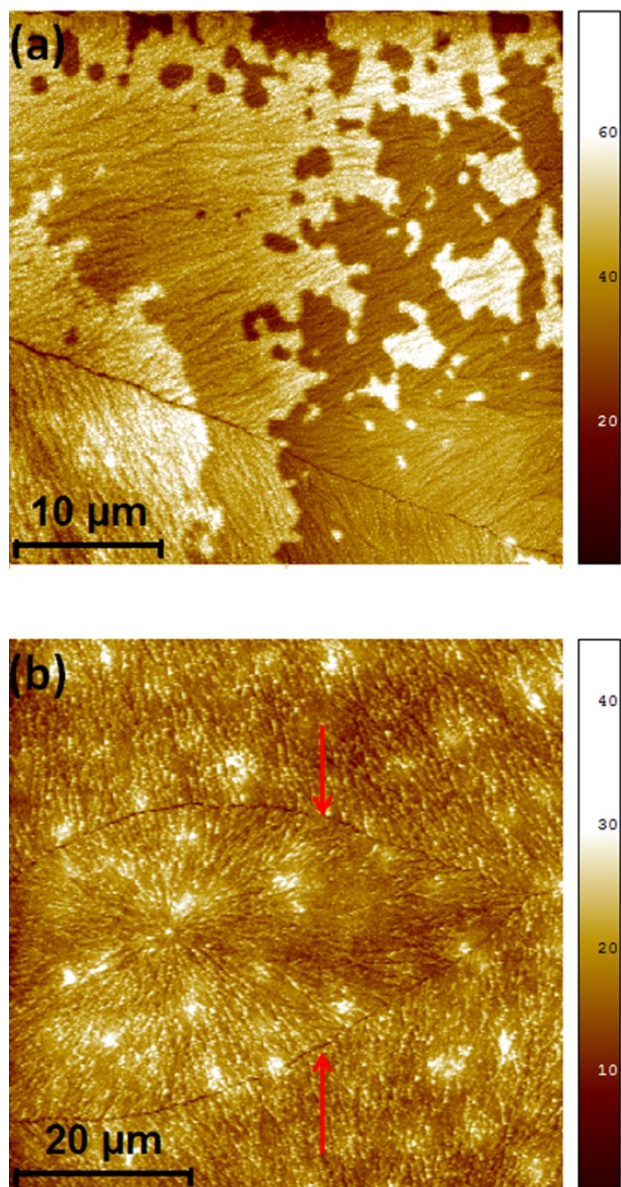


Figure 3.8 (a) (b) AFM topography images from different areas of the 41 nm film with  $f_{\text{PEO}} = 0.66$ . Note the dendrite layer observed inside a whole of the film in image (a). Arrows in image (b) indicate crystal boundaries (colour scales are in nanometres).

### 3.5 Conclusions

We studied the morphology of thin PI-*b*-PEO films prepared by spin-coating by varying the crystallisable/hydrophilic block (PEO) volume fraction and the concentration of the polymers in aqueous solutions. Stable ordered nanodomains



immediately after spin coating were observed in all cases, not affected by heating/annealing and ageing.

We have argued that the interactions between the hydrophilic mica surface and the hydrophilic PEO block played a crucial role and resulted in the collapse of the micelles and the formation of a crystallised dendritic thin monolayer on top of the mica. Our results are consistent with a monolayer consisting of a PEO layer of the same thickness in all cases (directly on top of mica) and a PI brush with a varying layer thickness. The growth of these patterns which started from the thicker areas of the film (which played the role of nucleation centres) is associated with a diffusion limited crystallisation mechanism. This mechanism can be slow and account for the varying lateral spreading of the monolayer during the rapid spin-coating.

In thicker areas, the excess of polymer material which did not wet the mica self-assembled into lamellae bilayers as result of the coupling between autophobic dewetting and phase separation behaviour. For the symmetric diblock copolymer ( $f_{\text{PEO}} = 0.49$ ) the preferred morphology are tall cone-like lamellae structures which are uniform and well-formed while for the asymmetric one with the lower PEO volume fraction ( $f_{\text{PEO}} = 0.32$ ) they deteriorate as we move away from the substrate. In the case of the asymmetric PI-PEO polymer with a higher PEO volume fraction ( $f_{\text{PEO}} = 0.66$ ) and for relatively high average polymer thickness, the morphology is characterised by laterally extensive stacks of flat-on (2D) lamellae crystallites on the surface.

The monolayer and bilayer lamellar thicknesses depend on PI-*b*-PEO composition, molecular weight and surface coverage (average polymer thickness) of each film. Increasing the concentration (and consequently the APT) causes the PI-PEO molecules to stretch away from the interface to avoid overlapping resulting in thicker layers.

A conclusion coming from the comparison between the three polymers is that the volume fraction of the PEO played a crucial role in the observed structures. At the highest concentration studied, the polymer with the lowest volume fraction of the PEO ( $f_{\text{PEO}} = 0.32$ ) formed dewetted cone-like patterns on top of the semi-continuous monolayer. The wetting increased with the increase of the volume fraction of the PEO ( $f_{\text{PEO}} = 0.49$ ) and lamellar layers were formed on top of a fully formed monolayer. Finally when the volume fraction of the PEO reached the maximum value studied herein ( $f_{\text{PEO}} = 0.66$ ) multi-crystalline lamellar structures have covered the substrate. The PEO content is crucial in determining the overall morphology of these kinetically trapped but robust structures.

The structures were formed right after the spin coating process, using aqueous solutions without the need of annealing. This is an intriguing result as self-assembled, robust structures based on block copolymers and produced by environmentally-friendly processing routes can be important for many applications. For example, exploiting the biocompatibility of the PEO block and the coupling between microphase separation and dewetting in thin films, in combination with the

PEO crystallinity, robust patterns with useful biological/biomedical properties can be produced by water-processing alone.

### 3.6 References

1. Hamley IW. *The Physics of Block Copolymers*. Oxford: Oxford University Press, 1998.
2. Russell TP. *Science* 2002;297(5583):964-967.
3. Cheng JY, Ross CA, Smith HI, and Thomas EL. *Advanced Materials* 2006;18(19):2505-2521.
4. Park C, Yoon J, and Thomas EL. *Polymer* 2003;44(22):6725-6760.
5. Khor HL, Kuan Y, Kukula H, Tamada K, Knoll W, Moeller M, and Hutmacher DW. *Biomacromolecules* 2007;8(5):1530-1540.
6. Kim H-C, Park S-M, and Hinsberg WD. *Chemical Reviews* 2009;110(1):146-177.
7. Ho R-M, Tseng W-H, Fan H-W, Chiang Y-W, Lin C-C, Ko B-T, and Huang B-H. *Polymer* 2005;46(22):9362-9377.
8. Templin M, Franck A, Du Chesne A, Leist H, Zhang Y, Ulrich R, Schädler V, and Wiesner U. *Science* 1997;278(5344):1795-1798.
9. Leibler L. *Macromolecules* 1980;13(6):1602-1617.
10. Bates FS and Fredrickson GH. *Annual Review of Physical Chemistry* 1990;41(1):525-557.
11. Huang S, Jiang S, Chen X, and An L. *Langmuir* 2009.
12. Huang Y, Liu X-B, Zhang H-L, Zhu D-S, Sun Y-J, Yan S-K, Wang J, Chen X-F, Wan X-H, Chen E-Q, and Zhou Q-F. *Polymer* 2006;47(4):1217-1225.

13. Moreno-Flores S, Nehring R, Raiteri R, and Meier W. *Macromolecules* 2009;42(23):9332-9337.
14. Nandan B, Lee CH, Chen HL, and Chen WC. *Macromolecules* 2006;39(13):4460-4468.
15. Nandan B, Hsu JY, and Chen HL. *Polymer Reviews* 2006;46(2):143-172.
16. Floudas G, Ulrich R, and Wiesner U. *Journal of Chemical Physics* 1999;110(1):652-663.
17. Floudas G, Vazaiou B, Schipper F, Ulrich R, Wiesner U, Iatrou H, and Hadjichristidis N. *Macromolecules* 2001;34(9):2947-2957.
18. Russell TP, Coulon G, Deline VR, and Miller DC. *Macromolecules* 1989;22(12):4600-4606.
19. Green PF. *Journal of Polymer Science Part B-Polymer Physics* 2003;41(19):2219-2235.
20. Li Y, Loo Y-L, Register RA, and Green PF. *Macromolecules* 2005;38(18):7745-7753.
21. Turner MS, Rubinstein M, and Marques CM. *Macromolecules* 1994;27(18):4986-4992.
22. Papadakis CM, Darko C, Di Z, Troll K, Metwalli E, Timmann A, Reiter G, and Forster S. *European Physical Journal E* 2011;34(1).
23. Glynos E, Pispas S, and Koutsos V. *Macromolecules* 2008;41(12):4313-4320.

24. Lee JH, Lee HB, and Andrade JD. *Progress in Polymer Science* 1995;20(6):1043-1079.
25. Liu VA, Jastromb WE, and Bhatia SN. *Journal of Biomedical Materials Research* 2002;60(1):126-134.
26. Saffer EM, Tew GN, and Bhatia SR. *Current Medicinal Chemistry* 2011;18(36):5676-5686.
27. Dormidontova EE. *Macromolecules* 2001;35(3):987-1001.
28. Pispas S and Hadjichristidis N. *Langmuir* 2003;19(1):48-54.
29. Pispas S and Sarantopoulou E. *Langmuir* 2007;23(14):7484-7490.
30. Magonov SN, Elings V, and Whangbo MH. *Surface Science* 1997;375(2-3):L385-L391.
31. Magonov SN and Reneker DH. *Annual Review of Materials Science* 1997;27:175-222.
32. Godehardt R, Lebek W, Adhikari R, Rosenthal M, Martin C, Frangov S, and Michler GH. *European Polymer Journal* 2004;40(5):917-926.
33. Reiter G and Vidal L. *European Physical Journal E* 2003;12(3):497-505.
34. Hadjichristidis N, Iatrou H, Pispas S, and Pitsikalis M. *Journal of Polymer Science Part A: Polymer Chemistry* 2000;38(18):3211-3234.
35. Pispas S. *Journal of Polymer Science Part A: Polymer Chemistry* 2006;44(1):606-613.
36. Ligoure C. *Macromolecules* 1991;24(10):2968-2972.

37. Connell SD, Collins S, Fundin J, Yang Z, and Hamley IW. *Langmuir* 2003;19(24):10449-10453.
38. Geke MO, Shelden RA, Caseri WR, and Suter UW. *Journal of Colloid and Interface Science* 1997;189(2):283-287.
39. Liang G-D, Xu J-T, Fan Z-Q, Mai S-M, and Ryan AJ. *Polymer* 2007;48(24):7201-7210.
40. Surin M, Marsitzky D, Grimsdale AC, Müllen K, Lazzaroni R, and Leclère P. *Advanced Functional Materials* 2004;14(7):708-715.
41. Meiners JC, Ritzi A, Rafailovich MH, Sokolov J, Mlynek J, and Krausch G. *Applied Physics A: Materials Science & Processing* 1995;61(5):519-524.
42. Xu L, Lio A, Hu J, Ogletree DF, and Salmeron M. *The Journal of Physical Chemistry B* 1998;102(3):540-548.
43. Brandrup J, Immergut EH, Grulke EA, and (Editors). *Polymer Handbook*, 4 ed. Hoboken, NJ: Wiley, 1999.
44. Reiter G, Castelein G, Hoerner P, Riess G, Sommer JU, and Floudas G. *European Physical Journal E* 2000;2(4):319-334.
45. Milner ST. *Science* 1991;251(4996):905-914.
46. Takahashi Y and Tadokoro H. *Macromolecules* 1973;6(5):672-675.
47. Reiter G and Sommer J-U. *The Journal of Chemical Physics* 2000;112(9):4376-4383.

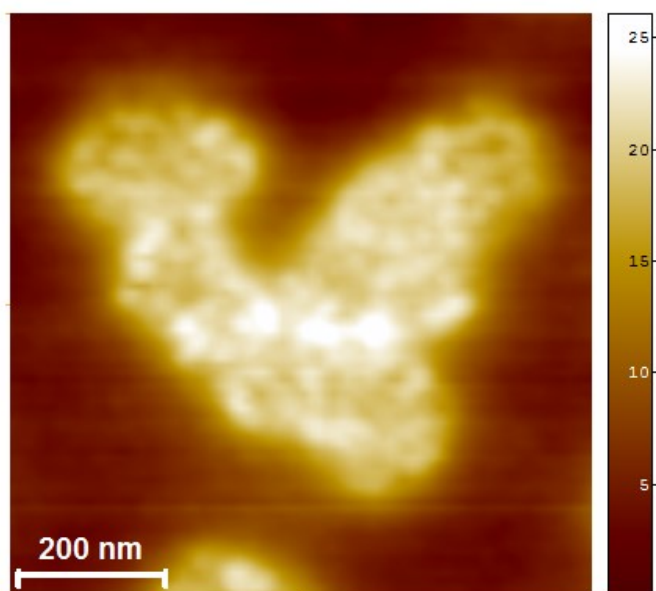
48. Liu Y-X and Chen E-Q. *Coordination Chemistry Reviews* 2010;254(9-10):1011-1037.
49. Reiter G and Sommer J-U. *Physical Review Letters* 1998;80(17):3771.
50. Sommer J-U and Reiter G. *Journal of Chemical Physics* 2000;112(9):4384-4393.
51. Witten TA and Sander LM. *Physical Review Letters* 1981;47(19):1400.
52. Witten TA and Sander LM. *Physical Review B* 1983;27(9):5686.
53. Green PF and Limary R. *Advances in Colloid and Interface Science* 2001;94(1-3):53-81.
54. Zhang P, Wang Z, Huang H, and He T. *Macromolecules* 2012.
55. Hare EF and Zisman WA. *Journal of Physical Chemistry* 1955;59(4):335-340.
56. Gennes P-Gd, Brochard-Wyart, Françoise, Quere, David. *Capillarity and wetting phenomena: drops, bubbles, pearls, waves*. New York: Springer, 2004.
57. Shull KR. *Faraday Discussions* 1994;98:203-217.
58. Reiter G and Khanna R. *Physical Review Letters* 2000;85(26):5599-5602.
59. Kerle T, Yerushalmi-Rozen R, and Klein J. *Macromolecules* 1998;31(2):422-429.
60. Pastorino C, Binder K, Kreer T, and Muller M. *The Journal of Chemical Physics* 2006;124(6):064902.



61. Beziel W, Reiter G, Drockenmuller E, Ostaci RV, Al Akhrass S, Cousin F, and Sferrazza M. *Epl* 2010;90(2).
62. Croll AB, Massa MV, Matsen MW, and Dalnoki-Veress K. *Physical Review Letters* 2006;97(20).
63. McGraw JD, Rowe IDW, Matsen MW, and Dalnoki-Veress K. *The European Physical Journal E* 2011;34(12):1-7.
64. Kim JU and Matsen MW. *Soft Matter* 2009;5(15):2889-2895.
65. Zhao Y-L, Erina N, Yasuda T, Kato T, and Stoddart JF. *Journal of Materials Chemistry* 2009;19(21):3469-3474.
66. Hashimoto T, Shibayama M, and Kawai H. *Macromolecules* 1980;13(5):1237-1247.
67. Tamayo J and García R. *Langmuir* 1996;12(18):4430-4435.
68. Evangelopoulos AEAS, Glynos E, Madani-Grasset F, and Koutsos V. *Langmuir* 2012;28(10):4754-4767.
69. Vasilev C, Reiter G, Pispas S, and Hadjichristidis N. *Polymer* 2006;47(1):330-340.
70. Neto C, James M, and Telford AM. *Macromolecules* 2009;42(13):4801-4808.
71. Hu J, Xiao XD, Ogletree DF, and Salmeron M. *Surface Science* 1995;344(3):221-236.
72. Hu J, Xiao X-D, Ogletree DF, and Salmeron M. *Science* 1995;268(5208):267-269.

73. Hong S, MacKnight WJ, Russell TP, and Gido SP. *Macromolecules* 2001;34(8):2398-2399.
74. Huang S, Jiang S, Chen X, and An L. *Langmuir* 2009;25(22):13125-13132.
75. Mareau VH and Prud'homme RE. *Macromolecules* 2005;38(2):398-408.
76. Xu P, Tang H, Li S, Ren J, Van Kirk E, Murdoch WJ, Radosz M, and Shen Y. *Biomacromolecules* 2004;5(5):1736-1744.
77. Robinson DN and Peppas NA. *Macromolecules* 2002;35(9):3668-3674.
78. Zhang R, Seki A, Ishizone T, and Yokoyama H. *Langmuir* 2008;24(10):5527-5533.
79. Zhao J, Mountrichas G, Zhang G, and Pispas S. *Macromolecules* 2009;42(22):8661-8668

## Chapter 4 Thin Films of Conjugated Polymer Blends



AFM height image of F8BT:TFB 1:2 polymer blend thin film (colour scale units are in nm).

## 4.1 Introduction

Conjugated polymer blends are organic semiconductors that have proved to be excellent alternatives to inorganic semiconductors for use in devices such as photovoltaic and light emitting diodes [1]. The much less complicated techniques to mix and prepare thin films of conjugated polymers compared with the high-energy, sophisticated and expensive preparation techniques of the inorganic competitors, in combination with the very good electroluminescence efficiency are the reasons which made conjugated polymers very popular.

Burroughes *et al.* [2], have first reported electroluminescence produced from a polymer based diode using poly(phenylene vinylene) (PPV). Since then, several other polymer-based diodes were investigated for their electroluminescence efficiency. Polyfluorene-based conjugated blends are one of the most popular organic semiconductors, exhibiting great semiconducting performance [3] and achieving the production of the first full colour displays [4]. More precisely thin films of the electron-transporting F8BT [poly(9,9-dioctylfluorene-*co*-benzothiadiazole)] and hole-transporting TFB poly[9,9-dioctylfluorene-*co*-N-(4-butylphenyl)-diphenylamine] polymer blends as active materials in LEDs have been very successful in improved device efficiency, such as higher electroluminescence (higher than 18 lm/W) and outstanding firmness under long-lasting process (more than 5,000 h at 100 cd/m<sup>2</sup>) [5,6].

The structural behaviour of F8BT:TFB polymer blends in thin films determines the overall performance and function of the devices [7]. For that reason the extensive

and in depth study of the mixing, solubility and phase-separation behaviour is of paramount importance. Kim and *co-workers* have studied the phase separation behaviour of F8BT:TFB blends [7]. Furthermore, Yim and *co-workers* have lately reported that F8BT and TFB polymer blends with at least one molecular weight  $M_n < 10$  kg/mol do not exhibit any measureable lateral phase-separated structures [3]. However, they used polymer pairs with a substantial difference between their molecular weights. Furthermore, there are still several questions which were left unanswered, such as the effect of the concentration, spin-coating speed and annealing.

In this chapter, we show that F8BT:TFB polymer blend thin films with both  $M_n < 10$  kg/mol exhibit sub-micrometre and nano-scale phase-separation. A large number of samples were prepared from *p*-xylene solutions of 14 mg/ml and 20 mg/ml and the weight (w/w) blend ratio varied from 0:1 to 1:4 and from 1:0 to 4:1. The spin coating speed was varied from 2,000 to 5,000 rpm. Finally the annealing process was applied to a few of the thin films.

We found for the first time and present the formation of sub-micrometre length scale phase-separated domains in F8BT:TFB thin films with blend ratios 1:1, 1:2, 1:3 and 1:4 for both solution concentrations with  $M_n < 10$  kg/mol. Sub-micrometre phase separated domains have been reported only in F8BT:TFB 3:1 thin films (in thin films with significantly higher molecular weights) [7].

Two different phase-separation trends were found, one for 1:1 thin films which is caused due to spinodal decomposition and one for 1:2, 1:3 and 1:4, the cause of

which is nucleation and growth. Although it is known that the phases are not completely pure, we are the first to present high resolution AFM images showing the structure of the impurities (nano-phase separation) in the F8BT:TFB thin films with 1:4 blend ratio. The spin coating speed and concentration do not appear to affect the structures laterally in a substantial degree, however there are some important changes noted in the vertical sizes of the domains. Furthermore, the evolution of the structures from 1:2 to 1:4 blends was also extensively investigated.

## **4.2 Background**

### **4.2.1 Semiconductor Materials and Light Emitting Diodes**

Materials which have conductivity that lies between that of conductors and non-conductors (insulators) are known as semiconductors. Conventional semiconductors are made by single inorganic crystalline materials such as silicon and germanium, or compounds such as cadmium selenide or gallium arsenide. The basic characteristics of the semiconductors are the well-defined optical properties such as the bandgap and electrical properties such as the conductivity, mobility and electron affinity. The conductivity of the semiconductors originates from the free mobility of the electrons and the holes (absence of electrons). The conductivity properties of the semiconductors can be modified by doping the materials with the appropriate dopants (electrons or holes). In the case where a semiconductor is doped with excess of electrons it is called *n*-type semiconductor, while in the case where it is doped with excess of holes, the semiconductor is called *p*-type.

The semiconductor devices usually include junctions of  $n$ -type and  $p$ -type semiconductors. A typical example of a single  $p$ - $n$  junction is the light emitting diode (LED). LED semiconductor devices are low-voltage light sources (compared with the conventional light sources) widely used in our everyday life (flat panels, visual signals) and in industry (aviation lighting, automotive lighting, sensors, LED printers etc). LEDs emit light through the phenomenon of electroluminescence. As shown in the schematic of Figure 4.1, when the diode is biased (current flows), electrons from the  $n$ -type semiconductor recombine with holes from the  $p$ -type, producing photons i.e. light. The exact colour of the light depends on the band gap (the gap between the conduction and the valance band) of the semiconductor device. In order for the LED to achieve the desirable optical properties, the semiconductors inside the LED need to be doped with electron or holes as mentioned above. For example when the semiconductor  $\text{In}_2\text{O}_3$  is doped with Sn, a transparent conductive semiconductor material is formed with great applications in optoelectronics. However mixing and doping the inorganic semiconductors requires high energy and complicated techniques which are not cost-effective.

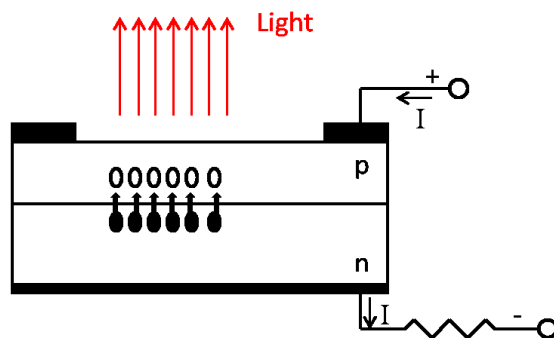


**Figure 4.1** Schematic representation of the electroluminescence process in an inorganic-based only light emitting diode.

Molecular materials, on the other hand, can be synthesized and mixed to create the desirable semiconductor properties through easier and less expensive techniques compared to inorganic semiconductors. The wide variety of molecular materials with semiconductor properties (in combination with the constant need for smaller and lower-cost devices) has made them promising candidates for replacing the expensive inorganic semiconductors. Single-molecule devices with wire, rectifiers, storage and switching properties have been successfully demonstrated that can substitute the silicon technology [8]. Furthermore, over the last years, small-molecule technology (or vacuum-deposited molecular layers) [9], as well as polymer technology (or conjugated polymers) [2], have been great competitors in performance and efficiency with the inorganic crystalline semiconductors in fields such as the display industry [10]. However the vacuum-deposited molecular layer technology has been proven to exhibit a long-term instability (re-crystallisation and other structural changes). A way to overcome this structural instability is to move from molecular to macromolecular materials. Conjugated polymers could offer both good charge transfer and stability over long times [2].

#### **4.2.2 Conjugated Polymers**

Conjugated polymers are organic semiconductors; the semi-conducting behaviour originates from the delocalised  $\pi$ -electron bonding in their backbone structure. Friend *et al.* [11] in their review article describe the process as follows: “The  $\pi$  bonding and the  $\pi^*$  antibonding orbitals form delocalised valence and conduction wavefunctions, which support mobile charge carriers.” The polymeric properties of this type of semiconductors lead to the formation of more flexible,



robust structures, increased device efficiency, improved overall performance [12] and at the same time lower-cost manufacturing using solution-processing of film-forming polymers [13], compared with the inorganic semiconductors. For these reasons LEDs and photovoltaic diodes or photodiodes (PD, convert light into current or voltage; the opposite process of a LED) consisting of conjugated polymer-based thin films have received considerable attention over the last decade [1,7,14,15]. A typical polymer LED/PD is made from a polymer film as the active layer sandwiched between an anode (ITO) and a cathode (metal). Usually the polymer film is a blend of an A and a B conjugated polymer. The A polymer is *n*-type (donor) semiconductor and the B polymer is *p*-type (acceptor) semiconductor. Figure 4.2 presents a schematic representation of a typical PD. The morphological behaviour when the two polymers are blended to produce the polymer-based active layer plays a crucial role in the overall efficiency and performance of the diodes [7]. Therefore, it is of paramount important to understand in depth the polymer structures formed on solid surfaces on the nano-scale.

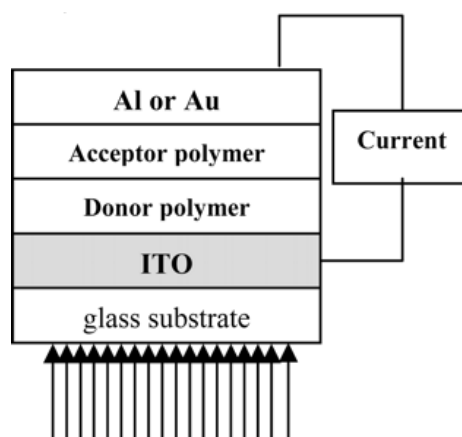


**Figure 4.2** Schematic cross section of the layered donor/acceptor polymer photovoltaic cells; image is taken from Alam and *co-workers* [15].

The technique used the most for processing the conjugated polymers is blending, where two or more polymers are mixed in order to achieve discrete morphology and physical properties of the polymeric mixture in the solid state, without the synthesis of new polymers [1]. Phase-separated structures resulting from demixing of the conjugated polymers determine the ultimate optoelectronic performance of the devices. Therefore it is crucial to achieve control of the phase-separation, in order to develop devices with the desired properties. Phase-separation in conjugated polymer blends usually occurs after solvent quenching, where the polymers are dissolved in a non-selective solvent and form a homogeneous solution, which phase-separates when the solvent evaporates from the solution. When the blended polymer solution is being transferred onto a solid substrate, usually via spin-coating [16] an ultrathin or thin film forms. Polymer-blend thin films, typically exhibit different compositions to the compositions they exhibit in the bulk, because each component tends to have different surface energy (and thus different interactions with the substrate and the free interface). The phase-separated domains can have a circular-like shape of one phase in a homogenous matrix of the other phase [1]. The circular-like shape can be either island-like (extended out of the surface) or well-like (extended into the film) [17]. The resulting film morphology and the phase-separated domain size are highly affected by factors such as the polymer blend ratio (the polymers mass fraction in the blend), the solvent, the spin coating parameters (spin speed, time) and the nature of the substrate [1]. In this study we considered the effect of the polymer blend ratio, spin speed and time in various blend ratios of a given conjugated polymer blend.

### 4.2.3 Polyfluorene-Based Conjugated Polymer Blends

Since the first report in the 1970s that polymers can be conductive (Nobel Prize in Chemistry 2000) [18], a new area of interest in polymer technology was born. Electroluminescence from a polymer based diode using poly(phenylene vinylene) (PPV) was first reported by Burroughes *et al.* [2]. Since this seminal work, considerable progress was made with tuning the conjugated polymer properties to achieve increased conductive, emissive and electroluminescence efficiency. In particular blue emission was achieved making possible the production of full colour displays with the use of poly(fluorene)-based conjugated polymer blends [4].

The phase-separation behaviour of thin films made by poly(fluorene)-based conjugated polymer blends, which exhibit photo-induced charge transfer and photovoltaic performance has been extensively investigated by the Friend group at the Cavendish Laboratory [3,5,7,14,19-23]. Arias *et al.* [20] studied the morphology and performance of conjugated polymer blended thin films consisted by F8BT [poly(9,9-dioctylfluorene-*co*-benzothiadiazole)] and PFB [poly(9,9-dioctylfluorene-*co*-bis-*N,N*-(4-butylphenyl)-bis-*N,N*-phenyl-1,4-phenylenediamine)] parts on an ITO substrate. They used scanning probe microscopy techniques to study the structural behaviour of the films, which influences the performance of polyfluorene blend-based devices. They found that by varying the solvent, the substrate temperature and the saturation of the atmosphere over the film, the phase-separated domain sizes could be varied from tens of nanometres up to tens of microns. In addition they found that the nanoscale sized phase-separated structures, produced by rapid solvent evaporation (in this case chloroform) during spin coating, led to more efficient

photovoltaic performance. The performance of vertically segregated LEDs and the effect of the structural behaviour on device performance was also studied by Corcoran *et al.* [21] using the same method as Arias *et al.* [20]. They used blended films consisted of the electron transporting polymer F8BT and the hole-transporting polymer poly[9,9 -dioctylfluorene-coN-(4-butylphenyl)-diphenylamine] (TFB) on poly(styrenesulfonate)-doped poly(3,4-ethylenedioxythiophene) PEDOT:PSS coated ITO substrates. The effect of the solvent and the spinning conditions can be used to control the phase-separation in the F8BT:TFB polymer blend films. Vertically segregated light emitting diodes by F8BT:TFB blends have been fabricated with increased device efficiency relative to laterally phase-separated devices.

Thin films of F8BT:TFB polymer blends as active materials in LEDs have been very successful in improved device characteristics, such as higher electroluminescence (higher than 18 lm/W) and outstanding firmness under long-lasting use (more than 5,000 h at 100 cd/m<sup>2</sup>) [5,6]. More precisely, the F8BT:TFB blend with 1:1 w/w, was found to produce LEDs with remarkably high brightness and efficiency, even at low operational voltage [24,25]. The light emission kicks in at operational voltages of 1.9 V with a peak efficiency of 16 lm/W, at 2.2 V and 100 cd/m<sup>2</sup>. The level of the luminescence was found at 1,000 cd/m<sup>2</sup>, obtained at 2.4 V and at 30,000 cd/m<sup>2</sup> at 5 V [24,26].

First AFM investigations of the morphology of spin-cast F8BT:TFB blend thin films with 1:1 weight ratio have revealed that the surface consists of micrometre-size well-like domains (dark wells) in a homogeneous phase (bright areas) [24,25,27]. Increasing the weight fraction of the TFB part, island-like domains

extending out of a homogenous layer were formed. On the other hand, for higher weight fraction of the F8BT polymer, the thin film morphology is characterised by sub-micrometre well-like domains (200 – 300 nm diameter for 2:1 w/w). Furthermore, the molecular weight of the polymer was also found to affect the film morphology [24,28].

Later, Kim *et al.* [7] has extensively studied the spin-cast thin film morphology of F8BT:TFB blended polymers, dispersed in *p*-xylene solutions onto ITO substrates by AFM, micro-Raman spectroscopy and X-ray photoelectron spectroscopy (XPS). They have experimentally determined the phase diagram of a F8BT:TFB:*p*-xylene ternary blend system at 22 °C, which is a useful tool for predicting the thin-film formation during the spin-coating process (Figure 4.3). Their study showed that the TFB part is more soluble in *p*-xylene than the F8BT part, which exhibits a limited solubility (~ 3.5%) in this solvent; we also note that the F8BT part has a higher surface energy (40–45 mJ/m<sup>2</sup>) than the TFB (35–40 mJ/m<sup>2</sup>) [7,29]. According to these solubility trends, during solvent evaporation an F8BT-rich phase will form at an early stage. As the concentration of the polymer in the system increases, two phases would form. One would be F8BT-rich and the other would be TFB-rich. In further compositional analysis Kim *et al.* have studied these micron-scale lateral phase-separated domains, using micro-Raman spectroscopy. These domains are not pure at the nanoscale. Furthermore, vertical phase segregation also occurred, with the TFB part which has the lower surface energy segregating at both air and substrate interfaces. Kim *et al.* [7], who have performed XPS and variable photoelectron takeoff-angle experiments on the ITO side of the F8BT:TFB 3:1 thin film, claimed

that the preference of the TFB polymer to wet the substrate might be related to the solvent concentration gradient across the film thickness during the solvent evaporation process. Furthermore, the enrichment of the TFB polymer (which has lower surface energy) in the interfaces and the depletion of the F8BT, which has higher surface energy than the TFB from the film interfaces, are consistent with the thermodynamic driving force to reduce the interface energies, in (otherwise) weak substrate-polymer interactions.

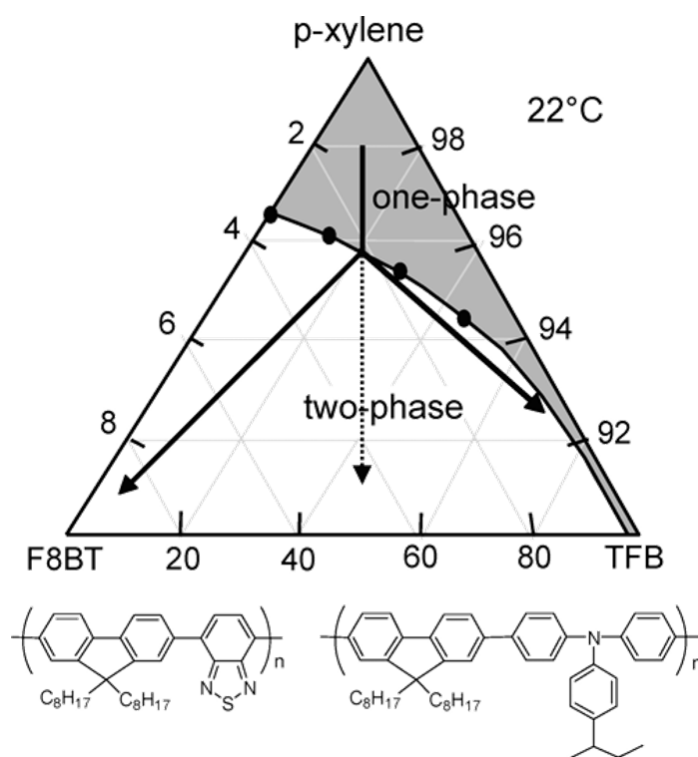


**Figure 4.3** Phase diagram for the ternary blend system, F8BT + TFB + *p*-xylene, obtained by Kim *et al.* [7].

Kim *et al.* suggested a typical polymer concentration of 10–20 mg/ml and spin casting to achieve a final film thickness of 100 nm. Based on their observations, they have also proposed a simple model for the evolution of structure of the F8BT:TFB blend thin films during spin-coating (Figure 4.4), which is crucial for the ultimate

performance of the conjugated-based LEDs. As presented at Figure 4.4, when the substrate starts to spin the solution would spread over the substrate to the edges (step 1). As the solvent evaporates and in accordance with the phase diagram of Figure 4.3, the F8BT-rich + solvent regions will phase-separate at low solid contents (step 2). For blends with 1:1 ratio this process will occur via the spinodal decomposition (i.e. initiated by density fluctuations of the respective polymer concentrations), whilst for compositions that are strongly enriched in one or the other polymer, the process would be initiated by nucleation and growth of specific polymer-rich areas. As more solvent evaporates, the phases continue to eject the 'guest' polymer material; however some of this material is entrapped as smaller domains into the larger phase-separated domains, until the system reaches the glass transition temperature ( $T_g$ ), which results in polymer chain motions stopping and the existing structure freezes (step 3). After this step the solvent continues to evaporate, however the phase-separated morphologies were already determined. The final film structure (step 4) for the particular example of low F8BT content blends, comprises of a crater-like surface, probably due to the pinning of the triple-phase boundary (F8BT-rich, TFB-rich and air) while the solvent continues to evaporate. XPS experiments have shown that a TFB wetting layer is formed at the film-substrate interface and the existence of a TFB capping layer on top of the F8BT-rich craters (film-air interface).

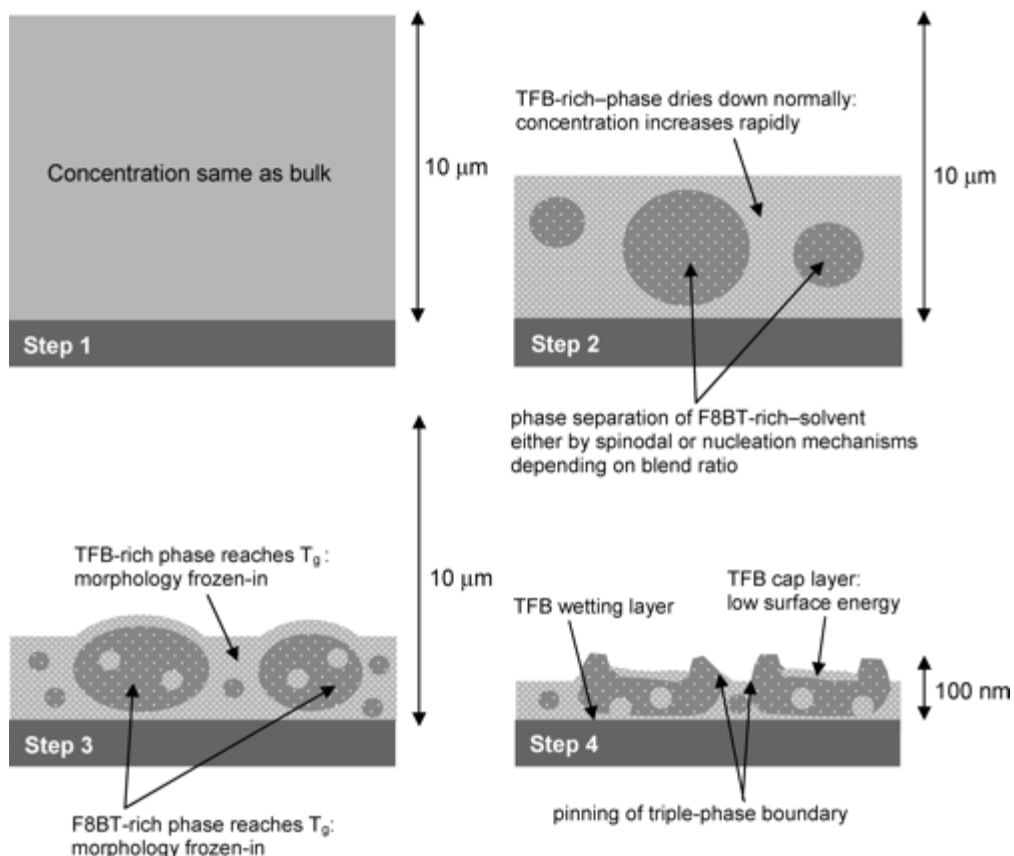


**Figure 4.4** Proposed model for the development of the thin-film phase-separated structure in F8BT:TFB blends during the spin coating process according to Kim *et al.* [7]: Step 1: spin-off, step 2: solvent evaporation, step 3: morphology frozen in, step 4: thin film formation.

Kim *et al.* [7] have also performed studies on junctions directly on ITO without applying a hole-injection/transporting layer (PEDOT:PSS), since the TFB wetting layer was found to be present at the anode interface (substrate). Results have shown that it is possible to prepare LEDs which include an ultrathin layer of F8BT:TFB polymer blend alone as efficient as with the existence of an additional PEDOT:PSS layer.

Later, Yim *et al.* [3], have performed studies on vertically and laterally phase-separated thin-film structures of F8BT:TFB blends with molecular weight variations as presented in Figure 4.5. For their study they used AFM, XPS and



photoluminescence (PL) spectroscopy techniques. They found that blend films that consist of at least one low molecular weight polymer ( $M_n < 10$  kg/mol, Figures 4.5a-g), show no micrometre lateral phase-separation. Only vertical phase segregation did occur, driven by the difference of the polymer molecular weights in the blends. They stated that the film-air interface was found to be enriched by the lower molecular weight polymer (i.e. shorter length) polymer, due to the surface free energy of end groups and conformational entropy factors [3]. On the other hand, when there are no low molecular weight polymers in the blend, micrometre lateral phase-separation was observed (Figures 4.5e, f, h and i). However, neither Yim *et al.* nor Kim *et al.* have performed studies on F8BT:TFB polymer blends with similar and at the same time low molecular weights ( $M_n < 10$  kg/mol). The use of low molecular weight polymers in the polymer blend could be beneficial for maintaining high efficiency of the devices at high drive voltages [3]. More precisely, the TFB which is an amorphous polymer with bulky and twisted triarylamine units in the backbone, exhibits gradual decrease in the hole mobility with increasing its molecular weight [3]. Thus, the extensive study of thin film morphologies in this direction is of paramount importance.

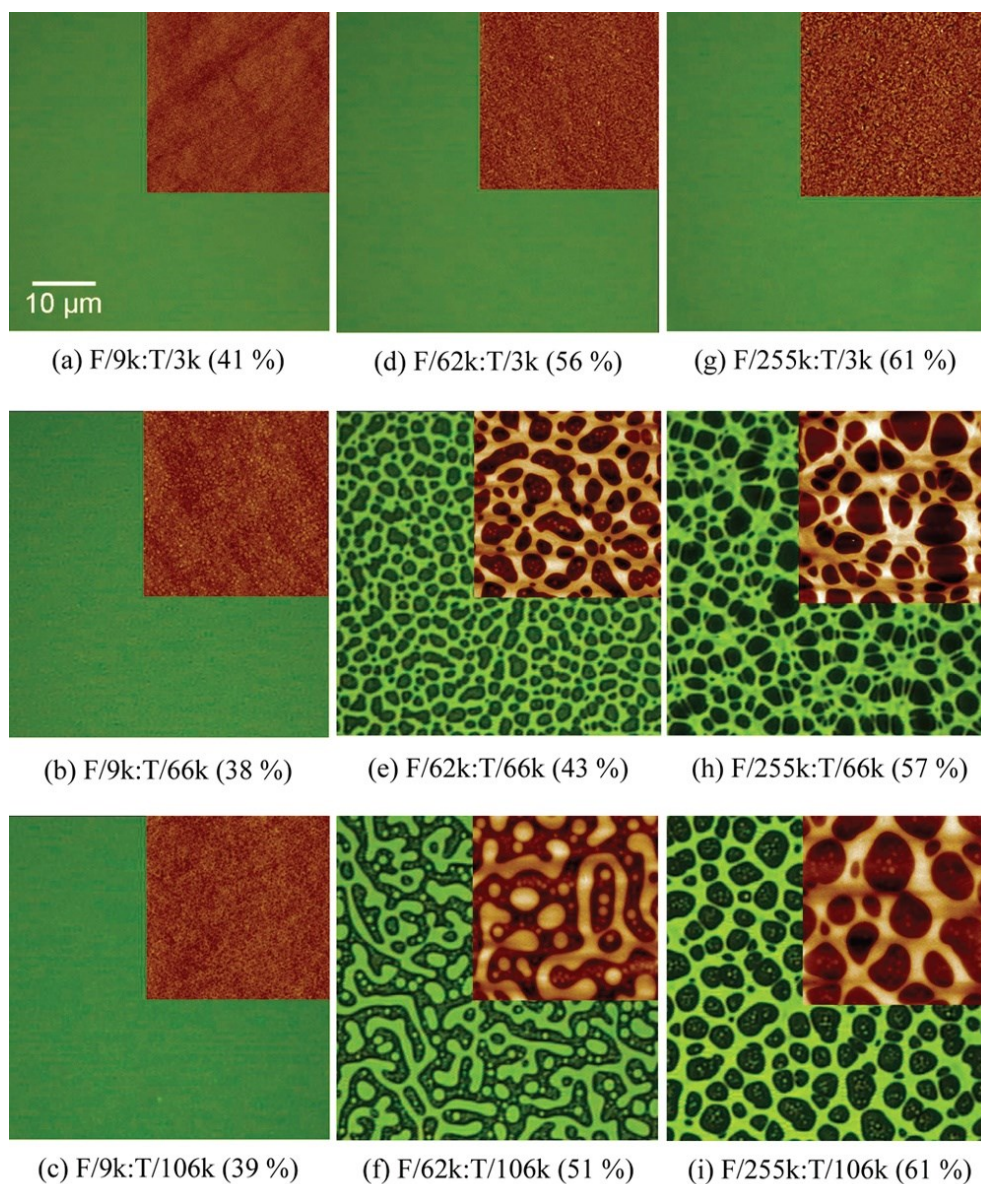


**Figure 4.5 (a-i) Photoluminescence (PL) images of ca. 80-100 nm thick F8BT:TFB blend films (1:1 by weight) with different molecular weights of each homopolymer, under blue excitation (2.85 eV). The bright regions in these PL images correspond to F8BT-rich phases while the dark regions correspond to TFB-rich phases. The corresponding AFM images ( $20 \mu\text{m} \times 20 \mu\text{m}$ ) are included in the insets. AFM images in (a-d) and (g) are on a 20 nm height scale, while those in (e), (f) (h), and (i) are on a 70 nm height scale. No measurable lateral phase-separation in (a-d) and (g) within the resolution of both PL and AFM images here. The PL efficiency values (%) of the blend films are also shown (Figure and the Figure caption obtained from Yim *et al.* [3]).**

Owing to the great advantages that the thin films of F8BT:TFB polymer blends exhibit in LED fabrication and the effect of the phase-separation behaviour in the overall performance of the LEDs, we applied atomic force microscopy and transmission electron microscopy techniques to further study this polymer system. The size of the domains appears to be extremely crucial for the ultimate performance and efficiency of the LEDs [3]. Both Yim and Kim *et al.* [3,7] used various substrates for the formation of thin films: pre-cleaned quartz substrates and oxygen-plasma cleaned ITO-coated glass substrates with or without a ~60 nm thick poly(styrene sulfonate)-doped poly(3,4-ethylene dioxythiophene) (PEDOT-PSS) layer. They have not reported any changes in morphology due to the difference in substrates. For our fundamental studies, we used freshly cleaved mica which is a hydrophilic high energy mineral surface (similar in this way to chemically cleaned Quartz or ITO) which has the extra advantage of being atomically flat allowing for smoother thin films which can aid in high resolution imaging with AFM.

We used the polymer blend ratios, solution concentration, spin coating parameters and the heat treatment, as tools to better understand the phase-separation behaviour of the spin cast blend films in the lateral direction. More precisely, we prepared a series of ultrathin films of low molecular weight F8BT:TFB polymer blends with concentration 20 mg/ml and 14 mg/ml, with various blend ratios ‘by weight’. Some of the films were annealed at 200 °C for 12 h after spin coating. We found sub-micrometre lateral phase-separated domains (50–500 nm) in the as spin cast thin films of F8BT:TFB polymer blends. We present the fine details of the morphology of the domains in the nano-scale for the first time. The exact structural

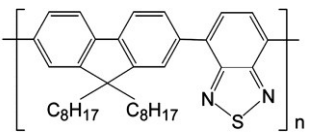
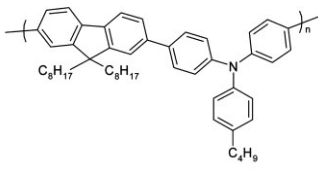
behaviour was found to be strongly dependent on the weight fractions of the F8BT and TFB blends.

### 4.3 Experimental

#### 4.3.1 Materials

The conjugated polymer blends studied consisted of F8BT (poly[9,9-dioctylfluorene-*co*-benzothiadiazole]) parts ( $M_n = 6.2$  kg/mol) and TFB (poly[9,9-dioctylfluorene-*co*-N-(4-butylphenyl)-diphenylamine]) parts ( $M_n = 5.8$  kg/mol), whose chemical structures are presented in Table 4.1. Polymers were purchased by American Dye Source, Inc. (Quebec, Canada). F8BT is an electron mobility polymer (*n*-type) [30,31] and TFB is a high hole mobility polymer (*p*-type) [32].

**Table 4.1 Properties and Chemical Properties of the Polymers Studied**

Polymer	$M_n^a$ (kg/mol)	Polydispersity	Chemical Structure
F8BT	6.2	7.4	
TFB	5.8	2.6	

<sup>a</sup> From gel permeation chromatography (GPC)

#### 4.3.2 Polymer Solutions and Thin Films Preparation

Polymer solutions were prepared by dissolving each conjugated polymer in *p*-xylene purchased by Sigma-Aldrich Ltd. (Dorset, UK) to produce concentrations of 20 mg/ml and 14 mg/ml. F8BT and TFB solutions were then mixed to produce

blends of various ratios from 4:1 to 1:4 by weight. The mixed solutions were placed on stirring/hot plate at 50 °C and 800 rpm and left overnight. The following day, droplets of the blended solutions (approximately 1 ml) were spin coated (spin coater SPIN150-NPP, SPS-Europe, Putten, the Netherlands) on freshly cleaved mica sheets (Agar Scientific, Essex, UK) in ambient conditions, producing ultrathin films (50–100 nm). The spin-coating speed was varied from 2,000 to 5,000 rpm while durations of 90 seconds were used. For 2,000 rpm thin films of thickness ~ 100 nm were produced, while for 4,000 and 5,000 rpm, 70 nm and 55 nm thin films were produced respectively. The film thickness values are in accordance with McNeill and *co-workers* study on thin films of F8BT:TFB blends [33]. The films were aged at room temperature for an average of 3 hours before characterisation. In one case we altered the spin coating duration from 90 to 30 seconds which did not provide different results while some of the ultra-thin films were annealed at 200 °C for 12 hours or longer resulting in a substantial alteration of the morphology. In the schematic of Figure 4.6, all the different thin-films prepared are presented.

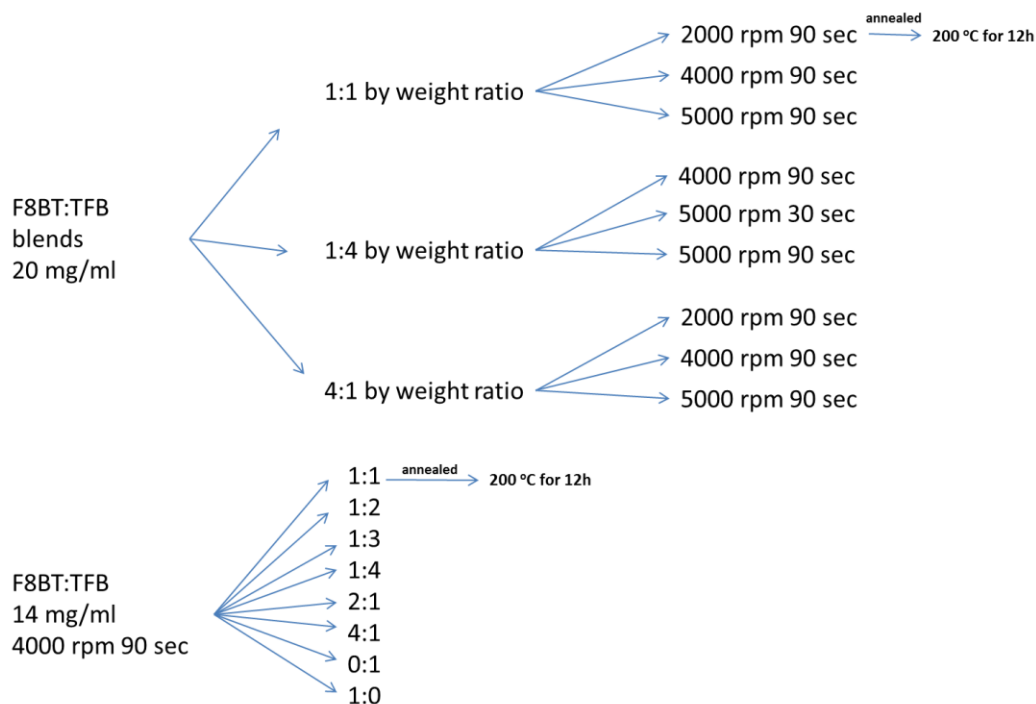


**Figure 4.6** The conjugated F8BT:TFB polymer blend ultra-thin films prepared with concentrations 20 mg/ml and 14 mg/ml in different by weight blend ratio, spin coating parameters and in some occasions heat treatment.

### 4.3.3 Atomic Force Microscopy

A Bruker AFM Multimode/Nanoscope IIIa (Bruker, Santa Barbara, CA, USA), equipped with a *J*-scanner ( $x$ - $y$  range  $\approx 140$   $\mu\text{m}$ ) and/or an *E*-scanner ( $x$ - $y$  range  $\approx 12$   $\mu\text{m}$ ) was used to study the morphological behaviour of the F8BT:TFB blends ultrathin films. RTESP and/or RTESPA Bruker cantilevers with a nominal spring constant and resonance frequency of 40 N/m and 300 kHz respectively were used to image the samples. In order to minimize the interaction force between the tip and the substrate (but without losing contact) “light tapping” was used by keeping the set-point amplitude ratio  $r_{\text{sp}} = A_{\text{sp}}/A_0$  close to 1 (where  $A_0$  and  $A_{\text{sp}}$  are the free oscillation amplitude and the reduced scanning set-point amplitude of the cantilever,

respectively). Images were processed and the layer heights as well as the surface roughness were measured using the software Scanning Probe Image Processor (SPIP, Image Metrology, Hørsholm, Denmark).

#### **4.3.4 Transmission Electron Microscopy**

The F8BT:TFB ultrathin layers were lifted off from mica substrates by gently immersion into a de-ionized water bath and then placed on a 200 square mesh copper grid. The specimens were analysed in a FEI Tecnai T20 tunnelling electron microscope (TEM) EM (FEI, Oregon, United States of America), operated at 200 kV and equipped with an Olympus-SIS Megaview III CCD camera (Olympus Soft Imaging Solutions GmbH, Münster, Germany). We used an objective aperture of 20  $\mu\text{m}$  and defocus value of approximately 10  $\mu\text{m}$ . The software used to process the TEM images is the Micrograph<sup>™</sup> (Gatan, Abingdon, UK).

#### **4.4 Results**

In what follows we present the resulting phase-separated nanodomains from different concentrations of the F8BT:TFB polymer blend in *p*-xylene solutions (20 mg/ml and 14 mg/ml) spin cast on mica. For the polymer blend with 20 mg/ml concentration, we considered the effect of the spin-coating parameters (2,000 – 5,000 rpm), the heat treatment (annealing) and the F8BT:TFB polymer blend ratio (1:1, 1:4 and 4:1 by weight) on the morphological behaviour of the thin films. For the polymer blend with 14 mg/ml concentration, we present the differences in the ultimate morphology of the thin films resulting from a larger variation F8BT:TFB blend ratios (1:1, 1:2, 1:3, 1:4, 2:1, 4:1, 1:0 and 0:1 by weight) for a specific spin-coating speed of 4,000 rpm.

#### 4.4.1 F8BT:TFB Polymer Blends with concentration 20 mg/ml

##### 4.4.1.1 F8BT:TFB Polymer Thin Films with 1:1 blend ratio

Figures 4.7a, b, c and d show typical AFM height images of the F8BT:TFB polymer blend films (1:1 by weight ratio) from *p*-xylene solutions (concentration 20 mg/ml) spin cast on mica. The topography of the thin-film spin-coated at 2,000 rpm is characterised by the formation of wells, in which their diameter is in the sub-micrometre scale (black areas in Figure 4.7a) in a higher-level layer (light yellow area in Figure 4.7a). The same morphological behaviour was observed when thin films were prepared by spin coating F8BT:TFB polymer droplets at 4,000 rpm (Figure 4.7b) and at 5,000 rpm (Figure 4.7c); however, the wells exhibit a slight decrease in their lateral size, increasing the spin coating rate. Furthermore, a thin film spin coated at 2,000 rpm, was then annealed at 200 °C, for 12 hours. In this case, as shown in Figure 4.7d, the morphology and the texture of the surface has changed drastically and the well-defined domains are absent. The well-morphology (prior to annealing) is very similar to the one observed by Kim *et al.* [7] albeit at much smaller scale (as our molecular weights are smaller) who have associated the wells with a low enclosed phase imbedded in a high matrix phase.



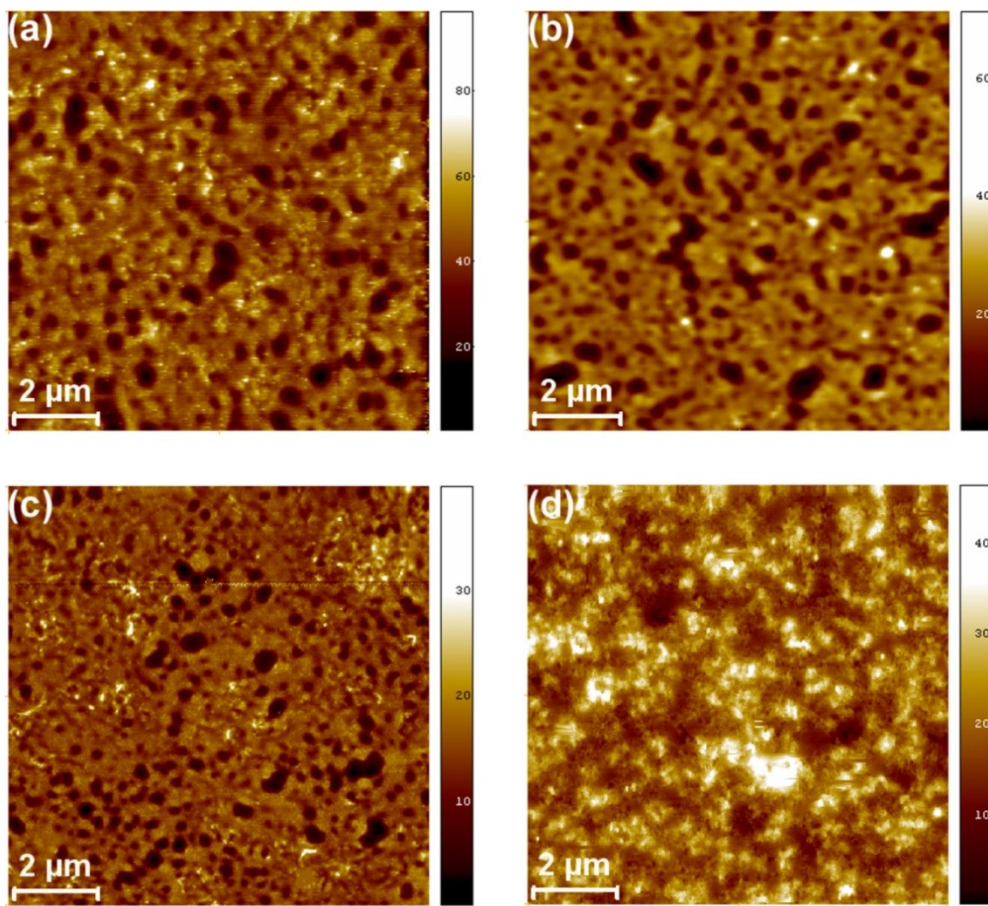


**Figure 4.7** Tapping mode AFM images,  $10 \times 10 \mu\text{m}^2$ , of F8BT:TFB (1:1 by weight ratio) thin-films on mica spin coated (concentration 20 mg/ml) at (a) 2,000, (b) 4,000, (c) 5,000 rpm for 90 seconds; (d) annealed film of the case (a) at 200 °C, for 12 hours (colour scales are in nanometers).

Figure 4.8 presents AFM zoomed images of the F8BT:TFB, 1:1 by weight blend ratio thin films with different spin coating speeds, highlighting the well structures (Figures 4.8a, c, e), along with height profiles taken across the zoomed images (Figures 4.8b, d, f). We observe that the height between the matrix layer and the lower lying domains (depth of the wells) lowers as we increase the spin coating speed. In the case of spin coating at 2,000 rpm the height is  $\approx 26$  nm (Figure 4.8b), while in the case of spin coating at 4,000 and 5,000 rpm the height decreases to  $\approx 21$

nm (Figure 4.8d) and  $\approx 13$  nm (Figure 4.8f), respectively. Several wells from different images have been considered and the graph of Figure 4.9 shows the relation between the well average depth and the spin-coating speed.

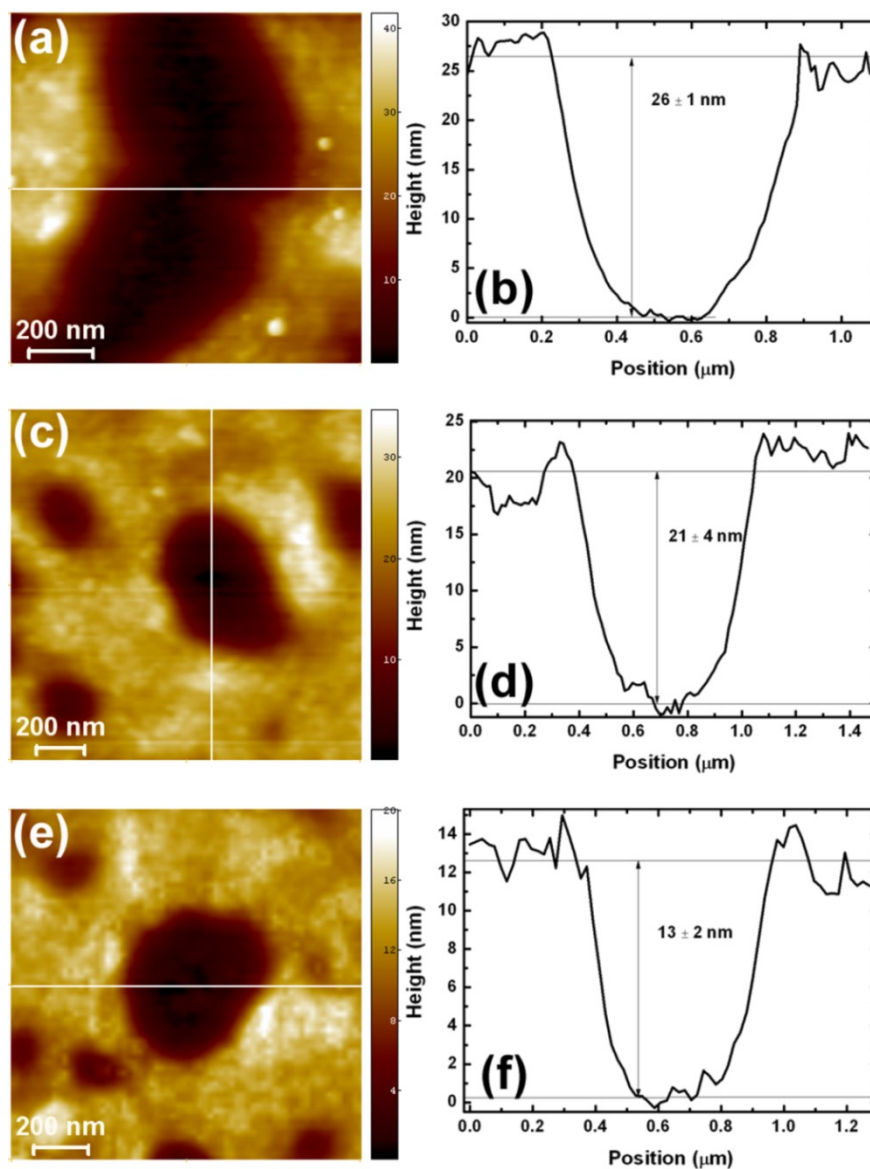


Figure 4.8 (a) (c) (e) AFM height images (the scan size is for a:  $1.1 \times 1.1 \mu\text{m}^2$ , for c:  $1.5 \times 1.5 \mu\text{m}^2$  and for e:  $1.3 \times 1.3 \mu\text{m}^2$ ) focused on a representative well structure formed from F8BT:TFB films (concentration: 20 mg/ml) with 1:1 by weight blend ratio spin coated at 2,000, 4,000 and 5,000 respectively. (b) (d) (f) Height profiles from the corresponding AFM images, taken across the well structures.

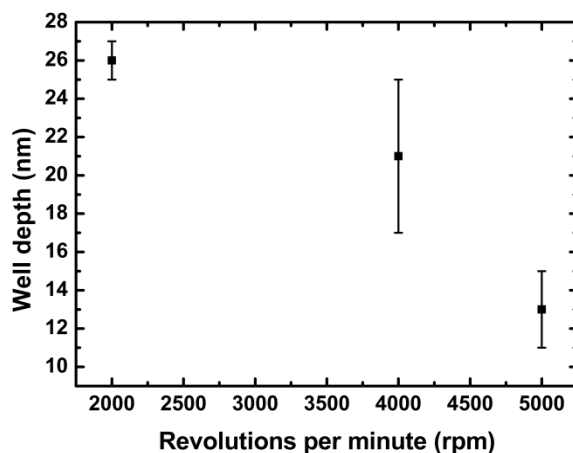


Figure 4.9 Well depth against the spin-coating speed applied to prepare F8BT:TFB blend thin films (concentration: 20 mg/ml) with 1:1 by weight blend ratio.

#### 4.4.1.2 F8BT:TFB Polymer Blend thin films with 1:4 weight ratio

Figure 4.10a and c shows the structural behaviour of the F8BT:TFB films with blend ratio 1:4, spin coated at 4,000 rpm (Figure 4.10a) and at 5,000 rpm (Figure 4.10c). In both cases the polymer blend has phase-separated into several island-like structures surrounded by a lower-level matrix. This is the opposite case to that presented in 4.4.1.1 section and Figures 4.7 and 4.8. According to height profiles taken across the images of Figures 4.10a and c, the average height of the islands was 14 nm and 9 nm, accordingly (Figures 4.10b and d).

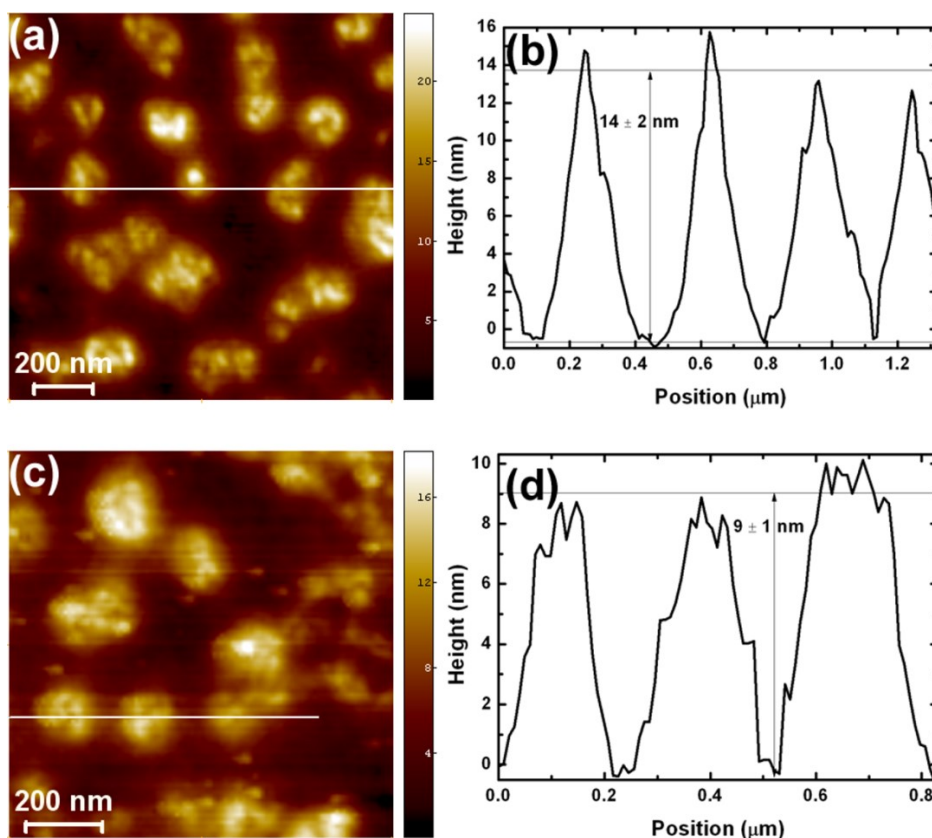
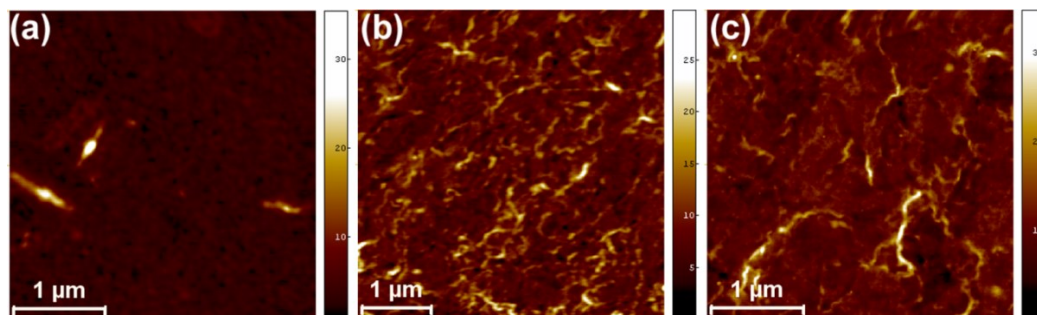


Figure 4.10 (a) (c) Typical AFM height images (scan size for a:  $1.3 \times 1.3 \mu\text{m}^2$  and for c:  $1.1 \times 1.1 \mu\text{m}^2$ ) of F8BT:TFB polymer blends films with 1:4 by weight ratio (concentration 20 mg/ml). Spin coated at 4,000 rpm and 5,000 rpm respectively; (b) (d) height profiles of the corresponding AFM images, highlighting the height of the island structures.

#### 4.4.1.3 F8BT:TFB Polymer Blend thin films with 4:1 weight ratio

Figure 4.11 presents AFM height images of F8BT:TFB thin films with blend ratio 4:1 spin coated at 2,000 rpm (Figure 4.11a), 4,000 rpm (Figure 4.11b) and 5,000 rpm (Figure 4.11c). The morphology of the films is characterised by several ridges and well-like domains which become less frequent by increasing the spin coating speed. In addition, the roughness of the thin-films increases with the spin coating speed; the root mean square (RMS) for the 2,000 rpm, 4,000 rpm and 5,000

rpm thin films is  $4 \pm 1$  nm,  $8 \pm 1.2$  nm and  $11 \pm 1.8$  nm respectively. The roughness was determined from AFM images with scan size  $\sim 4 \times 4 \mu\text{m}^2$ .



**Figure 4.11 (a) (b) (c) Representative AFM height images of F8BT:TFB polymer blends films with 4:1 by weight ratio, from concentration 20 mg/ml and spin coated at 2,000, 4,000 and 5,000 rpm respectively (scan size for a:  $3.4 \times 3.4 \mu\text{m}^2$ , b:  $4.4 \times 4.4 \mu\text{m}^2$  and for c:  $3.4 \times 3.4 \mu\text{m}^2$ ). The height scale unit is nm.**

#### **4.4.2 F8BT:TFB Polymer Blend thin films from concentration 14 mg/ml**

The morphology of F8BT:TFB thin films in various blend ratios, from solutions with 14 mg/ml, spin coated at 4,000 rpm was also investigated.

##### **4.4.2.1 F8BT:TFB Polymer thin films with 1:1 by weight ratio**

Figure 4.12a presents the phase-separated structures in the F8BT:TFB thin film with 1:1 blend ratio. The morphology of the film does not differ with the morphology of the corresponding thin film with concentration 20 mg/ml (Figure 4.7b). Following the structural trend of the higher concentration annealed thin films, the annealed sample of the F8BT:TFB, with 1:1 blend ratio at 14 mg/ml concentration, as presented in Figure 4.12b does not obtain a clear well morphology.



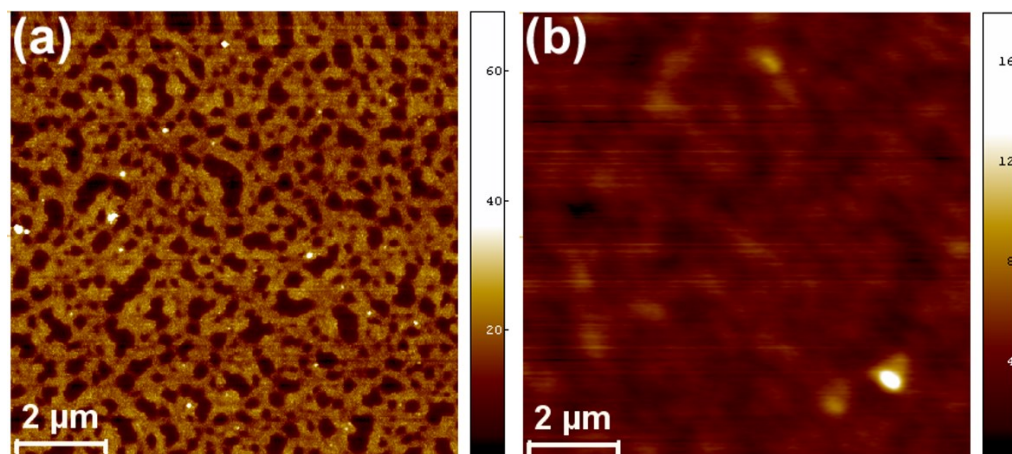


**Figure 4.12** Typical AFM height images of the F8BT:TFB polymer thin films with 1:1 blend ratio (14 mg/ml), spin coated at 4,000 rpm for 90 seconds (a) as cast and (b) annealed at 200 °C for 12 hours (scan size for a and b:  $10 \times 10 \mu\text{m}^2$ , z-scale in nm).

Furthermore, to investigate the phase-separated domains in thin-films of F8BT:TFB, we used the transmission electron microscopy technique (TEM). The TEM image of Figure 4.13a revealed the clear formation of the phase-separated domains. The dark-brown well-like domains observed in AFM height images (Figure 4.13b) are presented in TEM with bright grey colour and the light yellow in AFM matrix which surrounds the wells is presented in TEM with a dark grey colour. The difference in TEM contrast originates from the difference in the electron waves scattered through the thin film. From comparing the TEM and AFM images, we observe that the sizes of the domains seen in both images do agree. The TEM contrast is due to the difference in thickness but could also be enhanced by the difference in the content of heavy atoms (F8TB contains the heavier atoms) indicating that this is the main constituent of the thickest domains (matrix/continuous phase) which is consistent with the results of Yim *et al.* [3] (see also Figure 4.5). The F8BT:TFB 1:1 film presented in Figure 4.12a is further processed using SPIP to

remove some small artefacts (bright spots on film surface) caused probably from dust and presented in Figure 4.13b. Height profile of the image in Figure 4.13b, presented in Figure 4.13c reveals that the depth of the wells is  $\approx 16$  nm, lower than the corresponding depth of the 20 mg/ml thin film (Figure 4.8c).

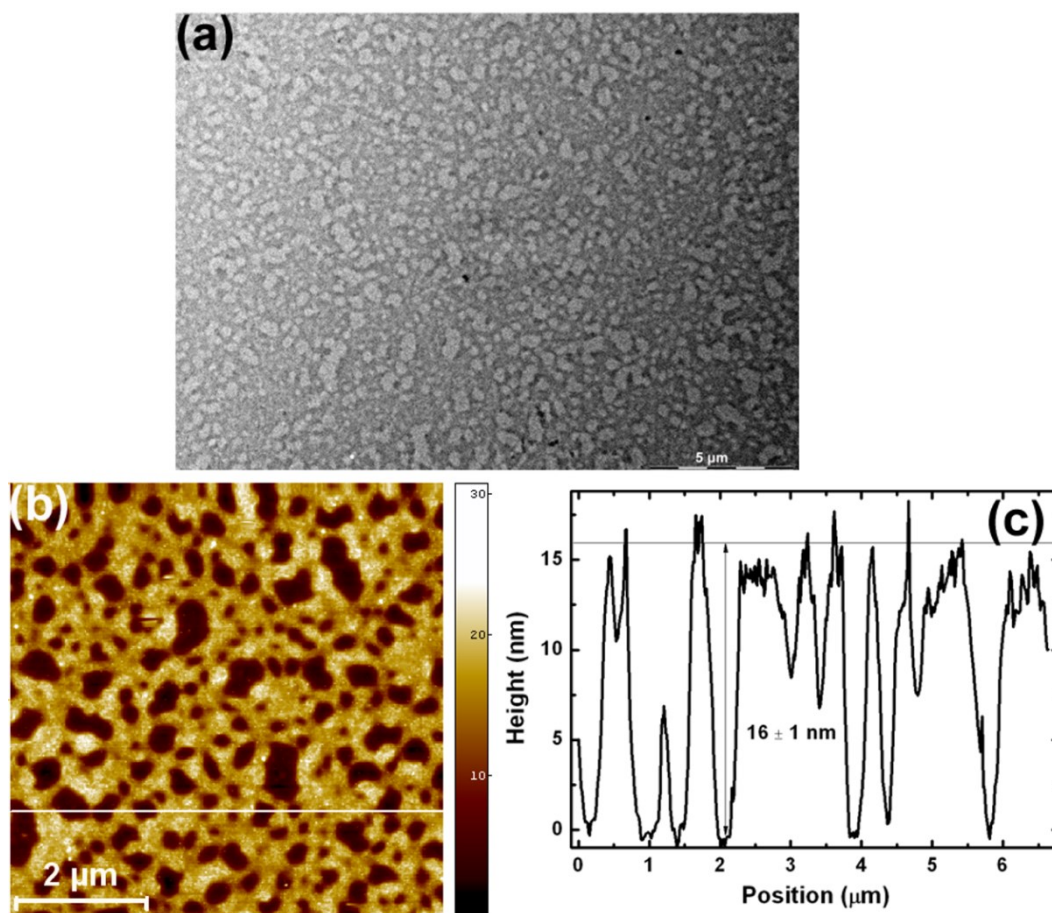
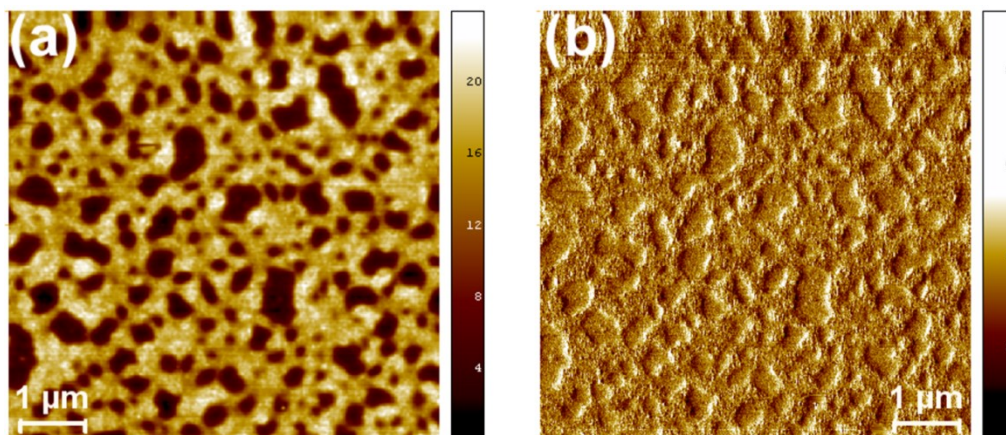


Figure 4.13 (a) TEM image of the F8BT:TFB polymer thin film with 1:1 blend ratio, spin coated at 4,000 rpm for 90 seconds. (b) AFM height image of the same thin film (scan size is:  $6 \times 6 \mu\text{m}^2$ ); (c) height profile corresponding to the white line of image (b).

Finally, Figure 4.14 presents an AFM phase image (Figure 4.14b) and the corresponding height image (Figure 4.14a) taken from the F8BT:TFB 1:1 thin film. The phase separation into two phases is evident in both the topography and the phase

images, but interestingly, the high-lying domains look ‘grainy’ indicating some intermixing at the free interface as will be discussed in detail later (section 4.5).



**Figure 4.14** AFM height (a) and the corresponding phase (b) images ( $7 \times 7 \mu\text{m}^2$ ) of F8BT:TFB thin film with 1:1 blend ratio (14 mg/ml solution concentration), spin coated at 4,000 rpm for 90 seconds ( $z$ -scale in (a) nm and (b) degrees).

#### **4.4.2.2 F8BT:TFB Polymer Blend Thin Films with 1:2, 1:3 and 1:4 by weight ratio**

Thin films of conjugated F8BT:TFB polymer blends with 1:2, 1:3 and 1:4 blend ratios from 14 mg/ml concentration solutions were also prepared. The big scan-size ( $\approx 20 \times 20 \mu\text{m}^2$ ) AFM height images of Figure 4.15 present the typical topography of the thin film with blend ratio 1:2 (Figure 4.15a), 1:3 (Figure 4.15d) and 1:4 (Figure 4.15g). Island-like domains were formed on the film surface surrounded by a lower-lying matrix (continuous phase). As shown in the smaller scan size AFM images of Figure 4.15b, e and h, the islands are oblong and/or multi-shaped in the case of the 1:2 blend and as the fraction of the F8BT part decreases the islands become smaller and more rounded. Furthermore line-scan profiles of Figure



4.15c, f and i, which corresponds to the white lines of the AFM height images, show that the height of the islands decreases with the decrease of the F8BT part.

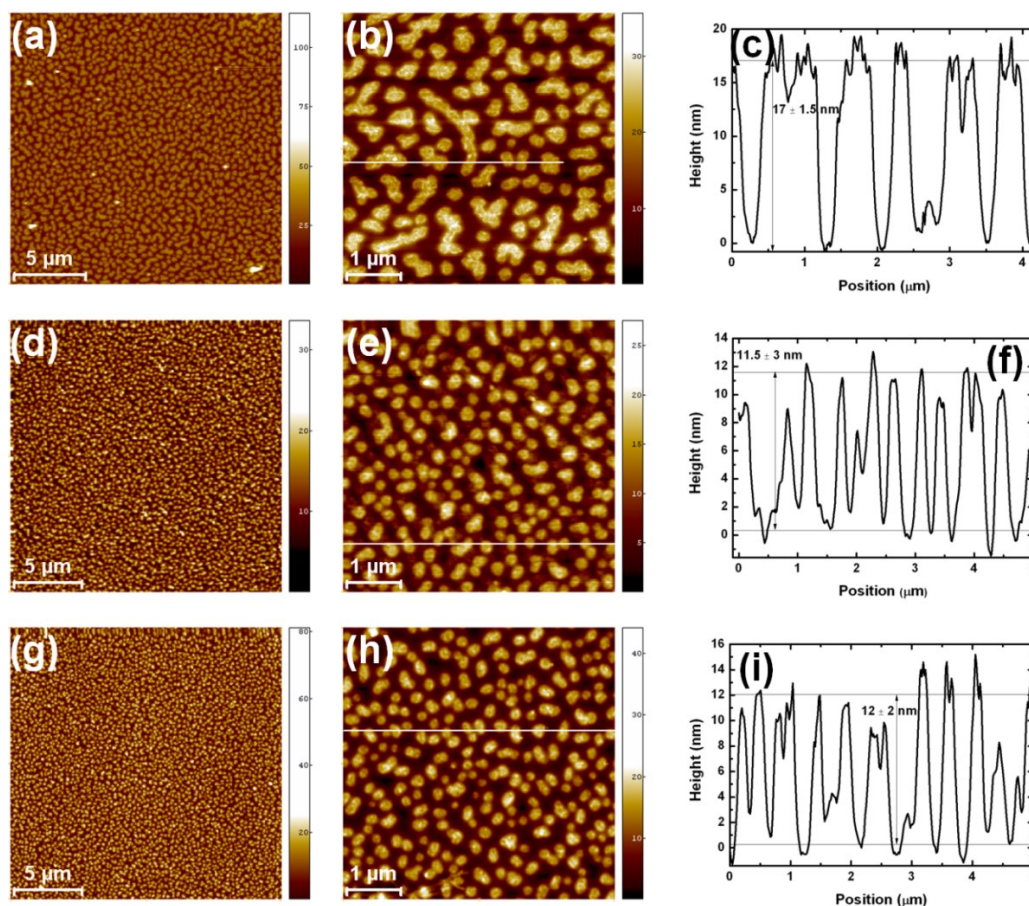


**Figure 4.15** (a) (d) (g) Typical AFM height images of the F8BT:TFB thin films with 1:2 (a), 1:3 (d) and 1:4 (g) blend ratio spin coated at 4,000 rpm (the scan sizes are  $\approx 20 \times 20 \mu\text{m}^2$ ); (b) (e) (h) Zoomed areas of the corresponding images (a) (d) and (g) (the scan size is:  $5 \times 5 \mu\text{m}^2$ ); (c) (f) (i) Height profiles taken across the corresponding zoomed images (white lines).

Figure 4.16a presents a TEM image of the F8BT:TFB 1:4 thin film. The phase-separation of the blends into rounded islands surrounded by a continuous phase of different phase is clear also by using TEM. However, this time the contrast is much reduced (see Figure 4.13a) presumably by the fact that the higher lying (mass heavier) F8BT-rich islands are less pure and further contaminated by the (mass

lighter) TFB (which now exists at a much higher percentage) leading to reduced contrast. The AFM phase imaging of Figure 4.16c which corresponds to the AFM height image of Figure 4.16b, reveals that the surface of the phase-separated domains in this case (F8BT:TFB 1:4) are not pure domains of one polymer or the other. This will be discussed later in the discussion section.

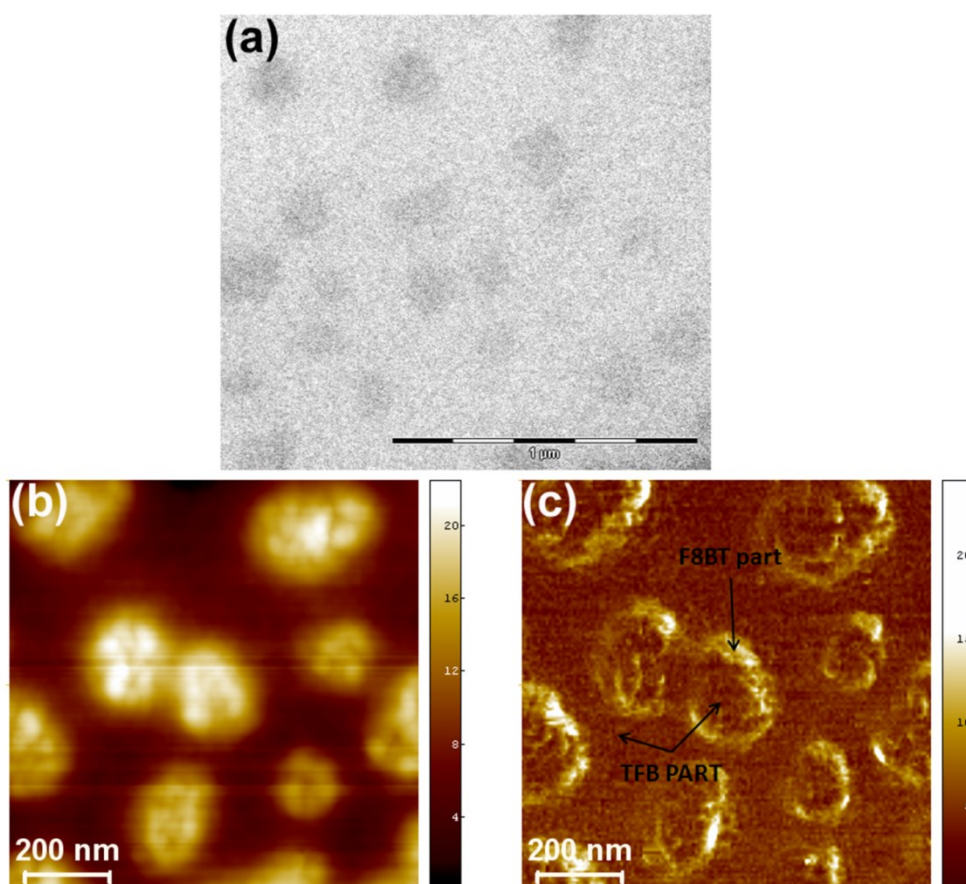


**Figure 4.16.** (a) TEM image of F8BT:TFB thin film with 1:4 by weight polymer blend ratio from 14 mg/ml concentration solutions spin coated at 4,000 rpm for 90 seconds. (b) AFM height image ( $1 \times 1 \mu\text{m}^2$ , colour scale/z-scale: nanometres) of the same thin film along the corresponding (c) AFM phase imaging (z-scale: 24 degrees).

Furthermore, a study of the rounded higher lying domains was also performed. Figure 4.17 presents  $1 \times 1 \mu\text{m}^2$  scan-size AFM images highlighting the islands

formed in F8BT:TFB blend films with 1:2 (Figure 4.17a), 1:3 (Figure 4.17b) and 1:4 (Figure 4.17c) blend ratio. The coverage of the islands in the total surface, the number of islands per  $\mu\text{m}^2$ , the diameter of the islands and the mean height difference from the lower lying matrix to the higher islands domains were studied. The red lines surrounded the islands of Figure 4.16 correspond to the limits of the studied structures. The red lines were chosen to be placed in areas where the step between the flat surface and the polymer domain is rapidly increasing to height values higher than 5 nm to exclude any steps caused by noise.

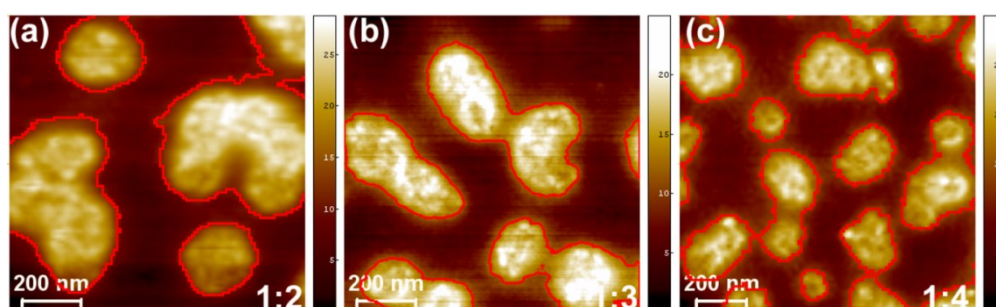


**Figure 4.17.** (a) (b) (c) AFM height images of F8BT:TFB thin film with (a) 1:2, (b) 1:3, (c) 1:4 by weight polymer blend ratio (scan size of the images are:  $1 \times 1 \mu\text{m}^2$ ), from 14 mg/ml concentration solutions spin coated at 4,000 rpm for 90 seconds; The red lines correspond to distinguish the borders of the polymeric islands.

Plots of Figure 4.18 present the coverage of the islands (Figure 4.18a), the number of islands per  $\mu\text{m}^2$  (Figure 4.18b), the mean diameter of the islands (Figure 4.18c) and the mean average height of the islands against the blend ratio of the F8BT:TFB thin films (Figure 4.18d). We observe that the coverage, the diameter and the height of the islands decreased with the decrease of the F8BT part in the blend. The opposite trend is obtained with the number of islands per square micrometre: the number of islands increased with decreasing the fraction of the F8BT part.

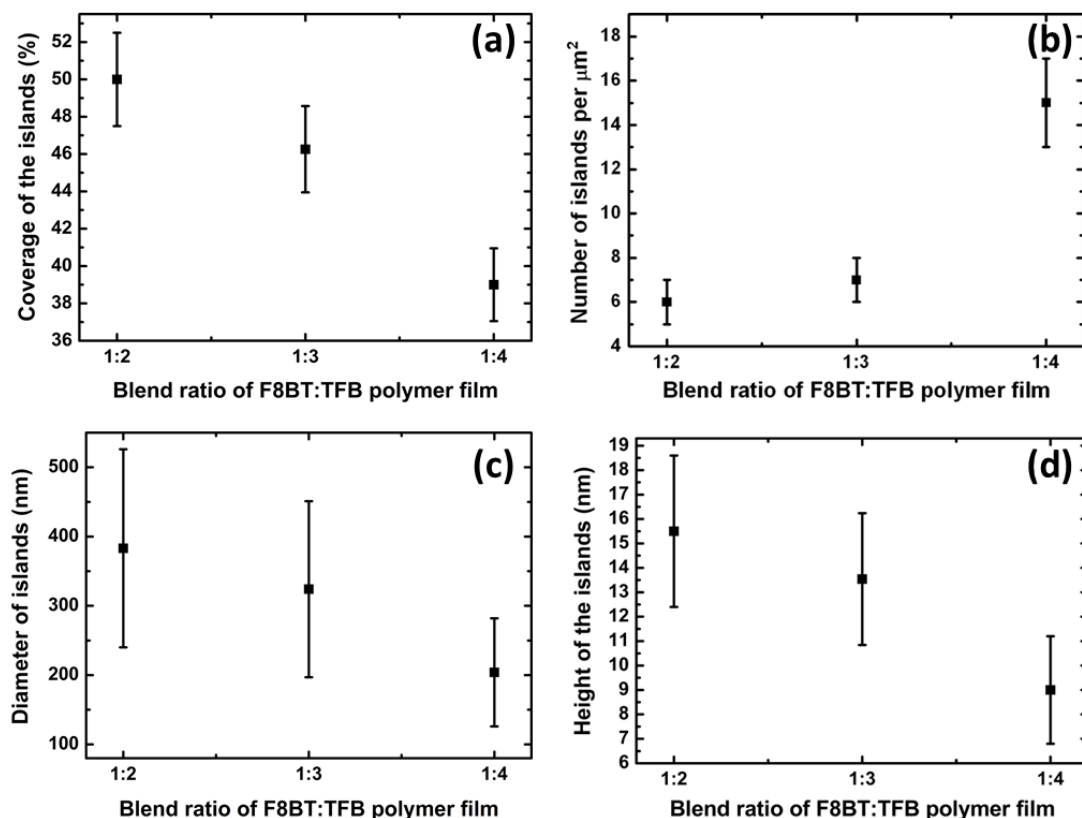


Figure 4.18. (a) Coverage of the islands, (b) the number of the islands, (c) the diameter of the islands and (d) the height of the islands formed in the F8BT:TFB thin films versus the by weight F8BT:TFB polymer blend ratio.

#### 4.4.2.3 F8BT:TFB Polymer Blend thin films with 0:1, 1:0, 2:1 and 4:1 by weight blend ratio

The Figure 4.19 presents AFM height images of the F8BT:TFB thin films with 0:1 (Figure 4.19a), 1:0 (Figure 4.19b), 2:1 (Figure 4.19c) and 4:1 (Figure 4.19d) blend ratio. The homopolymer TFB, formed a quite flat, uniform layer on the film surface, including several holes. Post-processing AFM analysis (shown in Figure B1 of Appendix B) revealed that these holes are the “footprint” of the pyramid end of the cantilever’s tip. The flat layer appears to be relatively soft, as the tip of the AFM’s cantilever penetrated its surface forming small holes, even with imaging with



soft tapping (set-point amplitude ratio close to 1). This might be attributed to the residual solvent, which may have been trapped in the film. The homopolymer F8BT formed a relatively uniform layer with some irregular islands on top, which compares well with the literature on F8BT homopolymer thin films [1]. The thin films with 2:1 and 4:1 blend ratio formed were similar but with several well-like stripes and some irregular islands formed at the top surface.

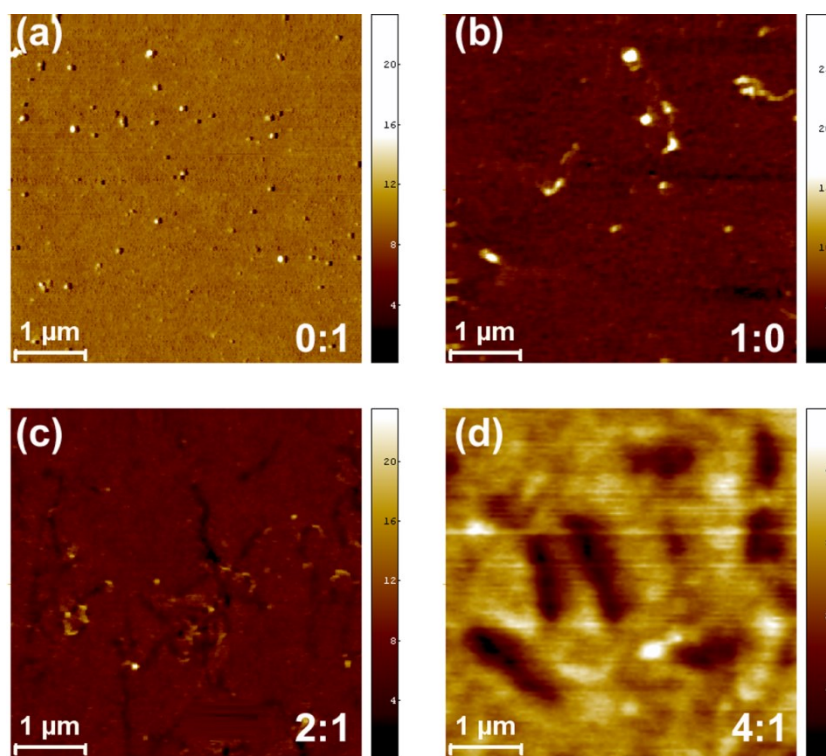


**Figure 4.19** AFM height images of (a) TFB homopolymer, (b) F8BT homopolymer, (c) F8BT:TFB polymer blend with 2:1 polymer blend ratio and (d) F8BT:TFB polymer blend with 4:1 polymer blend ratio thin films, made from solutions with concentration 14 mg/ml and spin coated at 4,000 rpm for 90 seconds.

## 4.5 Discussion

We presented AFM and TEM images of phase-separated domains in conjugated F8BT:TFB thin films with various blend ratios and spin coating parameters, from two different concentrations (20 mg/ml and 14 mg/ml) in *p*-xylene. As the F8BT:TFB blend ratio is varied, the surface morphology is altered. Two main morphological trends were observed; one for the F8BT:TFB 1:1 by weight ratio thin films and one for the F8BT:TFB with 1:2, 1:3 and 1:4 by weight ratios. For the 2:1 and 4:1 polymer blend films, no clear morphology was seen.

In the particular case of F8BT:TFB thin films with 1:1, the phase-separated morphology consists of well-like sub-micrometre lateral size domains  $\sim 0.4 \pm 0.2 \mu\text{m}$  (dark areas in AFM height images of Figures 4.7, 4.8 and 4.12-4.14) in a continuous phase (bright areas in AFM height images of Figures 4.7, 4.8 and 4.12-4.14). Similar phase separated domains in F8BT:TFB 1:1 thin films were previously observed by other groups [1,3,7], but with *micrometre* phase-separation. Kim *et al.*, who have analysed the lateral phase compositions of the F8BT:TFB 1:1, using optical microscopy under blue excitation (which results in green luminescence of the F8BT) and micro-Raman spectroscopy, reported that the brighter domains are F8BT-rich, while the darker well-like domains ( $\sim 2 - 5 \mu\text{m}$ ) are TFB-rich [7]. It is important to point out, that we have performed optical fluorescence microscopy under the same conditions as Kim *et al.* used, but we have not observed any domains, due to their significantly smaller size (no fluorescence results are included in this present study). The formation of the well domains within the continuous phase is formed due to the spinodal decomposition mechanism (by which a solution of two different polymers

with different solubility, chemical and physical properties, separate into distinct phases due to local density fluctuations which are amplified), in line with the F8BT:TFB phase diagram (see Figure 4.3, middle (50:50) compositions) [7], as well as in line with conventional polymers, such as the blend of the deuterated poly(methyl methacrylate) (dPMMA) and the poly(styrene-ran-acrylonitrile) (SAN) [34].

Increasing the TFB weight ratio in the blend to produce F8BT:TFB polymer blends with weight ratio 1:2, 1:3, 1:4, led the morphology to change drastically compared to the morphology of 1:1 thin films. Isolated island-like sub-micrometre size domains  $\sim 0.1 - 0.5 \mu\text{m}$  surrounded by a matrix were formed (Figures 4.10 and 4.15-4.18), triggered by the process of the nucleation and growth mechanism in line to the phase diagram of this blend system (see Figure 4.3) and Kim *et al.* study [7]. The reason for this change in morphology (compared to the 1:1 film) is the presence of the more abundant TFB polymer. According to previous studies on the F8BT:TFB 1:3 lateral domains [7], the continuous layer is TFB-rich, while the islands are F8BT-rich. In contrast to our findings; the lateral size of the domains observed in ref. [7] is significantly higher, varying from 0.5 to 1.0  $\mu\text{m}$ .

The reason behind this difference (domains with lateral size significantly lower than the size of the domains reported in the literature) in both cases (F8BT:TFB 1:1 and 1:2, 1:3, 1:4), lies on the coupling between the much lower molecular weight of the polymer blends we used (see Table 4.1), compared with Kim *et al.* [7] ( $M_n = 108 \text{ kg/mol}$  and  $M_n = 56 \text{ kg/mol}$  for F8BT and TFB, respectively) and the fact that we

used polymers with similar  $M_n$ . It has been reported by Yim *et al.* that the size of the phase-separated domains is highly affected by the molecular weight of *each* polymer in the blend [3]. Performing studies on the morphology of F8BT:TFB thin films of different molecular weights, they stated that increasing the  $M_n$ , the domain sizes increase accordingly. The size of the lateral phase-separated domains is also affected by a complex coupling between the relative miscibility and viscosity of the homopolymers in the blend, as well as chain mobility varying during a rapid solvent evaporation. Thus, different molecular weight combinations of the two polymer parts of the blend can result in different blend phase-separated morphologies. Although Yim *et al.* [3] have investigated several molecular weights, both high and low, in all cases where lateral phase separation did not happen (or at least was not measurable) there was a relatively large difference between the molecular weights of F8BT and TFB (see Figure 4.5). To the best of our knowledge we are the first who have observed and investigated the phase separated domains in the sub-micrometre scale for this system and we associate this type of phase separation to the use of *similar and low* molecular weight polymers in the blend. The low molecular weights promote small domains (sub-micrometre) and the similar molecular weight introduces antagonistic factors to inhibit the dominance of a purely vertical phase separation (as observed by Yim *et al.* for his low molecular weight pairs which were of significantly different molecular weight, see Figure 4.5a). This finding is of great importance as both the use of low molecular weight polymers and sub-micrometre phase separation could result in the development of improved semiconducting devices [3].



The distribution of the phases (consisted of lower lying and higher lying domains) formed in 1:1 and 1:4 films was also quantitatively analysed by post-AFM image processing and is presented in the graph of Figure 4.20. The depth distribution (per cent) confirms the existence of two main phases. The lower lying domains in the 1:1 polymer films were significantly fewer than the lower-lying domains in films with 1:4 blend ratio. Furthermore, the percentage of the coverage of the higher domains as observed from the top of the films was also investigated and found ~ 46% for 1:4 films and ~ 68% for 1:1 films. Comparing this last value with Kim and *co-workers* study [7], we observe that our case of the 1:1 thin film (of low and similar molecular weights) resembles the 3:1 thin film from the Kim *et al.* study (higher and dissimilar molecular weights), which is the only case that Kim and *co-workers* have reported submicrometre lateral phase separation. In contrast to Kim *et al.* our F8BT:TFB films with 2:1 and 4:1 gave no clear morphology (Figures 4.11, 4.19c and d). These results signify the importance of the molecular weight values for the resulting phase separation; the influence can be complex and unexpected as many factors change with the molecular weight of the two polymers.

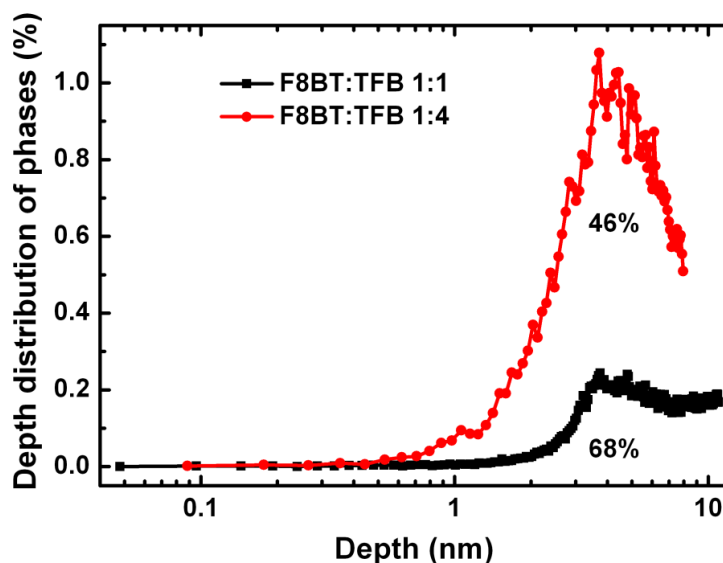


**Figure 4.20** Depth distribution of the lower-lying phases as calculated from AFM image analysis processor for 1:1 blend ratio (black rectangular) and for 1:4 blend ratio (red circle); the percentage of the corresponding higher phase is also presented.

In both morphological trends (F8BT:TFB 1:1 and 1:2, 1:3, 1:4), the phases are not pure with one polymer. As already mentioned above, there are F8BT-rich and TFB-rich phases. This, has been identified by Kim and *co-workers*, who performed extensive micro-Raman spectroscopy techniques to further (quantitatively) examine the two different phases in 1:1 F8BT:TFB thin films [7]. They found that the F8BT-rich phase consists of  $\sim 65 - 70\%$  F8BT and  $30 - 35\%$  TFB and that the TFB-rich phase consists of  $\sim 75 - 80\%$  TFB and  $20 - 25\%$  T8BT. They stated that this phenomenon originates from the fact that the lower molecular weight polymer in the blend system has the tendency to obtain purer phases, unlike the higher molecular weight polymer, which results in higher intermixing with the lower molecular weight polymer. In our case, although we have used low molecular weight polymers in the blend, the molecular weight is very similar (the *molecular weight* fraction of our system is close to 1). The TEM images of F8BT:TFB thin films with 1:1 (Figure

4.13a) and 1:4 (Figure 4.16a) blend ratio, show that the contrast between the phase separated domains is higher in the case of the 1:1 thin film. Noting that the TEM contrast could originate from the difference in the content of heavy atoms (F8TB contains the heavier atoms); the clear contrast between the higher-lying and the lower-lying domains enhances the argument of the purer phases (F8BT phase on top and TFB phase below) when the molecular weights of the polymers are relatively low. However, when we increased the volume fraction of one of the polymers in the blend (F8BT:TFB 1:4) the TEM contrast was lower, which is an indication of less purity in the domains. Thus, we assume that the weight ratio of each polymer blend could affect the purity of the phases.

AFM phase imaging can reveal the fine details of the phase separation at the free interface (which can be different to the phase separated domains in the bulk of the film). The AFM phase image of F8BT:TFB 1:1 thin film shown in Figure 4.14b which is a large scan size, revealed some phase contrast between the lower-lying and the higher-lying phase separated domains but interestingly the higher-lying domains look 'grainy' indicating intermixing of the capping layer. Furthermore, the AFM phase imaging in thin films of F8BT:TFB with 1:4 weight ratio shown in Figure 4.16 exhibited a clear contrast between the periphery of the tall F8BT-rich domains and the rest of surface and a several small size 'dark' domains within the islands. These observations constitute first a direct proof of the TFB capping layer inside the islands as speculated by Kim *et al.* [7] using Raman spectroscopy which led to the model shown schematically in Figure 4.4 and second indicate a 'grainy' structure of this capping layer signifying that it is not a wetting layer. Our technique is much more

surface specific and beyond verifying the model reveals more information regarding the organisation of the surface layer (including the capping layer). The arrows in phase imaging in Figure 4.16c indicate the fine details of both the TFB capping layer and the TFB layer surrounding the island-like domains. It is clear that we do not have the formation of a wetting TFB layer but the formation of nanoscale-sized discontinuous TFB domains as indicated by Kim *et al.* measurements and thus speculated but never directly imaged. We present for the first time in high resolution imaging, the phase behaviour of the polymer blend in the nano-scale at the free interface.

The phase separation, fine structure and purity of the domains in the nano-scale are of paramount importance for the fabrication of efficient LEDs and solar cells [23,35].

#### **4.5.1 Thin film nano-phase separation: effect of spin coating, annealing and concentration parameters**

Apart from the analysis of the two different nano phase-separated morphologies in thin films of F8BT:TFB with 1:1 and 1:2, 1:3 and 1:4 blend ratios, the effect of the spin-coating parameters on the ultimate phase-separated domains in F8BT:TFB with 1:1 and 1:4 weight ratio thin films is also investigated in the nano-scale. As observed in Figures 4.7, 4.8 and 4.10 the lateral structures change only slightly by varying the spin coating rate (few nanometres in the  $\sim 50 - 500$  nm diameter). However the height difference between the lower lying and the higher domains is shifted by several nanometres (which is a significant percentage to the height differences typically in the range of 10 to 25 nm). As shown in the height

profiles of Figures 4.8b, d, f and Figures 4.10b, d, which correspond to the white lines of the AFM height images and the collective graph of Figure 4.9, the height difference between the phases decreases by increasing the spin rate by  $\sim 2 - 10$  nm. This change in the height difference could be a valuable control parameter for the device processing and performance. The present study is the first presenting this structural trend. It is well-known that increasing the spinning rate, thinner films are formed. This reduction in the thickness reflects also on the thickness of the TFB-rich and F8BT-rich domains.

Furthermore, another factor which affects the height-step between the phases is the solution concentration. For example in the case of F8BT:TFB thin films with 1:1 blend ratio, spin coated at 4,000 rpm, from 20 mg/ml and 14 mg/ml solutions the step was  $\sim 21$  and  $\sim 16$  nm respectively. We attribute this to the thicker layers caused by the higher density of molecules, which leads to higher stretching of the polymers, similar behaviour with that of polymer brushes [36].

Finally, heat treatment was also applied to some F8BT:TFB blend thin films to investigate how this process would affect the stability of the phase-separated domains. Figure 4.7d, shows a representative AFM image from F8BT:TFB thin films with 1:1 blend ratio, annealed at 200 °C for 12 hours. Compared with the 1:1 films with no heat treatment, the heated film exhibited no lateral phase-separated domains and the typical 1:1 morphology has been lost. This is a key point as we have to consider that the well-formed phase-separated domains are unable to withstand this heat treatment, which is expected to be detrimental for the performance of the future devices, if these are going to be used in high temperature environment.

#### 4.5.2 Lateral Size Transition of the Phases from F8BT:TFB with 1:2 to 1:4 by weight blend ratio

Figure 4.15 presents typical AFM images (large scan size:  $20 \times 20 \mu\text{m}^2$  and small scan size:  $5 \times 5 \mu\text{m}^2$ ) and the corresponding height profiles of F8BT:TFB thin films with blend ratios varying from 1:2 to 1:4. Interesting nanometre-length scale differences was observed in the phase-separated domains, which is possible to affect the functionality of the thin films applied in devices. A closer look at the small scan size images (Figures 4.15b, e, h), reveals that the higher lying phase (F8BT-rich), becomes more rounded and from the corresponding height profiles (Figures 4.15c, f, i), we observe that from 1:2 blend ratio to 1:3 and 1:4, the step between the lower and the higher lying domains decreases. A reason behind this transition might be the lower weight fraction of the F8BT polymer in the blend which results in smaller island-like domains as the TFB-rich continuous layer increases.

Furthermore, quantitative analysis of the island-like domains (Figure 4.17), from  $1 \times 1 \mu\text{m}^2$  scan size AFM images of F8BT:TFB 1:2, 1:3 and 1:4 showed in detail the change in morphology of the island-like domains. Post-processed data from the AFM, revealed that the coverage of F8BT-rich polymer islands decreases almost linearly with the increase of the weight fraction of TFB in the F8BT:TFB thin-films ( $\sim 50\%$ ,  $\sim 45\%$   $\sim 39\%$  for 1:2, 1:3 and 1:4 respectively, Figure 4.18a). Although the island's coverage decreases, the number of islands per square micrometre increases by increasing the TFB part (Figure 4.18b). This reveals that more F8BT-rich (electron transporting) domains can form in (laterally) very small areas. More islands per square micrometre and lower surface coverage, unavoidably results in the

formation of islands with smaller diameter ( $\sim 370$  nm,  $\sim 300$  nm and  $\sim 190$  nm for 1:2, 1:3 and 1:4 respectively, Figure 4.18c). Finally, we can deduce that the size in vertical direction of the islands by increasing the TFB part is also affected. It was found that the height decreased by few nanometres (Figure 4.18d), which can be crucial for the overall performance of the thin-film devices. Note that the calculated by line-scan profile heights reveal somewhat higher island domains compared with the calculations of Figure 4.18d. This difference is related with the peak-to-peak average measurement of the island heights obtained from post-processing AFM particle analysis (Figure 4.18d); in contrast with the relatively less-accurate line-scan profiles taken across the islands and the lower lying layer (Figure 4.15).

#### **4.6 Conclusions**

Herein, we performed an extensive investigation in the lateral phase separation and structural behaviour in nano-scale of low-molecular weight F8BT:TFB conjugated polymer thin films, with various blend ratios by weight, using AFM and TEM. We observed sub-micrometre phase-separated domains in the morphology of 1:1, 1:2, 1:3 and 1:4 weight ratios F8BT:TFB thin films for first time.

The 1:1 thin films showed a phase-separated F8BT-rich higher-lying continuous matrix interrupted by TFB-rich lower-lying wells with diameters in the sub-micrometre length scale (a result of the spinodal decomposition mechanism). Increasing the weight fraction of the TFB part, the thin films exhibited phase-separation of a different morphology: TFB-rich flat continuous layer separated by many sub-micrometre length scale F8BT-rich islands extending out of the TFB-rich

layer (a result of the nucleation and growth mechanism). The (low) molecular weight of the polymers used in this study determined the (sub-micrometre) size of the domains in the thin films. We are the first to report a clearly seen sub-micrometre phase separation in polymer blends, which combine the use of two polymers with low ( $M_n < 10$  kg/mol) molecular weight [3]. Furthermore, although it is already known that the phases in the film morphology are not completely pure, we are the first to present the exact morphology of the top free interface of the F8BT:TFB thin film with 1:4 blend ratio and show the formation of TFB nanodomains (and not a wetting layer).

The two different phase-separation behaviours of F8BT:TFB 1:1 and 1:4 thin films were found not to be significantly affected in the lateral direction by adjusting the spin coating and solution concentration parameters, however the vertical step between the domains was found to be altered by several nanometres. Annealing the thin films at 200 °C was found to destroy the well-formed phase-separated domains. An extensive study on the phase transition of F8BT:TFB thin films with blend ratio of 2:1 to 4:1 was also performed, exhibiting no clear phase-separated domains. Finally, increasing the weight fraction of the TFB in the blend, producing thin films with 1:2, 1:3 and 1:4 weight ratio, more rounded, smaller (laterally and vertically) islands were formed.

These detailed investigations on the F8BT:TFB thin films, are expected to be crucial for the determination of the functionality and the efficiency of the devices, as



even a small change in the film morphology in the nano-scale could affect the overall performance of the LEDs/solar cells [23, 35].

## 4.7 References

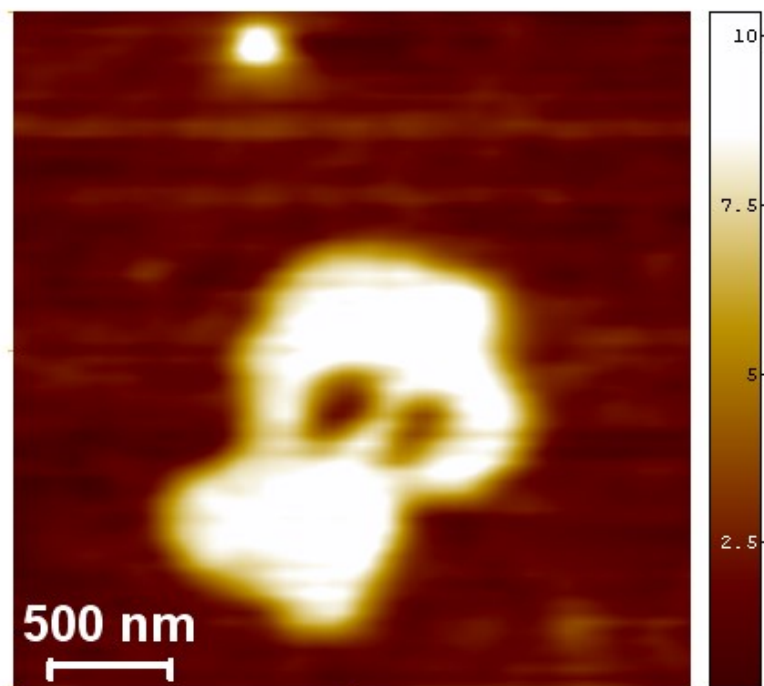
1. Moons E. *Journal of Physics: Condensed Matter* 2002;14(47):12235-12240.
2. Burroughes JH, Bradley DDC, Brown AR, Marks RN, Mackay K, Friend RH, Burns PL, and Holmes AB. *Nature* 1990;347(6293):539-541.
3. Yim K-H, Doherty WJ, Salaneck WR, Murphy CE, Friend RH, and Kim J-S. *Nano Letters* 2010;10(2):385-392.
4. Grice AW, Bradley DDC, Bernius MT, Inbasekaran M, Wu WW, and Woo EP. *Applied Physics Letters* 1998;73(5):629-631.
5. Morteani A, Dhoot A, Kim JS, Silva C, Greenham N, Murphy C, Moons E, Ciná S, Burroughes J, and Friend R. *Advanced Materials* 2003;15(20):1708-1712.
6. Kim JS, Ho PKH, Murphy CE, Baynes N, and Friend RH. *Advanced Materials* 2002;14(3):206-209.
7. Kim J-S, Ho PKH, Murphy CE, and Friend RH. *Macromolecules* 2004;37(8):2861-2871.
8. Joachim C, Gimzewski JK, and Aviram A. *Nature* 2000;408(6812):541-548.
9. Fukuda Y, Watanabe T, Wakimoto T, Miyaguchi S, and Tsuchida M. *Synthetic Metals* 2000;111-112(0):1-6.
10. Christou, V.; Salata, O. V.; Ly, T. Q.; Capecchi, S.; Bailey, N. J.; Cowley, A.; Chippindale, A. M. *Synthetic Metals* 2000;111:7-10.

11. Friend RH, Gymer RW, Holmes AB, Burroughes JH, Marks RN, Taliani C, Bradley DDC, Dos Santos DA, Bredas JL, Logdlund M, and Salaneck WR. *Nature* 1999;397(6715):121-128.
12. Burroughes JH, Cina S, Towns CR, and Heeks K. *Journal of the Society for Information Display* 2001;9(3):187-189.
13. Friend RH. *Pure and Applied Chemistry* 2001;73(No. 3):425-430.
14. Yim KH, Zheng Z, Friend RH, Huck WTS, and Kim JS. *Advanced Functional Materials* 2008;18(19):2897-2904.
15. Alam MM and Jenekhe SA. *Chemistry of Materials* 2004;16(23):4647-4656.
16. Lawrence CJ. *Physics of Fluids* 1988;31(10):2786-2795.
17. Walheim S, Böltau M, Mlynek J, Krausch G, and Steiner U. *Macromolecules* 1997;30(17):4995-5003.
18. Heeger AJ. *Reviews of Modern Physics* 2001;73(3):681-700.
19. Xia Y and Friend RH. *Advanced Materials* 2006;18(11):1371-1376.
20. Arias AC, MacKenzie JD, Stevenson R, Halls JJM, Inbasekaran M, Woo EP, Richards D, and Friend RH. *Macromolecules* 2001;34(17):6005-6013.
21. Corcoran N, Arias AC, Kim JS, MacKenzie JD, and Friend RH. *Applied Physics Letters* 2003;82(2):299-301.
22. Xia YJ and Friend RH. *Applied Physics Letters* 2006;88(16).
23. McNeill CR and Greenham NC. *Advanced Materials* 2009;21(38-39):3840-3850.

24. Cina S. Materials Research Society Spring Conference (MRS 2001), vol. 665. San Francisco, CA: MRS Symposium Proceedings, 2001.
25. Cina S, Baynes N, Moons E, Friend RH, Burroughes J, Towns C, Heeks K, O'Dell R, O'Connor S, and Athanassopoulou N. New, efficient light emitting polymer diode for flat panel display applications. In: Kippelen B and Bradley DDC, editors. Organic Photonic Materials and Devices Iii, vol. 4279. Bellingham: Spie-Int Soc Optical Engineering, 2001. pp. 221-228.
26. Murphy C, Ho P, Kim J-S, Baynes N, and Friend R. ICEL-3. Los Angeles, CA, 2001.
27. Moons E, Murphy C, Butler T, Nice C, Lacey D, Burroughes J, and Friend R. ECME, vol. A35. Kerkerde, The Netherlands: ECME Abstracts, 2001. pp. 89.
28. Moons E. Symposium on New Developments in Display Applications. Oxford: RAL Laboratory, 2000.
29. Van Krevelen DW. Properties of Polymers: Their Correlation with Chemical Structure: Their Numerical Estimation and Prediction from Additive Group Contributions;. Amsterdam: Elsevier, 1990.
30. Herguth P, Jiang X, Liu MS, and Jen AKY. *Macromolecules* 2002;35(16):6094-6100.
31. Campbell AJ, Bradley DDC, and Antoniadis H. *Applied Physics Letters* 2001;79(14):2133-2135.
32. Redecker M, Bradley DDC, Inbasekaran M, Wu WW, and Woo EP. *Advanced Materials* 1999;11(3):241-246.

33. McNeill CR, Watts B, Thomsen L, Belcher WJ, Greenham NC, and Dastoor PC. Nano Letters 2006;6(6):1202-1206.
34. Wang H and Composto RJ. The Journal of Chemical Physics 2000;113(22):10386-10397.
35. McNeill CR, Abrusci A, Zaumseil J, Wilson R, McKiernan MJ, Burroughes JH, Halls JJM, Greenham NC, and Friend RH. Applied Physics Letters 2007;90:193506.
36. Milner ST. Science 1991;251(4996):905-914.

**Chapter 5 Thin Films of  
Conjugated Polymer Blend-  
Nanoparticle Composites**



**AFM topography image of F8BT:TFB 1:4/CdSe composite thin film (colour scale units in nm).**

## 5.1 Introduction

Over the last decades, the unique property of the delocalization in  $\pi$ -conjugated polymer chains led to exceptional optoelectronic properties in polymer field [1]. Due to the low-cost synthesizing methods, conjugated polymers can be promising alternatives to the more expensive conventional inorganic materials in the development of optoelectronic devices. However, there are still many challenges to overcome in order to make the polymer-based devices more efficient and available to large scale applications such as displays, biomedical imaging & sensing, lab-on-a-chip, solid-state lighting and photovoltaic devices [2].

Material-based concerns could negatively affect the performance and the functionality of the devices. For example the low carrier mobilities of the conjugated polymers due to the existence of electron traps in the structure, results in lower efficiency solar cell devices compared to the inorganic semiconductor materials. In addition, conjugated polymers used in light emitting diodes (LEDs), exhibit limitations on getting pure single-colour light with high quantum efficiency. This limitation originates from the fact that the emission spectra of the  $\pi$ -conjugated molecules are very broad ( $\sim 50 - 100$  nm), due to the vibrational and rotational movements inside the molecules.

In the last few years, it has been effectively proven that the hybrid incorporation of inorganic semiconductor nanocrystals in the conjugated polymer blend system enhances the conjugates polymer's optoelectronic/photovoltaic efficiency. The inorganic nanocrystals offer also extra device functionality to the organic-based structures [3].

In this chapter, we will study the thin film morphology in the nanoscale of polyfluorene-based conjugated polymer blends mixed with inorganic semiconductor nanoparticles. For polymer blends we use the electron transporting F8BT and the hole transporting TFB, while for nanoparticles we use the cadmium selenide (CdSe) quantum dots (QDs). The polymer blend exhibits excellent optoelectronic and good photovoltaic behaviour, as well as a straight forward process of mixing [2].

We will focus on the effect of the QDs on the polymer phase-separation of the system comparing the results with the pure blend system studied in the previous chapter, using atomic force microscopy (AFM) and transmission electron microscopy (TEM) techniques. We will propose a mixing recipe of QD-polymer blend (PB), so that the phase-separation of the polymer blends would not be destroyed. Then, we will use AFM, TEM and optical microscopy techniques to study the dispersion and the accurate location of the quantum dots on the film surface.

In the case when the F8BT:TFB blend ratio is 1:1, the quantum dots have effectively spread on the F8BT-rich surface and no QDs were observed on the lower lying TFB areas. On the other hand, when the F8BT:TFB blend ratio is  $< 1$ , where the F8BT areas are in the form of island structures surrounded by a TFB layer, the QDs would prefer to form large aggregates on the film surface. However several single quantum dots are also lying on the surface of the F8BT islands. Furthermore, the size of the island domains exhibit lower vertical and lateral dimensions compared with the pure blend systems studied in the previous chapter (one order of magnitude lower). We attributed this to the increase viscosity which the F8BT exhibit, due to the favourable interaction with the quantum dots. All the above led to the interesting



conclusion that the quantum dots prefer the surface of the F8BT to the surface of the TFB.

The conclusion that the quantum dots would prefer to spread on the F8BT areas, is extremely crucial for the device functionality. The high electron transporting properties of the quantum dots is expected to support to the mobility of the electrons in the low electron transporting F8BT polymer.

## **5.2 Background**

Over the last two decades, organic semiconducting materials (conjugated polymers) have become excellent alternatives to inorganic semiconductors [2]. The reason why the conjugated polymers have become so popular originates from the ease of fabrication, large processing, great flexibility to achieve the required properties for the devices and the low fabrication cost [4,5]. Thin films of conjugated polymers have been successfully applied to semiconducting devices such as light emitting diodes (LEDs), thin film transistors, biosensors and organic photovoltaics/solar cells [6].

In particular, conjugated polymer-based solar cells, which have been applied as low-cost alternatives to inorganic solar cells, exhibit solar power efficiencies of up to 2.5% [7]. On the other hand, solar cells based on conventional but more expensive inorganic semiconductors could exhibit efficiencies which vary from 10% - 30% [8]. As mentioned in Chapter 4, the main reason why the inorganic semiconductors exhibit such a high efficiency lies in the higher intrinsic carrier mobilities, meaning that the charges are transferred to the electrodes more quickly. This would ultimately

reduce the current losses, increasing the device performance [9]. In the case of the conjugated polymers; their carrier mobilities are significantly low ( $\sim 10^{-4}$  cm<sup>2</sup>/Vs), due to the existence of several electron traps such as oxygen [10]. For this reason, the need for adding another material with high electron transport properties, which would also provide an interface for charge transfer, is of paramount importance in order to achieve higher photovoltaic efficiency. In order to overcome this issue, small molecules of conjugated compounds have been mixed with polymers, at a concentration which would give way on the formation of percolation pathways enhancing the electron transport [7,11-13]. However, this solution produced devices, which suffered from limited efficiency because of a) not-enough charge transport [12] and b) structural defects in the molecules block the electron transfer [13].

In addition, devices such as mobile phones with colour displays, which are made with organic LEDs, are successfully and widely produced over the last 15 years. Conjugated polymer based LEDs have the great advantage of colour tunability, which can be used to produce full-colour displays of red-green-blue (RGB) emitters. The images in polymer LEDs are generated through the process of fluorescence (electrons make transitions between orbital states of  $\pi$  – conjugated organic molecules) as explained in Chapter 4. However, even in the case of organic LEDs there are some limitations on getting pure single-colour light with high quantum efficiency. This limitation originates from the fact that the emission spectra of the  $\pi$ -conjugated molecules are very broad ( $\sim 50 - 100$  nm), due to the vibrational and rotational movements inside the molecules [14]. Ways to overcome this problem were also investigated by adding new materials in the system, such as europium

chelates, cyanine dyes and layered inorganic – organic perovskite. But the desired emission and device durability was not achieved [15,16].

One of the most efficient ways to solve the charge transport limitations and increase the quantum efficiency is to mix the conjugated polymers with inorganic semiconductor materials. First, charge transfer was found that is increased between the inorganic material with high electron affinity and the conjugate polymer with low ionization potential [17,18]. In addition, Rehm *et al.* [19] noticed that when the polymers are chemically bound with the inorganic crystalline semiconductor nanoparticles which exhibit high electronic-state density, the charge transfers are significantly increased. Alivisatos and *co-workers* [9,17,18] were the first who successfully reported that by mixing conjugated polymers and inorganic semiconductor nanocrystals, efficient solar cells are being produced. In Figure 5.1a, the proposed by Alivisatos group photovoltaic cell is presented. They used the conjugated polymer poly(3-hexylthiophene) (P3HT) as the hole-accepting material blended with colloidal cadmium selenide (CdSe) nanorods, which is the electron transport material. They reported that their device achieved power conversion efficiency of 6.9%, obtained under  $0.1 \text{ mW/cm}^2$  illumination at 515 nm. Second, the quantum efficiency is possible to be increased even by 50% in LEDs, by adding inorganic nanocrystals such as CdSe quantum dots. Coe and *co-workers* [20] prepared an inorganic/organic LED with a single layer of CdSe quantum dots placed between organic thin films, as shown in Figure 5.1b. *They noticed that pairs of electrons and holes are captured directly on the QD surface, producing high recombination luminescence.* Coe reported also that the efficiency of the device

prepared was 25 times higher than the efficiency obtained with other quantum-dot LEDs.

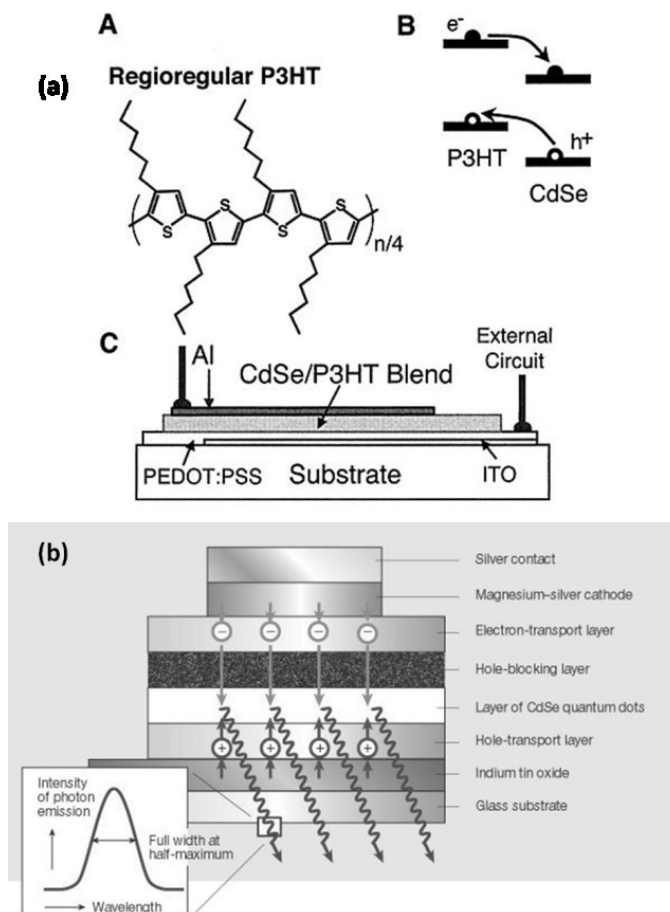


**Figure 5.1 (a) Inorganic (CdSe nanorods)/Organic (P3HT) solar cell device as obtained from Huynh et al. [9]: ‘(A) The structure of regioregular P3HT. (B) The schematic energy level diagram for CdSe nanorods and P3HT showing the charge transfer of electrons to CdSe and holes to P3HT. (C) The device structure consists of a film  $\sim 200$  nm in thickness sandwiched between an aluminium electrode and a transparent conducting electrode of PEDOT:PSS, which was deposited on an indium tin oxide (ITO) glass substrate. The active area of the device is 1.5 mm by 2.0 mm. This film was spin-cast from a solution of 90% wt % CdSe nanorods in P3HT in a pyridine-chloroform solvent mixture.’ (b) Inorganic (CdSe quantum dots)/Organic (TPD) light-emitting diode (LED) made by Coe et al. [20] and Figure obtained from Tsutsui et al. [14]: ‘In this LED, a layer of cadmium–selenium nanocrystals, or quantum dots, is sandwiched between layers of electron-transporting and hole-transporting organic materials. An applied electric field causes electrons and holes to move into the nanocrystal layer, where they are captured in the quantum dots and recombine emitting photons. The spectrum of photon emission is narrow, characterised by its full width at half the maximum value (FWHM).’**

### 5.2.1 Inorganic Nanoparticles and Quantum Dots

In general, nanoparticles are particles, in which the size of at least one dimension is less than 100 nm. The research interest in study and development of nanoparticles is very high, due to the variety of prospective applications, such as in biomedical, optical and electronic fields. The reason why nanoparticles are so popular lies in their small size. They act like a “bridge” between the bulk materials and the atomic and/or molecular structures. Unlike the physical properties of the bulk materials, which are constant and not affected by their size, the physical properties of the nanoparticles are highly dependent on their size. For example in the case of semiconductor nanoparticles, the quantum confinement such as the bandgap is size-dependent. There are two main different types of nanoparticles: the inorganic nanoparticles such the cadmium selenide quantum dots (CdSe QDs) and the organic nanoparticles such as the fullerene-type ([6,6]-phenyl C61 butyric acid methyl ester or PCBM). In Figure 5.2, structures of the inorganic and organic nanoparticles, which are widely used in polymer/inorganic solar cells and LEDs, are presented. Typically the inorganic nanoparticles such as the CdSe are prepared using short chain surfactants, which have a chelating head group (such as the trioctylphosphine oxide or TOPO) and they usually act like colloids in a solution. Inorganic nanoparticles can be prepared with various shapes and sizes (quantum dots or nanocrystals, nanorods, tetarods and hyperbranched). Owing to the quantum-confined nature of the CdSe quantum dots [21], variation of the QD size gives continuous and controllable changes in fluorescent emission [22,23]. This turns the

CdSe QDs into useful materials for applications such as photovoltaic cells [24,25], LEDs [26], biosensors and bio-imaging [27].

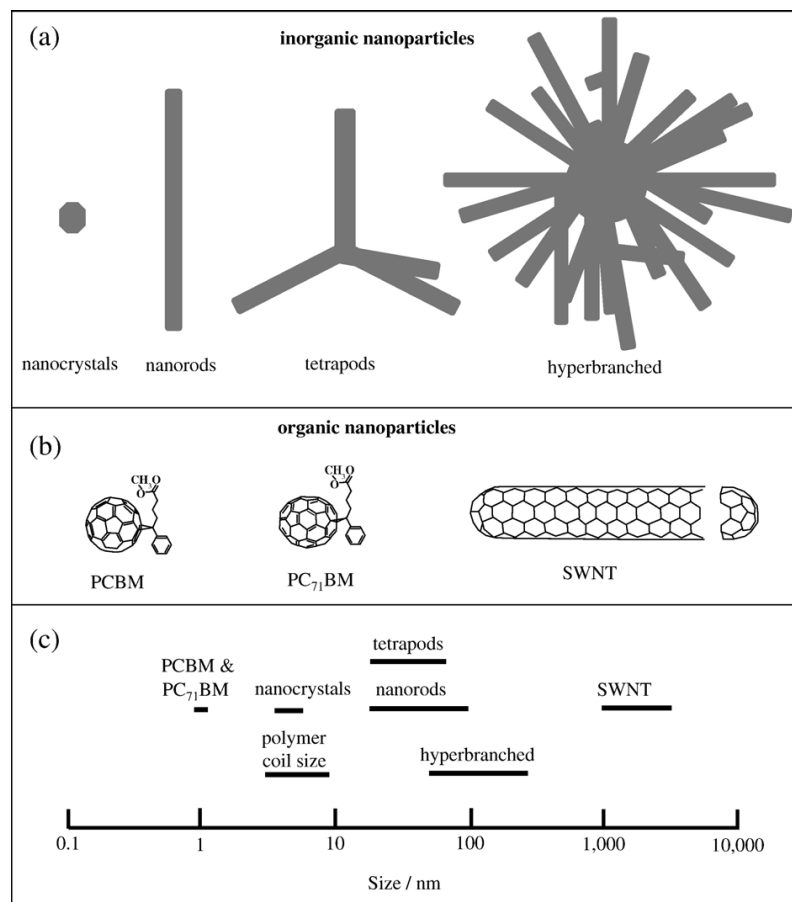


**Figure 5.2** Different types of selected inorganic and organic nanoparticles, used in organic/inorganic solar cells and LEDs as obtained from Saunders et al. [28]: ‘the structures shown in (a) are for CdSe nanoparticles. The structures shown in (b) are for nanoparticles used in organic nanoparticle–polymer PV cells and LEDs. The size ranges shown in (c) are estimates based on literature reports where the nanoparticles have been used in nanoparticle–polymer PV cells.’

Quantum dots (QDs), are nanoparticles of a semiconductor material mainly chalcogenides (selenides or sulfides) of metals like cadmium or zinc (CdSe or ZnS), which range from 2 to 10 nanometres in diameter, whose width is similar to ~ 50 atoms. The excitons (pairs of electrons and holes, shown in Figure 5.3) in QDs are

confined in three-dimensions. As a result these materials have unique electronic properties, which lie between the properties of the bulk semiconductors and the properties of the discrete molecules [29]. The electronic properties of the quantum dots depend on the size and shape of the material; the smaller the size of the QDs, the larger the band gap. When the band gap is large enough (Figure 5.3) i.e. when the difference between the valence and conduction band is large enough, more energy is needed to excite the QD; as a result, more energy (higher frequency) will be released before the QD returns to its relaxation state, emitting sharper light (lower wavelength light due to the higher frequency).

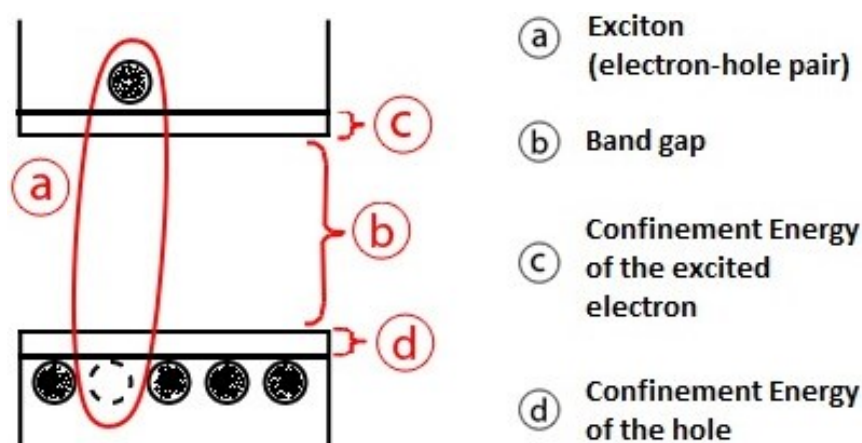


Figure 5.3. Quantum confinement in semiconductors such as the quantum dots, obtained from [30].

The most important property of the QDs is the emission of photons under excitation, which are visible to the human eye. In addition, the wavelength of the QD depends only on the size of the dot and not from the materials, which it is made. The ability of controlling the size of the QDs, which results in tuning the emission wavelength (size quantization effect), makes the QDs very popular candidates for use in optoelectronics and other electronic devices. For example, when the size of the

QDs is relatively small, closer to the blue of the spectrum light is being emitted, while when the size of the QDs is big, then closer to the red light is being emitted. The size of the quantum dots would also make them excellent materials for building solar cells with enhanced efficiency, given the nanoscale nature of light absorption and photocurrent generation in solar energy conversion [9].

As a result, combining the unique optical properties of quantum dots with the electrical properties of conjugated polymers produces inorganic/organic composite alternatives for solar cells and LEDs. The cost of these composite devices can be significantly lower than the conventional inorganic semiconductors, because economical high-volume manufacturing techniques for polymer films can be employed.

### **5.2.2 Mixing Nanoparticles with Conjugated Polymer Blends for Solar Cell and LED production**

Representative semiconductor devices such as solar cells of inorganic nanoparticles – conjugated polymers are usually prepared through a layer by layer process starting from the bottom to the top as presented in Figure 5.4 (obtained from Saunders *et al.* [31]). Each participating photoactive component can be deposited either from solution processing or could be prepared by low-temperature techniques. The bottom layer of the cell is the photoanode which is usually indium tin oxide (ITO)-coated glass. A hole transporting layer usually of PEDOT:PSS is spin cast onto the ITO anode [31]. In addition to the hole-transporting properties of the PEDOT:PSS, this layer is also used to link the Fermi Level of the photoanode to the valence band or else higher occupied molecular orbit (HOMO) of the conjugated



polymer. The photocathode, which is often made from aluminium, is usually deposited via thermal evaporation. The typical layer thickness for each layer, proposed by Saunders *et al.* is also presented in Figure 5.4, suggesting that the total thickness of the solar cell is approximately 500 nm (excluding the glass substrate).

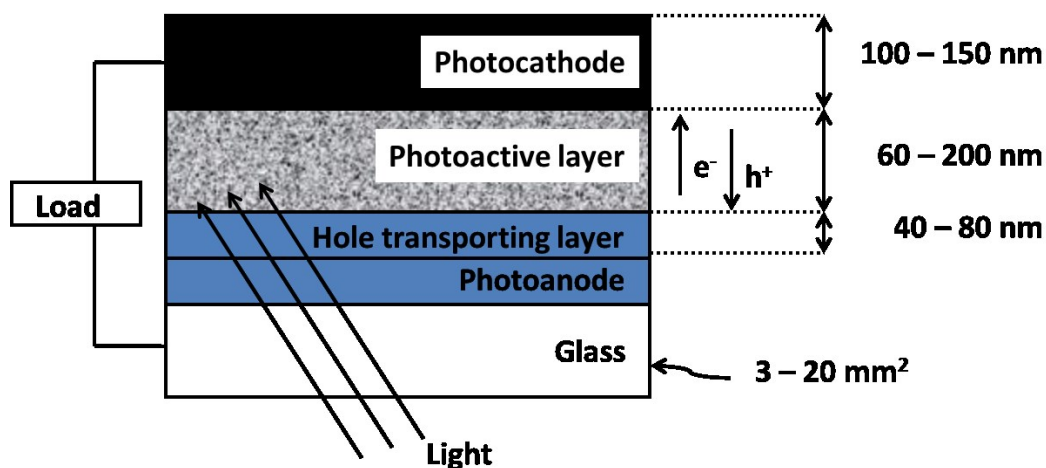
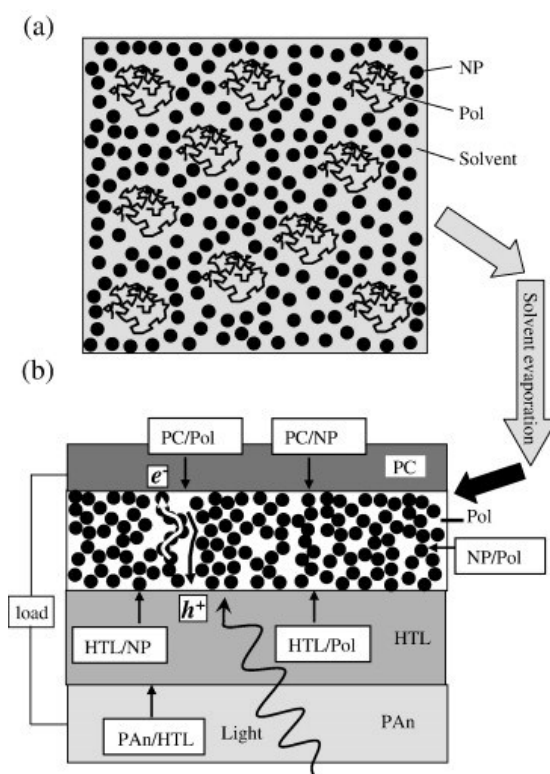


Figure 5.4 Schematic of a typical nanoparticle-conjugated polymer solar cell device. Adapted from Saunders *et al.* [28]: “electrons ( $e^-$ ) and holes ( $h^+$ ) are collected at the photocathode and photoanode, respectively. The hole transporting layer enhances hole transport to the photoanode. Typical ranges of layer thicknesses and PV cell areas are also shown.”

The most crucial part for the functionality and efficiency of the solar cell device is the nanoparticles – polymer photoactive layer. The process of the photoactive layer preparation starts from the dispersion of the colloidal nanoparticles, in polymer solution and it is finalized with the evaporation of the solvent and the formation of the NP – polymer thin film, as shown in the schematics of Figures 5.5a and b obtained from Saunders *et al.* [28]. The nanoparticles are illustrated smaller than the polymer coils; this is typical for organic NP – polymer photoactive layer such as the PCMB-P3HT. In the case of inorganic NP – polymer such as the CdSe-P3HT, the NPs will be larger than the polymer coils [28]. As presented in the

schematic of Figure 5.5b, up to 6 interfaces could be formed in the solar cell. According to Saunders, *good interfacial contact* is needed in order to increase the interfacial areas and decrease the series resistance across the cell. In addition good interfacial contact between the NP-polymer layer and the photocathode has been proven to be a key factor to the efficiency of the PCMB-P3HT solar cell [32].



**Figure 5.5 (a)** The colloidal nanoparticles (NP) mixed with the polymer solution to prepare the photoactive layer after solvent evaporation. **(b)** Schematic of the typical solar cell, presenting all possible interfaces formed. PC is the photocathode, HTL is the hole transporting layer, Pol is the polymer, PAn is the photoanode. Figure obtained from Saunders *et al.* [28].

The photoactive layer is usually prepared via the spin coating technique in inert environment [32]. Figure 5.6 shows what can be considered as general phase diagram of NP (colloid) /polymer/solvent, as obtained from Tuinier and *co-workers* [33] combining experimental, theoretical and simulation results. The mixture usually

contains more than 90% vol. of solvent prior spin coating. For the construction of the general phase diagram, several hypotheses were taken into account, such as the full solubility of the polymer in the solvent and at the same time the nanoparticles are assumed to remain dispersed in a binary nanoparticle-solvent system. The NPs would remain dispersed until their volume fraction reaches a critical value ( $\eta \sim 0.5$ ), which is linked with the NPs size and shape, composition and solvent-NP interaction. On top of that, the phase diagram becomes more complicated when instead of one polymer like the P3HT, the system consists of conjugated polymer blends such as the F8BT:TFB. As shown in Figure 5.6, solvent evaporation (increase of the concentration  $\phi$ ) would result in a transition from a one phase to a two phase region. To this stage, high aggregation of the NP and phase-separation of the polymer is highly favoured as the volume fraction ( $\eta$ ) of NP and the effective concentration ( $\phi/\phi^*$ , where  $\phi^*$  is the overlap concentration which signifies the onset of the semidilute regime) of the polymer increases. During spin coating, which is a highly controllable means of solvent evaporation, the extensive NP-aggregation and polymer phase-separation gives a “bicontinuous solid dispersion” [28]. To the best of our knowledge, there are no published phase diagrams for specific NP-polymer-solvent systems for neither solar cells nor LED applications.

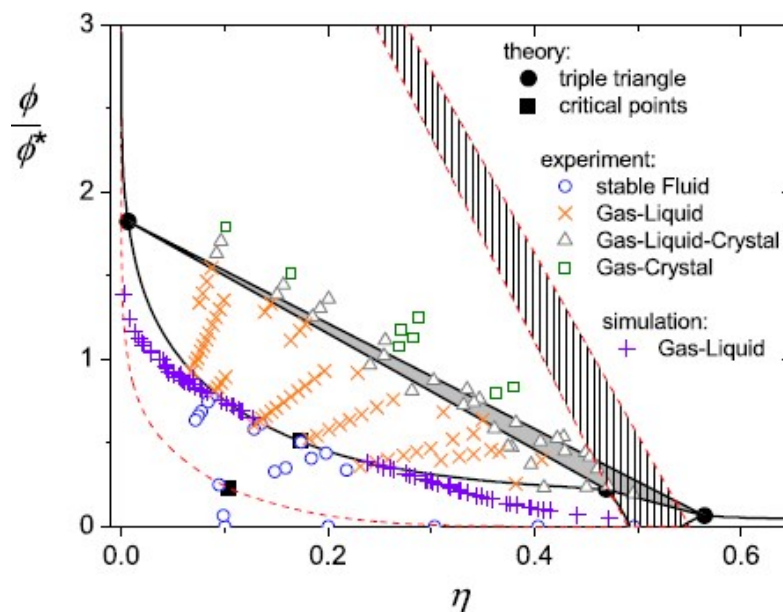


Figure 5.6 Phase diagram of a colloid (NP)-polymer mixture as obtained from Tunier *et al.* [33].  $\phi/\phi^*$  is the effective concentration of the polymer and  $\eta$  is the volume fraction of the colloid (nanoparticles).

### 5.2.3 F8BT:TFB Polymer Blends mixed with Quantum Dots to Produce Composite Thin Films for use in Semiconducting Devices

Compared to the most commonly used and studied conjugated polymers such as the polyphenylenes, polythiophenes, polypyrroles and polyanalines, polyfluorenes have the advantage of better processing, less sensitivity to chemical degradation i.e. increased durability. In the meantime polyfluorene-based LEDs and solar cells exhibit excellent efficiency [2]. The above make the polyfluorenes good candidates for further study to produce more efficient semiconductor devices. More precisely, as already mentioned in the previous Chapter, LEDs with excellent efficiency have been fabricated using a blend of the electron transport F8BT polymer and the hole transport TFB polymer [2]. Furthermore, same blends of F8BT:TFB polyfluorenes

have been used to prepare solar cells with satisfactory efficiency, but by replacing the hole-transport TFB with the PFB, the efficiency of the solar cell devices increased significantly [34]. Owing to the key role of the interface in conjugated polymer-based devices; the control of phase-separation after deposition on the solid substrate via spin coating is of paramount importance. This was extensively presented and studied in the previous chapter.

Figure 5.7 presents the typical energy diagrams and the typical configuration of the devices for LEDs (left) and solar cells (right). The electron transporting (F8BT) polymer is presented as ETL and the hole transporting (TFB) as HTL. In the case of LEDs, holes and electrons are injected from the ITO anode and from the Al cathode, respectively. To enhance the carrier injection and reduce exciton loss at the polymer active layer-electrode interface, a thin layer of PEDOT:PSS and Calcium (Ca) could be added at the anode and cathode, respectively. On the other hand, the configuration of the solar cell device is similar to the LED; however, there is no need of PEDOT:PSS and Ca layers. In this case the exciton is photo-generated in the TFB polymer and dissociates when it reaches the energy barrier at the F8BT:TFB interface to allow carrier extraction [3].

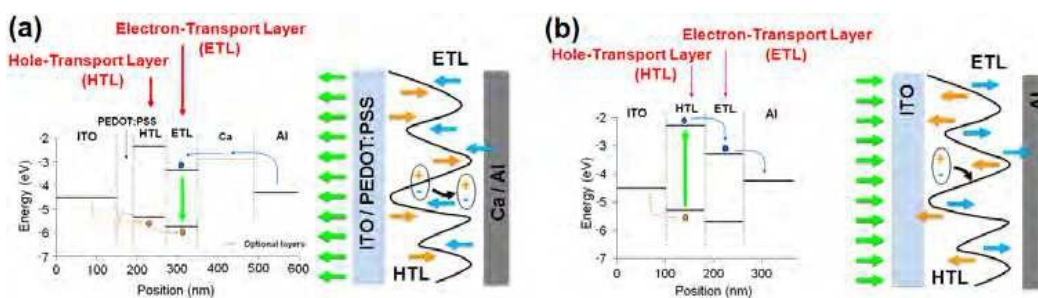


**Figure 5.7** Energy diagrams (left) and schematics (right) of F8BT:TFB polymer blends-based semiconductor devices for (a) LEDs and (b) solar cells. Figure obtained from ref. [3].

However, the hole transporting part of the polyfluorene blends, yields conductivities higher than  $1,000 \Omega^{-1}\text{cm}^{-1}$ , a value which is very difficult to achieve in the electron transporting polymer. As a result the electron-transporting polymer, often affects the overall performances of polymer-based devices [2]. Inorganic nanoparticles such as the quantum dots, which exhibit excellent electron transporting properties, are proved to be excellent additives to the polymer blends, enhancing the device efficiency [3]. As a result mixing nanoparticles with the polyfluorene-blend solutions and study the structural behaviour on solid films after solvent evaporation is crucial for the progress in the efficiency of LED and solar cell devices. Despite the significance of the ability to control the phase-separation in polymer blend-NP systems, to the best of our knowledge few studies have investigated this aspect.

Cloutier, in his chapter has recently reported the effect of lead-sulfite (PbS) colloidal quantum dots on the structural morphology of the F8BT:TFB blends and on the functionality of the optoelectronic devices [3]. Figure 5.8 (obtained from Cloutier), presents the TFB:F8BT blend system, which offers an ideal host system for semiconductor nanocrystals such as the PbS. He stated that this system provides heterostructures for low-cost and high-performance devices, which find application to lab-on-a-chip, flexible optoelectronics, night-vision and solar energy fields.

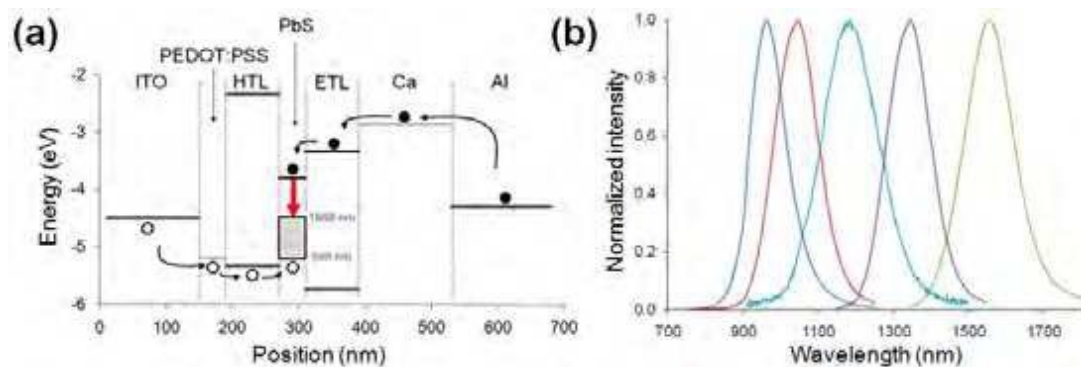


**Figure 5.8** Quantum dots - polyfluorene-based LED heterostructures, obtained from Cloutier [3]: (a) F8BT:TFB energy system, which provides an excellent host system for nanocrystals such as the PbS. (b) The incorporation of PbS nanocrystals can migrate their operation to the near-infrared (between 900 - 1600 nm), depending on their size.

According to Cloutier, the most efficient way to produce the heterostructures of F8BT:TFB and quantum dot nanoparticles is simply to mix the colloidal QDs with the polymer blend solution and then spin cast on the solid substrate to produce the active film. He assumed that after deposition, the QDs would spread homogeneously in the blended polymer film, but only the quantum dots which are placed within the interfaces (tens of nanometres area) would be active. The rest of the QDs would remain inactive. To achieve that, very large concentrations of QDs are needed, in order to increase the chances to obtain more active QDs in the film. However, this procedure might cause significant problems on the performance of the polymer blend film, which hosts the colloidal QDs.

In order for Cloutier to study the effect of the PbS quantum dots on the F8BT:TFB polymer blend film, he used confocal fluorescence mapping of F8BT:TFB films with and without the colloidal QDs. The vision intensity images, which are shown in Figure 5.9, present the structural behaviour and the phase-

separation of the blended films without QDs (Figure 5.9a) and with embedded colloidal QDs (Figure 5.9b). According to Cloutier, the brighter domains shown in the images are F8BT-rich, while the darker domains are TFB-rich. It is obvious from the images that the domains in the films with the colloidal QDs are significantly smaller, compared with the domains observed in the film without the colloidal QDs. The reason why this is happening was not discussed in the Cloutier study.

To this point, we should notice that the author of ref [3] did not specify the volume fractions of the F8BT and TFB blends, as well as the volume fraction of the colloidal QDs in the solution. Furthermore, by using *only* confocal microscopy techniques is too difficult to locate the QDs in the film and fully investigate the effect of the NPs on the ultimate nanophase-separation of the blends both in lateral and vertical dimensions. It is more than obvious that at this stage there are many more things to be done in order to fully understand and control the structural behaviour of the films. Then it would be possible to fabricate devices such as LEDs and solar cells with potentially improved performance.

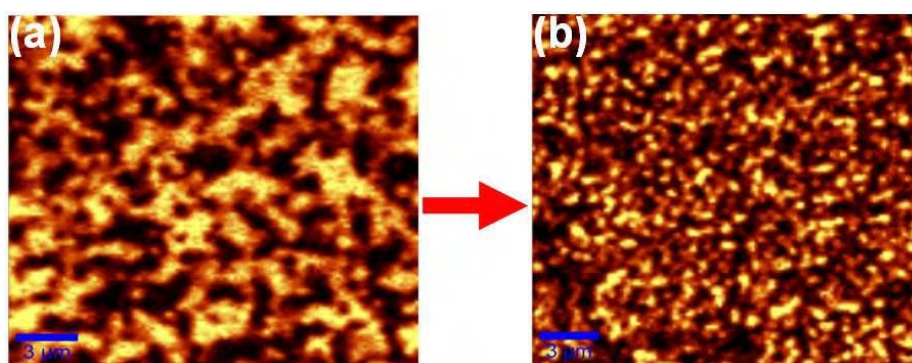


**Figure 5.9** The effect of the QD on the F8BT:TFB blended films, as obtained from ref. [3]: “confocal fluorescence mapping of the domain structure for the same toluene-blended TFB:F8BT (a) without PbS QDs and (b) with PbS QDs. The scale bars are 3  $\mu\text{m}$ .



Herein, we performed a first study of the effect of CdSe quantum dots on the phase behaviour of F8BT:TFB thin films. We prepared solutions of QDs – F8BT:TFB blends (with various polymer blend ratios) in three different mass ratios (2:1, 1:1, 1:2). Droplets of the solutions were then spin coated on freshly cleaved ultra-flat mica to produce  $\sim 70 - 80$  nm thin films. The structural behaviour of the inorganic-organic thin films was investigated by tapping-mode atomic force microscopy (AFM, height and phase imaging). Furthermore, for the accurate detection of the QDs in the film, apart from the height and phase imaging AFM we also used adhesion imaging AFM (force curved based imaging mode), mass-thickness contrast and dark field transmission electron microscopy (MTC and DF TEM) and optical microscopy with a fitted fluorescence camera. To the best of our knowledge we are the first who managed to determine the exact volume of QDs needed in order to maintain the phase-separation of the polymer blends and at the same time to detect several QDs across the film. In all cases, clusters of QDs on the top surface of the film were unavoidable.

The first important observation is that the phase-separated domains although they maintained their shape, their size was decreased significantly. This change is crucial for the functionality of the film as an active part of the device, as the interface between the parts of the films is increased. Furthermore, we managed to locate the existence of several QDs away from the QD aggregates. These were located at the edge of the F8BT-rich areas close to the interface of F8BT-rich and TFB-rich polymers. From the techniques applied we have strong evidence that the QDs do not want to ‘lie’ on the TFB-rich phase. They would always prefer to segregate on the

film surface or within the F8BT-rich area. The preference of the QDs in one of the polymers, leads to higher viscosity of the system during spin cast. The latter would result in the earlier arrest of the phase separation, i.e. before the diffusion of the TFB polymer in the F8BT domains.

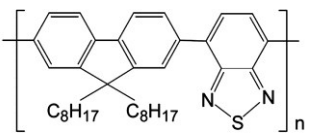
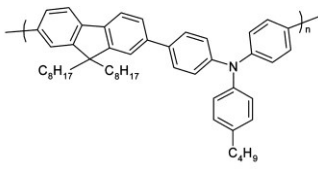
Due to the importance of the interfaces in the polymer-based devices, our findings give promising tools for understanding and controlling, the phase-separation of the polymer blends and the behaviour of the QDs in the system.

### 5.3 Experimental

#### 5.3.1 Materials

**Polymers:** the conjugated polymer blends applied for our present study consisted of F8BT parts ( $M_n = 6.2$  kg/mol) and TFB parts ( $M_n = 5.8$  kg/mol), whose chemical structures are presented in Table 5.1. Polymers were purchased by American Dye Source, Inc (Quebec, Canada).

**Table 5.1 Properties and chemical structures of the Polymers Studied**

Polymer	$M_n^a$ (kg/mol)	Polydispersity	Chemical Structure
F8BT	6.2	7.4	
TFB	5.8	2.6	

<sup>a</sup> From gel permeation chromatography (GPC).

**Inorganic Nanoparticles:** the inorganic nanoparticles (NP) Lumidot™ Cadmium Selenide (CdSe) quantum dots (QD) were purchased by Sigma - Aldrich Chemicals (Sigma-Aldrich Company Ltd., Dorset, United Kingdom). The properties of the quantum dots are presented in Table 5.2. The capping agent of the quantum dots is the hexadecylamine (HDA).

**Table 5.2 Properties of the Quantum Dots used.**

Quantum Dots	Concentration (mg/mL) in toluene	Fluorescence, $\lambda_{em}$ (nm) <sup>a</sup>	particle size (nm) <sup>b</sup>	UV absorption (nm) <sup>a</sup>
CdSe	5	475-485	~ 2.1	455-465

<sup>a</sup> Quantum yield was measured following the procedure of Qu and *co-workers* [35]. <sup>b</sup> Particle size was determined by TEM according to the procedure of Yu and *co-workers* [36].

### 5.3.2 Inorganic Nanoparticle - Polymer Solutions

First the polymer solutions were prepared by dissolving each conjugated polymer in *p*-xylene purchased by Sigma-Aldrich Ltd. (Dorset, United Kingdom) to produce a concentration of 14 mg/ml. F8BT and TFB solutions were then mixed to produce blends of various ratios 1:1, 1:2, 1:3 and 1:4 by weight. Second, the cadmium selenide quantum dots were dissolved in *p*-xylene. To achieve that, we first had to isolate the QDs from the toluene solution (as received) with centrifuge technique. 8 flasks of 1 ml capacity were filled with 250  $\mu$ l QD-toluene solution and 750  $\mu$ l of methanol each. The flasks were shaken up-side down and then they were loaded on the centrifuge (MicroCentaur, MSE, London, United Kingdom). The filled

flasks were centrifuged at 1300 rpm for 30 minutes. After centrifuging, the QDs were found at the bottom of the flask having a distinctive yellow colour as shown in the schematic of Figure 5.10. The methanol/toluene solution was then removed from the flasks using a single-use glass pipette. Furthermore, 250  $\mu\text{l}$  of *p*-xylene were added in every flask (8 flasks  $\times$  250  $\mu\text{l}$  = 2 ml of *p*-xylene), to achieve the same concentration as purchased from the industry (5 mg/ml in toluene). Then the taps of the flasks were covered with a Teflon tape to ensure that the solution will not evaporate. The flasks were extensively shaken and their container was placed in a cleaved bottle. The bottle with the QDs in *p*-xylene was loaded in Ultrasonic bath (FB11002, Fisherbrand, Fisher Scientific, Loughborough, United Kingdom) for 60 minutes to ensure the complete dilution of the QDs in *p*-xylene.

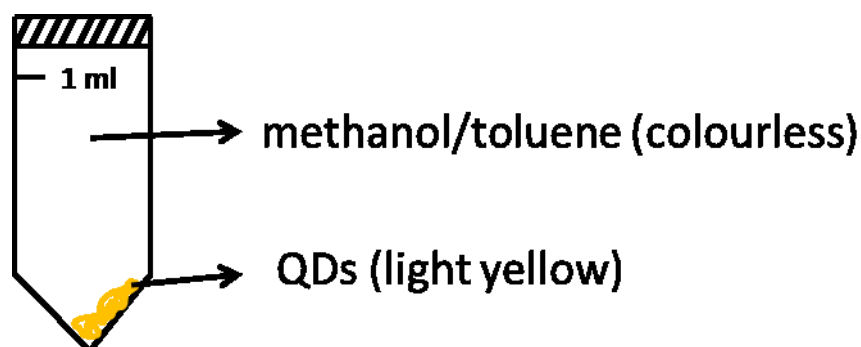


**Figure 5.10** Schematic of the flask (8 in total) upon centrifuge at 1300 rpm for 30 min. The outcome consisted of a cluster of quantum dots with a distinctive yellow colour at the bottom of the flask and a colourless solution of methanol and toluene.

At this point we were ready to mix the polymer blend solutions with the CdSe quantum dots. As shown in the hierarchy diagram of Figure 5.11, the 1:1, 1:2, 1:3 and 1:4 conjugated polymer blends (PB) with concentration 14 mg/ml were mixed with QDs with concentration 5 mg/ml in a weight ratio for the solutions of 1:1, 2:1

and 1:2. These correspond to 14:5, 28:5 and 14:10 mass ratios, respectively between the pure polymer blend and quantum dots. Exceptions are the conjugated polymer solutions with TFB or F8BT parts only, where the solutions were mixed only in a weight ratio of 2:1 (corresponding to 28:5 mass ratio between the pure polymer and quantum dots).

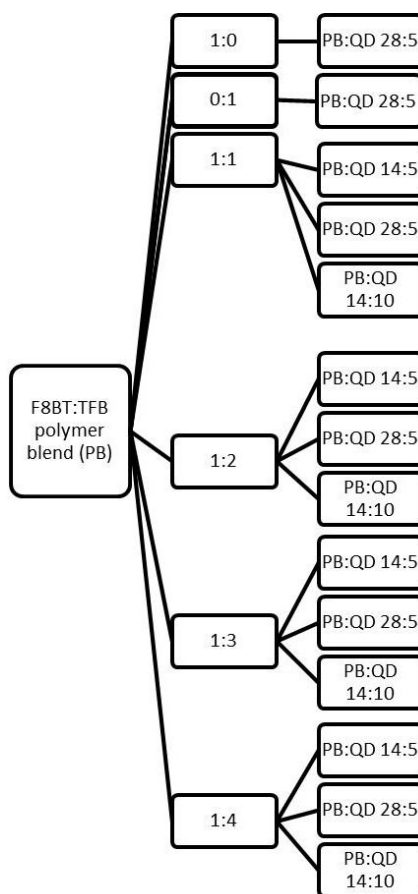


Figure 5.11. Schematic of the organic-inorganic by weight blend solutions prepared for this study.

### 5.3.3 Ultra-Thin-Film Preparation

Droplets of the solutions presented in Figure 5.11, were spin coated (spin coater SPIN150-NPP, SPS-Europe, Putten, the Netherlands) at 4,000 rpm for 90

seconds, on freshly cleaved mica sheets (Agar Scientific, Essex, UK) in ambient conditions, producing ultrathin films (~60 - 80 nm). Upon spin cast the thin films were dried with a stream of nitrogen.

### 5.3.4 Atomic Force Microscopy

A Bruker AFM Multimode/Nanoscope IIIa (Bruker, Santa Barbara, CA, USA), equipped with a *J*-scanner ( $x$ - $y$  range  $\approx 140 \mu\text{m}$ ) or an *E*-scanner ( $x$ - $y$  range  $\approx 14 \mu\text{m}$ ) was used to study the morphological behaviour of the organic F8BT:TFB blends – inorganic QD thin films in the tapping-mode. RTESP and/or RTESPA Bruker cantilevers with a nominal spring constant and resonance frequency of 40 N/m and 300 kHz respectively were used to image the samples. In order to minimize the interaction force between the tip and the substrate (but without losing contact) “light tapping” was used by keeping the set-point amplitude ratio  $r_{\text{sp}} = A_{\text{sp}}/A_0$  close to 1 (where  $A_0$  and  $A_{\text{sp}}$  are the free oscillation amplitude and the reduced scanning set-point amplitude of the cantilever, respectively).

In addition, we used the advanced QI<sup>TM</sup> (quantitative imaging) mode developed by JPK Instruments (NanoWizard II AFM, JPK Instruments AG, Berlin, Germany) to obtain high resolution adhesion and height details of the composite thin films. This mode works without applying lateral forces in the film and at the same time it enables the constant control (in every pixel) of the vertical forces (tip-surface) i.e. it combines the advantages of both the tapping (minimal lateral/friction forces – ideal for soft samples) and the contact (high resolution) modes. QI<sup>TM</sup> mode is a force curve

based high-resolution imaging mode in which there is no need of adjusting neither the amplitude set-point nor the gain during imaging.

According to JPK Instruments, the QI™ mode “uses a novel tip movement algorithm, which measures a real and complete force distance curve at every pixel of the image and gives all information about the local tip-sample interaction with high spatial resolution”. The interaction between the tip and the sample is possible to be controlled and minimised even down to a few picometres. In addition, it should be pointed out that in this novel mode, during the process of obtaining a force-distance curve there are no *xy*-movements ensuring that the curve is obtained under constant velocity. The latter is crucial for accurate and meaningful adhesion data, because of the coupling between the measured adhesion and the velocity during a force distance curve [37]. In the adhesion mapping in QI™ mode, the maximum unbinding force (the absolute value of the maximum force) is calculated during scanning and it is displayed in the adhesion image. To achieve this, the highest adhesion values are identified during the retraction step in the force-distance curve. In later adhesion data analysis, it is possible to navigate across the image and look at single force distance curves to distinguish between the different tip-surface interactions forces and perform a material analysis on the film surface.

In this present work, the force of adhesion was measured and it is associated with the maximum (in absolute value) during retraction of the tip from the sample. In addition to the adhesion mapping the corresponding height images are also presented. The data for height imaging were generated from the (unique for every

pixel) force distance curve, having as a standard value the sensor height at the trigger point, which is set to small values in order to minimize the forces between the cantilever and the film surface. Mikromasch, CSC37 cantilevers with a nominal spring constant and resonance frequency of 0.3 N/m and 20 kHz respectively, were used to scan the samples. For the adhesion mapping the cantilever was automatically calibrated by the JPK machine using the thermal noise method and the spring constant was found to be 0.283 N/m. Images were processed and the layer heights were measured using the software Scanning Probe Image Processor (SPIP, Image Metrology, Hørsholm, Denmark) and the JPKSPM data processing (JPK Instruments AG, Berlin, Germany).

### **5.3.5 Transmission Electron Microscopy**

The composite PB:QD thin layers were lifted off from mica substrates by gentle immersion into a deionized water bath and then placed on a 200 square mesh copper grid. The specimens were analysed in a FEI Tecnai T20 tunnelling electron microscope (TEM) EM (FEI, Oregon, United States of America), operated at 200 kV and it is equipped with an Olympus-SIS Megaview III CCD camera (Olympus Soft Imaging Solutions GmbH, Münster, Germany). We used an objective aperture of 20  $\mu\text{m}$  and defocus value of approximately 10  $\mu\text{m}$ . The software used to process the TEM images is the Micrograph<sup>™</sup> (Gatan, Abingdon, UK).



## 5.4 Results and Discussion

### 5.4.1 CdSe Quantum Dots on Mica

Figure 5.12 presents AFM 2D and 3D height images of two different scanning areas (Figures 5.12a, b and c) and a phase image (Figure 5.12d) of colloidal CdSe nanoparticle quantum dots (from concentration 5 mg/ml) spin cast on mica. The quantum dots are spread homogeneously on the mica surface, without forming any clusters on the top surface. The average height of the quantum dots is  $\sim 2.15 \pm 0.47$  nm (calculated by post-processing particle analysis performed in the image presented in Figure 5.12c), which compares very well with the nominal size of the QDs  $\sim 2.1$  nm. Note that the lateral size of the QDs is bigger than  $\sim 2.1$  nm ( $\sim 23.60 \pm 7.2$  nm), due to the tip-sample convolution (the probe tip apex diameter is larger than the features we image) [37]. Furthermore, phase imaging reveals a clear contrast between the dots and the layer below, confirming that there are no QD-rich layers formed on top of the mica and below the single QDs. The fact that the QDs are dispersed on mica, confirms that the quantum dots were diluted in the *p*-xylene, in agreement with earlier studies on CdSe quantum dots diluted in xylene solutions [38-40]. This is an important result, as we can use the QD solutions to mix them with the polymer blends solutions (diluted in *p*-xylene) and produce thin films with potentially homogeneous distribution (if not affected by the phase separation).

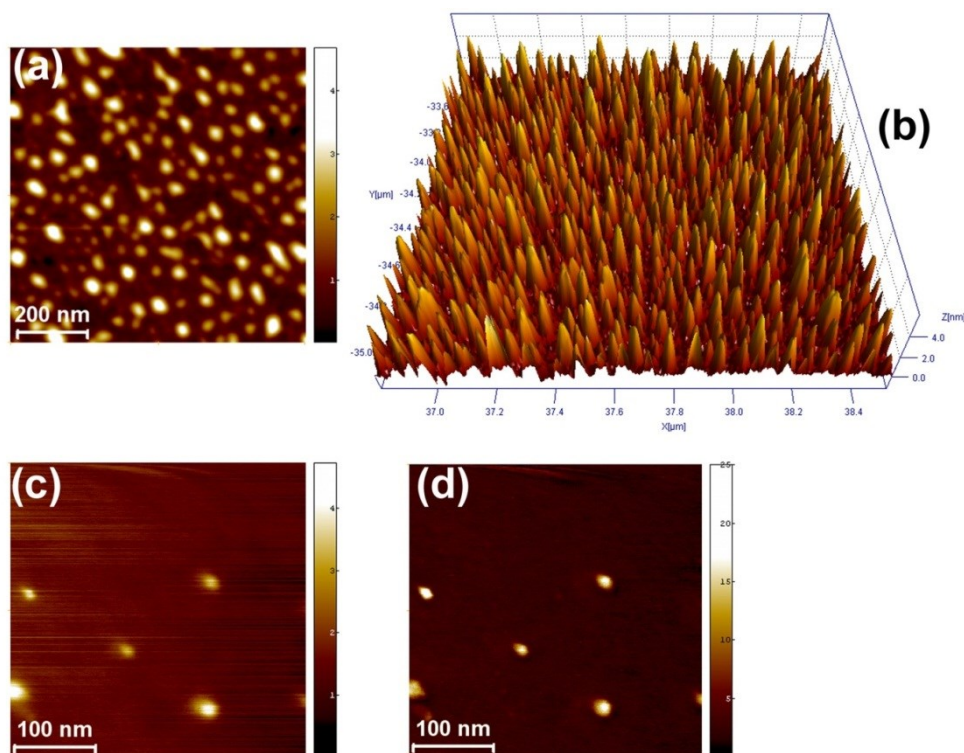


**Figure 5.12** (a) (b) AFM height images 2D and 3D of CdSe QDs spin cast on mica from p-xylene solution; the scan size of the image is  $1.7 \times 1.7 \mu\text{m}^2$  and the z-scale is 5 nm; (c) (d) AFM height (c) and phase (d) images of QDs on mica; the scan size of the image is  $360 \times 360 \text{ nm}^2$  and the z-scale for (c) is 5 nm and for (d) is 25 degrees.

#### 5.4.2 F8BT and TFB thin films mixed with QDs

Figure 5.13 presents AFM height and phase images of thin films from F8BT (Figures 5.13a and b) and from TFB (Figures 5.13c and d) mixed with CdSe quantum dots in a weight ratio of 28:5. Thin film morphology of the F8BT mixed with QDs is characterised by a relatively flat layer with many small bright spots and some larger holes and fewer thicker islands. The wells are of diameter in the range of  $\sim 50 - 200 \text{ nm}$ . The phase contrast revealed that a uniform F8BT layer was formed direct on top of the mica, while the quantum dots were spread on top of the F8BT layer (small bright spots). The situation in the TFB mixed with QDs is significantly

different. In the height image (Figure 5.13c), the formation of several large islands formed on top of a flat layer were observed. The phase contrast of the corresponding height image revealed the formation of a clear lateral phase-separation. Alternate phases of TFB and QD were formed on top of the mica. Comparing, our findings on the F8BT-QD and TFB-QD with our findings on the F8BT and TFB thin films from the previous chapter, we conclude that the quantum dots do not wet the surface of the TFB polymer layer. A flat TFB layer was formed in TFB-only thin films, but adding the quantum dots, the flat layer is destroyed, forming two lateral phases instead: one phase TFB-rich and one phase QD-rich. On the other hand, in the F8BT case, the quantum dots have successfully wetted the F8BT layer.

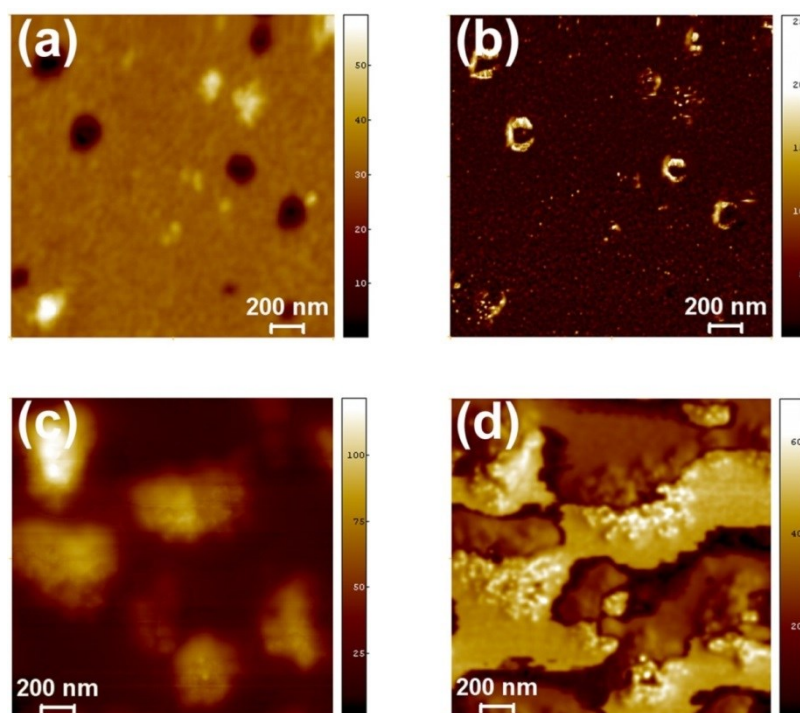


**Figure 5.13** AFM height (a) (c) and phase (b) (d) images of F8BT mixed with CdSe QDs (a, b) and TFB mixed with CdSe QDs (c, d) thin films spin cast on mica (scan size:  $2 \times 2 \mu\text{m}^2$ , colour scales in nm).

### 5.4.3 Thin films of F8BT:TFB polymer blends mixed with 3 different weight ratios of CdSe quantum dots.

Figure 5.14 presents typical AFM height images of F8BT:TFB polymer blend (PB) thin films with blend ratio 1:1, 1:2, 1:3 and 1:4 (vertical columns), mixed with CdSe QDs in solution weight ratio 28:5, 14:5 and 14:10 (horizontal columns).

The thin film of F8BT:TFB 1:1 with PB:QD 28:5 (Figure 5.14a) consists of well-like structures, which are surrounded by a higher lying matrix as observed in the previous chapter for the polymer blend alone indicating the same type of phase separation. However, on top of the matrix, some irregular island-like (with various sizes and shapes) structures were formed. Increasing the weight fraction of the QDs to 14:5 (PB:QD), the phase-separation was destroyed. Several irregular shaped island-like structures were formed on top of a uniform layer (Figure 5.14b). These islands became larger and fewer, when the QD fraction was increased to 14:10 (Figure 5.14c).

The thin film of F8BT:TFB 1:2 mixed with QDs in mass ratio of PB:QD 28:5 (Figure 5.14d) consists of several island-like structures extended out of a homogeneous matrix as expected from the pure blend behaviour. On the top surface, few larger islands were formed. Thin films of the same F8BT:TFB blend but with PB:QD 14:5 (Figure 5.14e) and PB:QD 14:10 (Figure 5.14f), exhibited irregular structural morphology with no clear phase-separated domains. Rounded island domains, which increased in size in the higher QD fraction, were observed on the top surface.

Figure 5.14g presents the morphology of F8BT:TFB 1:3 with QDs in mass fraction PB:QD 28:5 thin film. The morphology is characterised by the formation of several small island-like domains spread across the film and extended out of a homogeneous matrix. At the top surface of the film larger (few) island-like domains are formed. Similarly to the previous cases, increasing the QD fraction in the system increases the larger islands on top (Figures 5.14h and i). However, it has to be noted that in this case (polymer blend with 1:3 ratio) the small domains remain when the colloidal quantum dots concentration was increased to PB:QD 14:5 indicating that the phase-separation could persist.

Finally, thin films of F8BT:TFB 1:4 with QDs in weight fraction PB:QD 28:5 consists of the expected phase separated island-like domains surrounded by a lower-lying matrix (Figure 5.14j). Again, some larger structures were observed at the top surface. Increasing the weight fraction of the QDs in the system, the phase-separated domains seem to disappear and several larger irregular island structures were formed instead (Figures 5.14k and l).

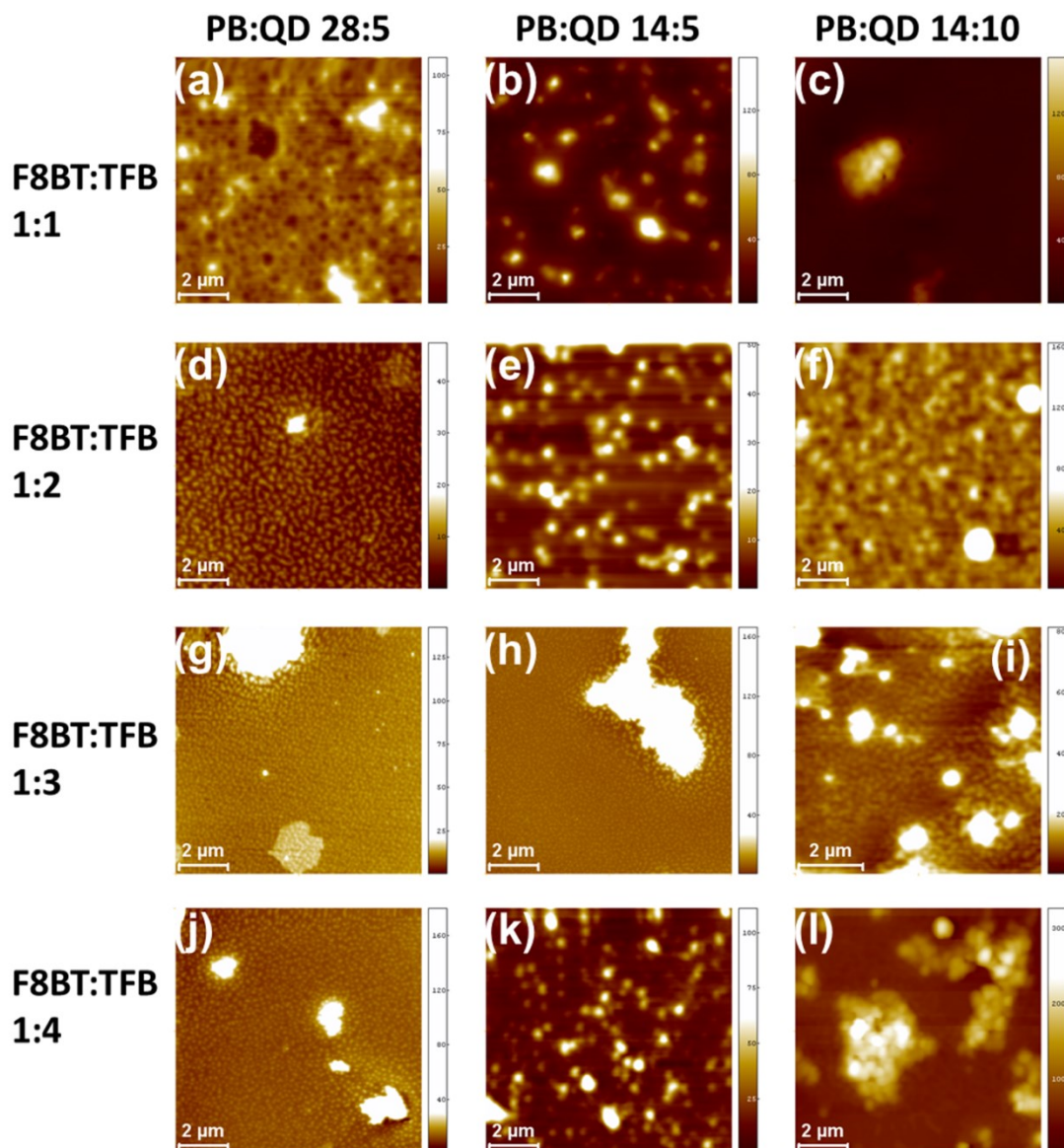


**Figure 5.14** Overview of typical AFM height images of F8BT:TFB polymer blend (PB) thin films spin cast on mica from four different blend ratios: 1:1, 1:2, 1:3 and 1:4 (rows), mixed with CdSe QDs in three PB:QD ratios: 28:5, 14:5 and 14:10 (columns). The scan size of the images is approximately  $10 \times 10 \mu\text{m}^2$ ; the colour scales are in nm.

From the Figure 5.14 presented above, we obtained valuable information for the phase behaviour of the polymer blend when mixed with CdSe QDs. Understanding of the phase evolution in blend thin films with QDs demands prior knowledge of the phase behaviour of the polymer blends. This knowledge was

obtained in the previous chapter where the F8BT and TFB parts were phase separated into discrete phases depending on the volume ratio of the blends. In this case, we observed that with the appropriate volume of QDs in the polymer blends, the phase-separation of the F8BT:TFB studied in the previous chapter remained the same. This was achieved at the lowest concentration of QDs: PB:QD 28:5. However, there are parameters such as the size and the interface of the phase-separated domains, which were affected from the QDs as will be analysed later.

An earlier study on conventional blend (PMMA-SAN)/NPs (silica) composite thin films confirmed that when the fraction of the NPs in the system passes a critical point then large NP clusters are formed destroying the phase separation of the polymer blend [41]. In this fundamental study, the concentration of the NPs in the PMMA-SAN 1:1 system was increased from 0.5 wt% to 5 wt%. They found that the size of the phase-separated domains decreased when the weight fraction of the nanoparticles increased and was destroyed at 5 wt%. Stable bicontinuous structures in polymer blend-NP thin films at low nanoparticle fraction were also confirmed in a later study from Gam and *co-workers* [42]. Furthermore, more recent computer simulations performed by Araki *et al.* [43], showed significant transitions in the morphology of symmetric AB blends, with the addition of nanoparticles. They reported that at high concentrations of nanoparticles, the polymer A which prefers to cover the A-like nanoparticles is not enough, leading to the formation of a “wetting-induced depletion”. This depletion enhances the formation of unusual morphologies as a function of the volume fraction of the nanoparticles. As a result the

concentration of the nanoparticles offers a simple process to control the overall morphology of immiscible polymer blend-nanoparticle mixtures.

In addition to the general influence of the QDs in the total system, the detection of the position of the quantum dots in these films is essential in order to fully understand the structural behaviour of these composite films i.e. the exact effect of the QDs in the phase separated domains in the nanoscale. In this study we will focus on the thin films with PB:QD 28:5 only. In general, the rest of the films do not show any clear lateral phase-separated domains and it is likely that the quantum dots had formed large clusters in the films destroying the valuable -for the function of future device- interfaces.

In Figure 5.15, we concentrate on AFM height images presenting the morphology of the F8BT:TFB 1:1 blended film embedded with QDs. There are three phases observed in the morphology of this film. The first two phases refer to the phase-separation of the F8BT and the TFB parts. As we extensively studied in the previous chapter, a TFB-rich layer has wetted the mica surface and an F8BT-rich layer with several well-like domains was formed on top of the wetted layer. Now using the QDs, we observe on top of the F8BT-rich layer several bright spots spread across the film surface. Later we are going to show that that these bright spots are small clusters of quantum dots. The zoomed AFM image of Figure 5.15a (small square in Figure 5.15b image) and the height analysis presented in Figure 5.15c reveal that the well-like domains have a typical depth  $27 \pm 4$  nm and lateral dimensions  $\sim 50 - 100$  nm. We should note that the lateral size of the wells is



significantly smaller than the size of the corresponding F8BT:TFB 1:1 thin films without quantum dots ( $400 \pm 200$  nm) as presented in the previous chapter. This observation agrees with the Cloutier study on F8BT:TFB 1:1 thin films without quantum dots and with PbS quantum dots [3]. He found using confocal microscopy that smaller (compared with the pure polymer blend thin films) phase-separated domains were obtained when quantum dots are embedded in the polymer blend system (Figure 5.9).

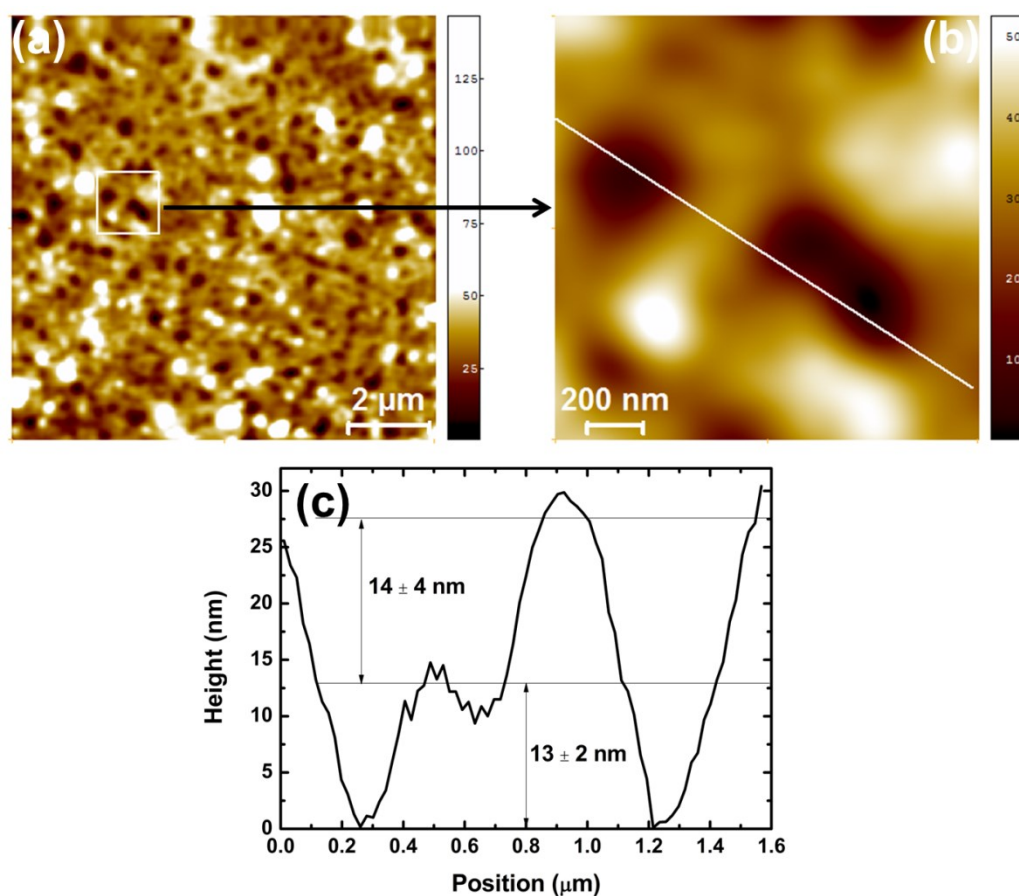


**Figure 5.15** (a) Representative AFM height image of F8BT:TFB 1:1 by weight ratio, mixed with QDs at a weight ratio of PB:QD 28:5 thin film spin cast on mica. (b) Zoomed area corresponding the white square of image (a); The scan size of the images are for (a)  $10 \times 10 \mu\text{m}^2$  and for (b)  $1.5 \times 1.5 \mu\text{m}^2$ ; colour scales are in nm; (c) Line-scan profile which corresponds to the white line of image (b).

The polymer phase-separation between the F8BT:TFB blends (1:2, 1:3, 1:4) without and with quantum dots is presented in Figures 5.16a, b and c and in Figures 5.16d, e and f, respectively. The comparison between the two systems reveals more clearly that the separation of the polymer blend in two phases: F8BT-rich and TFB-rich, remains similar by adding the quantum dots. More precisely, the two black boxes in Figures 5.16a and d, highlight examples of identical F8BT-rich phase-separated domains in F8BT:TFB 1:2 thin films without and with QDs. However, there are differences concerning the lateral and the vertical size of the polymer phase-separated domains and we should mention that in the case of the films with the quantum dots, the AFM height images exhibited a more blurred picture compared to the thin films without QDs.

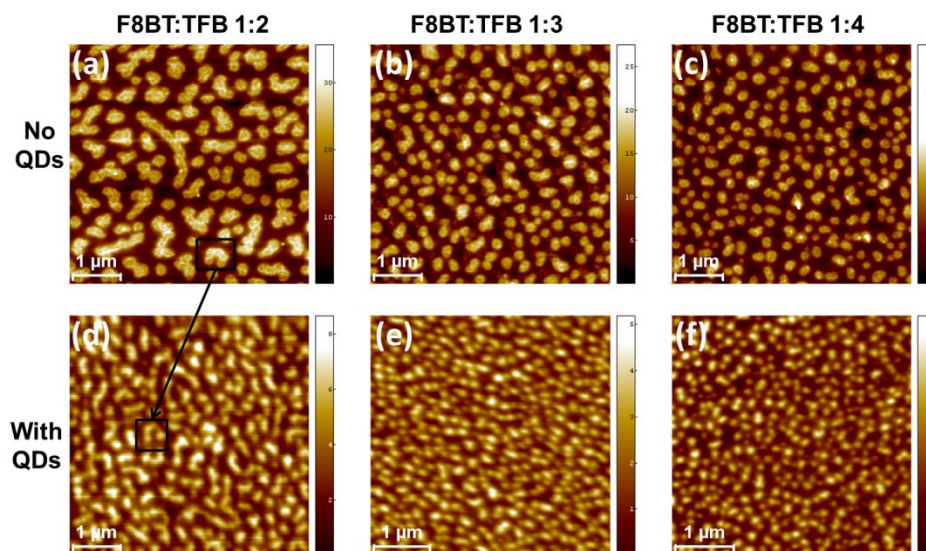


**Figure 5.16** Typical AFM height images of F8BT:TFB thin films on mica with polymer blend ratio 1:2, 1:3 and 1:4 without (a), (b), (c) and with (d), (e), (f) quantum dots respectively. The scan size of the images is approximately  $5 \times 5 \mu\text{m}^2$  and the  $z$ -scale is in nm. The colour scales are  $\sim 25$  nm and  $\sim 5$  nm for the thin films without and with QDs, respectively. The black boxes in (a) and (d), highlight the similar phase-separated domains formed in thin films without QDs and with QDs.

In the following graphs of Figure 5.17, the lateral and vertical difference of the phase-separated domains between the F8BT:TFB thin films without QDs and with QDs are presented, calculated by post-processing AFM imaging. The percentage of the islands coverage on the film surface decreased with the increase of the TFB part both for the systems with and without QDs in the same way. However, the thin films with QDs exhibited lower surface coverage in all cases than the thin films without QDs; the difference is in the range of  $\sim 15 - 20\%$  (Figure 5.17a).

Furthermore, the lateral size of the island-like phase-separated F8BT-rich domains is presented in Figure 5.17b. In the case of the thin films with quantum dots, the diameter of the islands decreases from  $\sim 260$  nm in the case of 1:2 polymer blend to  $\sim 160$  nm in the case of 1:3 polymer blend and to  $\sim 120$  nm in the case of 1:4 polymer blend. These values are lower than the values in the system without the QDs. We should note that the exact diameter of the islands is difficult to calculate from the AFM, due to the tip-sample convolution. However, we are able to obtain reliable results concerning the tendency of the domain diameter to decrease by increasing the TFB fraction and that the domains from the QD-system are smaller than in the non QD-system.

Finally, the vertical size (height) of the island-like domains for the QD-system versus the polymer blend ratio is plotted in Figure 5.17c. The height of the domains was significantly smaller (approximately one order of magnitude) than the height of the domains in non QD-system. The height of the islands decreased with increasing the fraction of the TFB part in the polymer blend ( $\sim 3$  nm,  $\sim 2$  nm and  $\sim 1.5$  nm for

1:2, 1:3 and 1:4, respectively). We should note that the height of the domains is calculated through the post-processing software from the height difference between the bottom area and the edge of the top surface of the islands, meaning that the rough surfaces of the isolated islands are not taken into account and that the bottom area might not be perfectly flat.

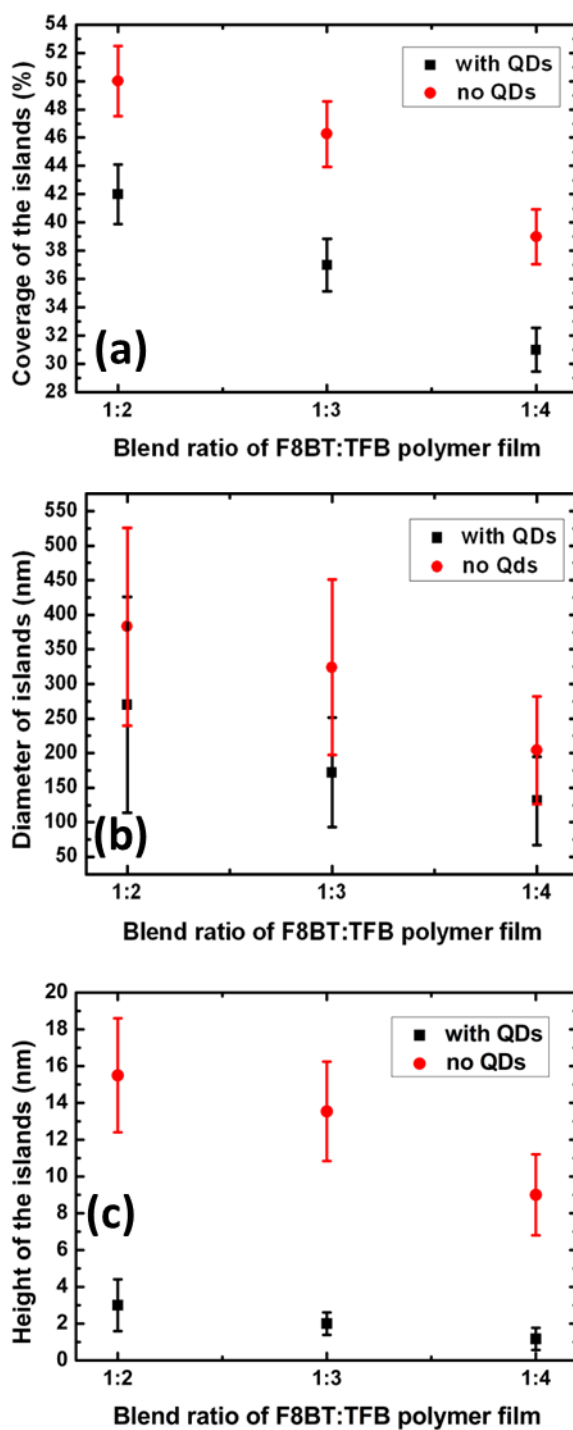


Figure 5.17 (a) Coverage of the islands, (b) diameter of the islands and (c) the height of the islands formed in the F8BT:TFB thin films versus the by weight F8BT:TFB polymer blend ratio; the red circles correspond to the thin films without QDs studied in the previous chapter, the black squares correspond to the thin films with QDs.

#### 5.4.4 CdSe Quantum Dots Detection in F8BT:TFB thin films

In the following part of the present chapter, we used adhesion AFM, phase imaging AFM, TEM and fluorescence microscopy, to locate the quantum dots on/in the film. From the height AFM imaging we have already observed that several clusters were formed at the top surface of the thin films. Generally, these clusters are smaller in the case of 1:1 thin films and become larger in 1:2, 1:3 and 1:4 films.

##### 5.4.4.1 Quantitative Analysis of Quantum Dots using AFM techniques

The QI<sup>TM</sup> (quantitative imaging) mode atomic force microscope technique is applied on F8BT:TFB with QD thin films in order to determine quantitatively the different domains at the top of the film. Given the significant difference in the molecular architecture/composition between the inorganic quantum dots and the conjugated polymers, physical and mechanical properties such as density and stiffness are unique for each compound and will affect the adhesive properties. To this end, we performed QI<sup>TM</sup> AFM mapping of F8BT:TFB 1:1 and F8BT:TFB 1:2 thin films, focusing on the phase-separated polymer domains and the bulk structures on top. The cantilever we used, which is made of *n*-type silicon, was calibrated (via the thermal method) and the spring constant was 0.283 N/m. Force – distance curves were obtained from every domain and some representative ones are presented in the graph of Figure 5.18. An example of a force – distance curve focused on the bulk top structure is presented in the black curve of the graph in Figure 5.18. The maximum force during the retraction curve provides the adhesion between the material in the bulk area and the tip and is  $\approx 6.5 \pm 1$  nN. Furthermore, the force of adhesion of the

higher lying domains in the polymer phase-separated area (polymer network in 1:1 polymer blends and island structures in 1:2 polymer blends) is  $\approx 10 \pm 2$  nN (red dashed curve in the graph of Figure 5.18). Finally, the force – distance curve in the lower lying polymer domains (wells in 1:1 polymer blends and lower polymer matrix in 1:2 polymer blends) revealed that the force of adhesion is  $\approx 13 \pm 2$  nN (blue dotted curve in the graph of Figure 5.18).

We already know from the previous chapter that the lower lying polymer domains in F8BT:TFB films are TFB-rich, while the higher domains are F8BT-rich. As a result the force values of the F8BT and the TFB parts are expected to be  $\approx 10 \pm 2$  nN and  $\approx 13 \pm 2$  nN, respectively. The similar surface tension values of the blends (F8BT  $\sim 40\text{--}45$  mJ/m<sup>2</sup> TFB  $\sim 35\text{--}40$  mJ/m<sup>2</sup>) do not provide an obvious reason for the adhesion difference. In addition, both polymers, which are well below their glass transition temperature (F8BT  $\sim 99$  °C, TFB  $\sim 156$  °C [44]) are expected to exhibit similar low adhesion properties. However, we speculate that the TFB polymer part exhibits higher adhesion than the F8BT due to the water or solvent molecules which might be trapped inside the TFB domains. TFB polymer exhibits higher solubility in *p*-xylene than the F8BT polymer, so it is more likely that there would be more molecules of solvent trapped inside TFB part even after spin coating (this might be the reason behind the soft behaviour of the TFB film presented in the previous chapter and appendix B). The bulk structure on the top surface of the films exhibits lower adhesive force than the force of the polymer blends pointing to the conclusion that these aggregates does not consist of any of the polymers but of CdSe quantum

dots. This type of quantitative information for the quantum dots provides a very important tool to identify the nanoparticles across the total thin film area.

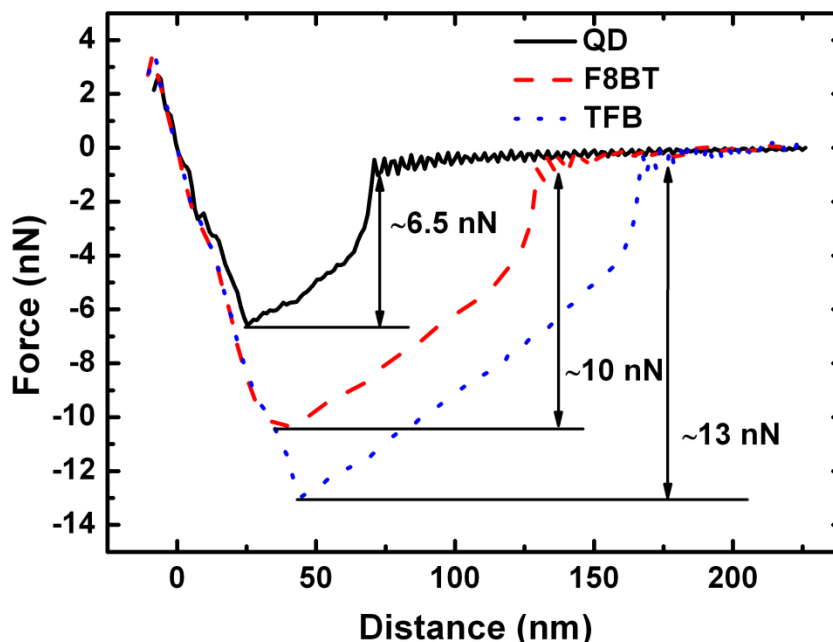


**Figure 5.18** Representative force-distance curves of CdSe quantum dots (black curve), F8BT (red dashed curve) and TFB (blue dotted curve), taken from the top surface of F8BT:TFB with 1:1 and 1:2 polymer blend ratio mixed with QDs thin films. The curves refer to the retraction of the tip during QI™ AFM mapping. The x-axis refers to the piezo displacement as measured by the sensor in the AFM head and smoothed. The spring constant of the tip used is 0.2828 N/m.

Figure 5.19 presents an AFM height image (Figure 5.19a) and the corresponding adhesion image (Figure 5.19b) of a F8BT:TFB 1:1 blend ratio thin film mixed with quantum dots. The different domains are shown using black arrows in the height image. We observe from both images that within the F8BT-rich higher lying phase, there are small CdSe QD aggregates. We cannot exclude the possibility of single QDs within this layer; however the small size of the QDs and the roughness of the polymer layer do not permit a clear observation of single QDs. Such small aggregates are not present in the lower lying TFB-rich domains (bright areas in the



adhesion image). Furthermore, there are areas where there is some segregation of QDs on top of the whole polymer layer. This is even more prominent in the case of F8BT:TFB 1:2 (with QDs) as shown in Figure 5.20 presenting the height (Figure 5.20a) and the corresponding adhesion (Figure 5.20b) AFM image.

Two valuable pieces of information are obtained from the height and the corresponding adhesion images (Figures 5.19 and 5.20) and force values of this system (Figure 5.18). The first is that there are quantum dots that are located in the form of either big or smaller aggregates across the film surface. The second valuable information is that we have not observed any CdSe quantum dots on the TFB – rich domains. The QDs have the tendency to spread on/in the F8BT-rich layer (F8BT:TFB 1:1), and when there is no continuous F8BT-layer available, they tend to form large aggregates (F8BT:TFB 1:2) at the top surface instead. These observations are in agreement with the comparison of the phase images of F8BT-QD and TFB-QD thin films presented in Figure 5.13. In the case of the TFB-QD thin film we have observed that the QDs and the TFB polymer have separated in two lateral alternate phases parallel to the substrate, meaning that the QDs do not find it favourable to cover the TFB; the opposite happens in the case of F8BT film.

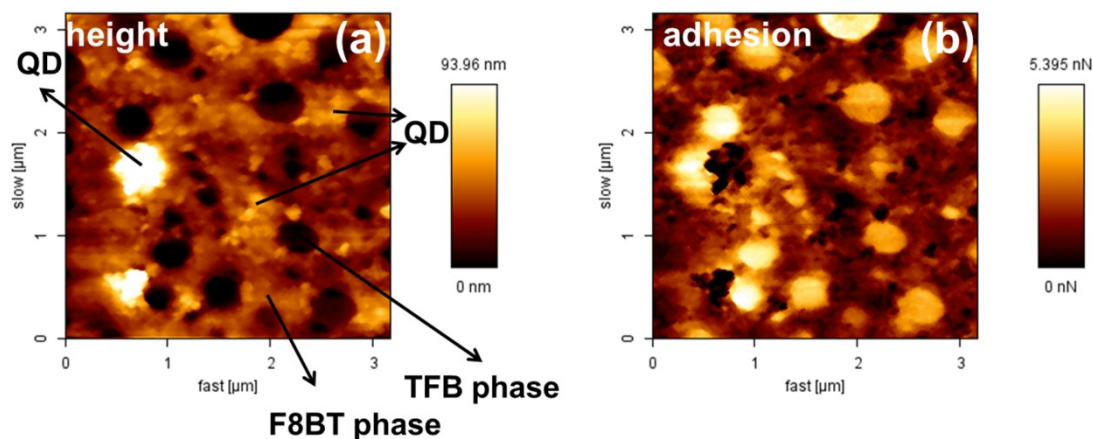


Figure 5.19 (a) Height and the corresponding (b) adhesion mapping of F8BT:TFB 1:1 mixed with QDs thin film. In height image, the dark well-like structures correspond to the TFB-rich domains, while the brown homogeneous matrix is F8BT-rich. The bright domains at the top correspond to the quantum dots. In the adhesion image the dark (low adhesion) correspond to QDs, the brown areas to F8BT-rich domains and the bright areas to TFB-rich domains.

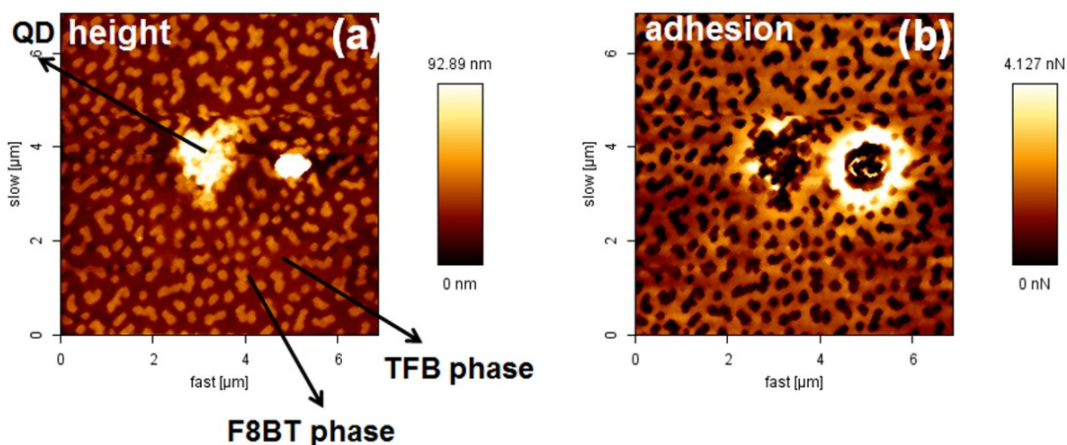
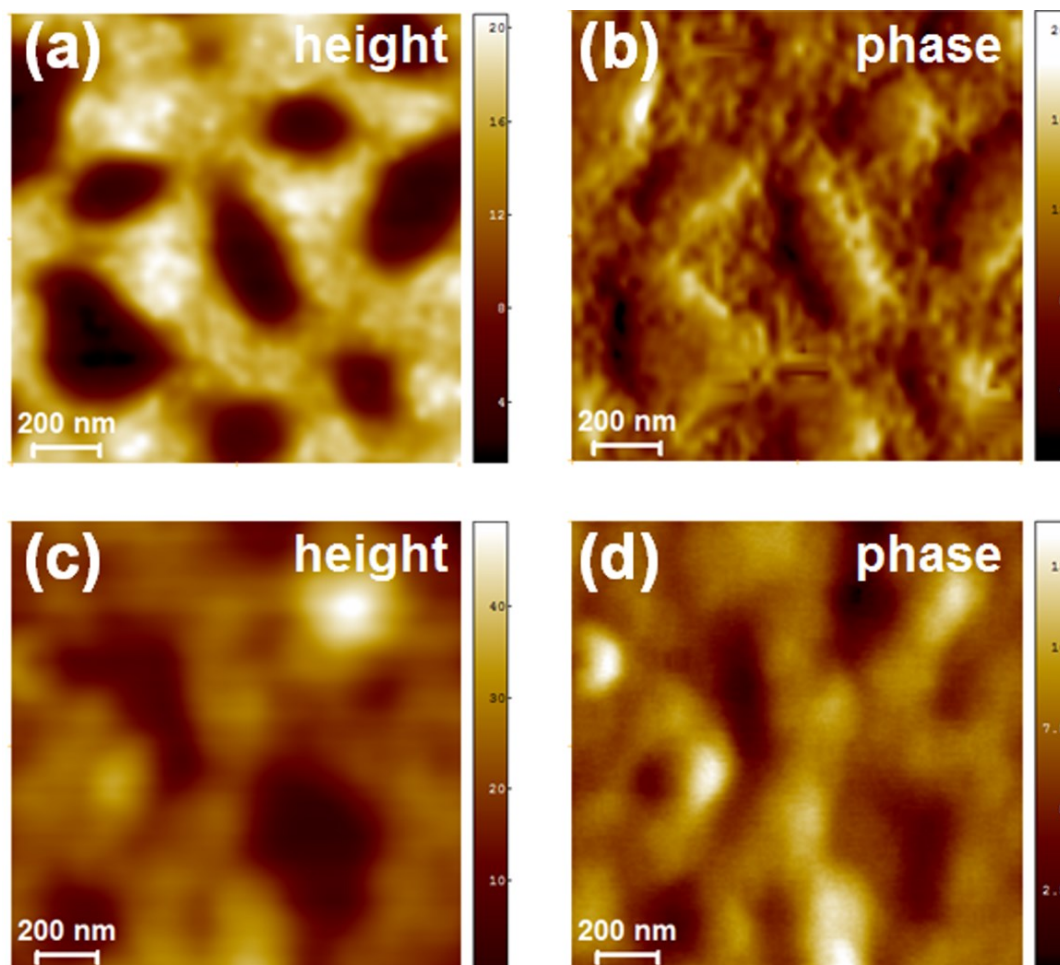


Figure 5.20 (a) Height and the corresponding (b) adhesion mapping of F8BT:TFB 1:2 mixed with QDs thin film. In height image, the dark brown lower lying layer corresponds to the TFB-rich domain, while the lighter brown island-like structures are F8BT-rich. The bright domains at the top correspond to the quantum dots. In the adhesion image the dark (low adhesion) correspond to QDs, the less dark areas to F8BT-rich domains and the bright areas to TFB-rich domains.

#### **5.4.4.2 Comparison between Tapping Mode AFM phase imaging of F8BT:TFB thin films without Quantum Dots and F8BT:TFB thin films with Quantum Dots.**

In the previous part, we confirmed that it is more favourable for the CdSe quantum dots to segregate in F8BT-rich areas and no QDs were observed in TFB-rich areas. Herein we focus on the difference in the phase contrast in small scan-size areas between thin films without QDs and with QDs. The scanning areas chosen are away from the QD aggregates to investigate how the film characteristics differ from the polymer-only thin films in the nanoscale. Through the phase imaging, we expect that the inorganic nanoparticles would exhibit different phase contrast compared with the phase contrast of the polymer blends.

Figure 5.21 presents AFM height (Figures 5.21a, c) and phase (Figures 5.21b, d) images of F8BT:TFB 1:1 thin films without quantum dots (Figure 5.21a, b) and with quantum dots (Figures 5.21c, d). In the case of the thin film without QDs, two clear phases are formed, one TFB-rich and the other F8BT-rich but as already discussed in the previous chapter there is some intermixing at the free interface in particular on top of the high lying F8BT-rich domains. However, in the case of the thin film with QDs, the ‘grainy’ structure is suppressed indicating that the presence of the quantum dots (not probed separately in these images) have hindered the formation of the capping layer.



**Figure 5.21** Typical AFM height (a) (c) and phase images (b) (d) of F8BT:TFB 1:1 thin films without quantum dots (a), (b) and with quantum dots (c), (d). The z-scales are in nm for the height images and in degrees of the phase images.

Furthermore, Figure 5.22 presents AFM height and phase images of F8BT:TFB 1:4 thin films without QDs (Figures 5.22a, b) and with QDs (Figures 5.22c, d). As extensively investigated in the previous chapter, no QD thin films of F8BT/TFB blend ratio  $< 1$  exhibit island-like phases surrounded by a homogeneous layer of the other phase. The island-like structures are F8BT-rich but they have a crater-like shape and they are ‘filled’ with a TFB capping layer. On the contrary, the height images of the QD thin films the islands have no crater appearance. As shown also in

the phase image in Figure 5.22d, the F8BT-rich areas do not exhibit a crater-like structure and no TFB areas (capping layer/grainy structure) are present inside the islands. A more homogeneous F8BT phase is formed instead. However, it has to be noted that the bright appearance of F8BT islands can be attributed to the presence of *the quantum dots within the F8BT areas*.

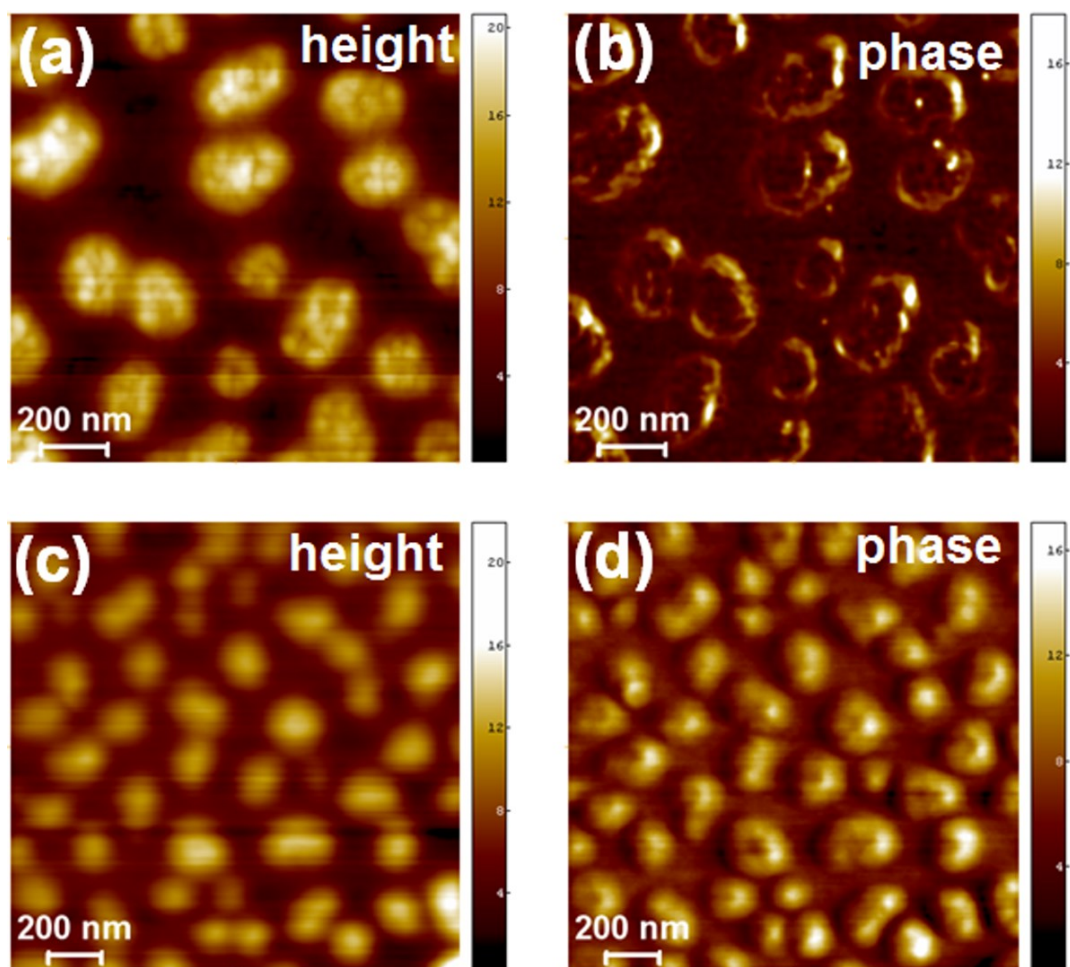


Figure 5.22 Typical AFM height (a) (c) and phase images (b) (d) of F8BT:TFB 1:4 thin films without quantum dots (a), (b) and with quantum dots (c), (d). The z-scales are in nm for the height images and in degrees of the phase images.

Thus, we could speculate from the surface analysis of these domains that by adding quantum dots in the system, we can achieve better phase-separation between

the blends. A reason why smaller F8BT phases were formed might be attributed to the kinetics of the phase separation of the F8BT:TFB polymer blend. Studies on polymer blend-NP systems, concluded that the polymer which has high affinity with the nanoparticles exhibit high viscosity, resulting in the hindering of the phase growth [41, 45]. Furthermore, Ginzburg *et al.* [46] concluded that the nanoparticles hamper interface motion, slowing down the domain growth. In addition, Tang and *co-worker* [47] stated that the nanoparticles inhibit the shape relaxation of the domains due to the excluded volume. Tanaka *et al.* [48] have also reported that the NPs can significantly affect the coarsening dynamics of the system. They stated that the NPs could ‘disturb’ the polymer flow inside the domains causing friction and slower domain motion. Theoretical studies based on the nanoparticle-polymer mixtures reported the existence of distinct phase separated domains in the early stages of thin-film formation [49,50] and a subsequent slowing of the domain growth in the later stages [51,52]. Later experimental studies [41,53], established the significant slowing of the phase separated domains, when nanoparticles are added in a polymer mixture. Thus, in our case, an effective increase of the F8BT viscosity due to the effect of the nanoparticles could also be the reason for the hindering the growth of phase separated domains and could also lead to less intermixing and purer (but smaller in size) phase-separated F8BT domains.

Although, many experimental and computational studies focused on the kinetics of the formation of polymer-nanoparticle mixture composites have been published, little has been published on the thermodynamics (experimental or theoretical) related to the phase separation of these mixtures [52]. Therefore, there is

little knowledge on the effect of the nanoparticle size, volume fraction or composition on the overall phase separation. Ginzburg [54] and He *et al.* [55] used thermodynamic theory to reveal the effect of the nanoparticles on the miscibility of a polymer blend system of two homopolymers. They reported that decreasing the size of the nanoparticles, an immiscible phase-separated system can be tuned into a thermodynamically miscible single-phase system. They concluded that by varying the size of the nanoparticles, one can control the phase-separation behaviour. However, we should point out that these studies were performed without the use of a solvent in the system (ternary system), plus they used homopolymers as parts of the blend in which physical parameters such as the  $\chi$  (Flory-Huggins interaction parameter) is easier to be found, compared with the more complicated copolymers such as the F8BT or the TFB. Furthermore, our experimental protocol (spin-coating) ‘suffers’ from kinetic dominated phenomena (i.e. we could be far from equilibrium).

#### **5.4.4.3 Use of Transmission Electron Microscopy to Detect the Quantum Dots.**

As we have seen the direct detection of the quantum dots with AFM is not easy and straightforward. Furthermore, with AFM we confine ourselves to the study of the free interface alone. Owing to the significant difference between the inorganic quantum dot and the organic conjugated polymer densities, we used mass-thickness transmission electron microscopy (TEM) to detect the quantum dots in the film as their exact position will have consequences for the performance of devices. Indeed, in the TEM micrograph of Figure 5.23, the segregated quantum dots are presented in black colour. Apart from the big segregated QD domain, the F8BT:TFB 1:4 phase-



separated domains are also clearly seen. The contrast is better than in the corresponding Figure of previous chapter for the same film without QDs indicating the presence of QDs in the F8BT domains. The red squares in the TEM image present three F8BT domains of particular interest.

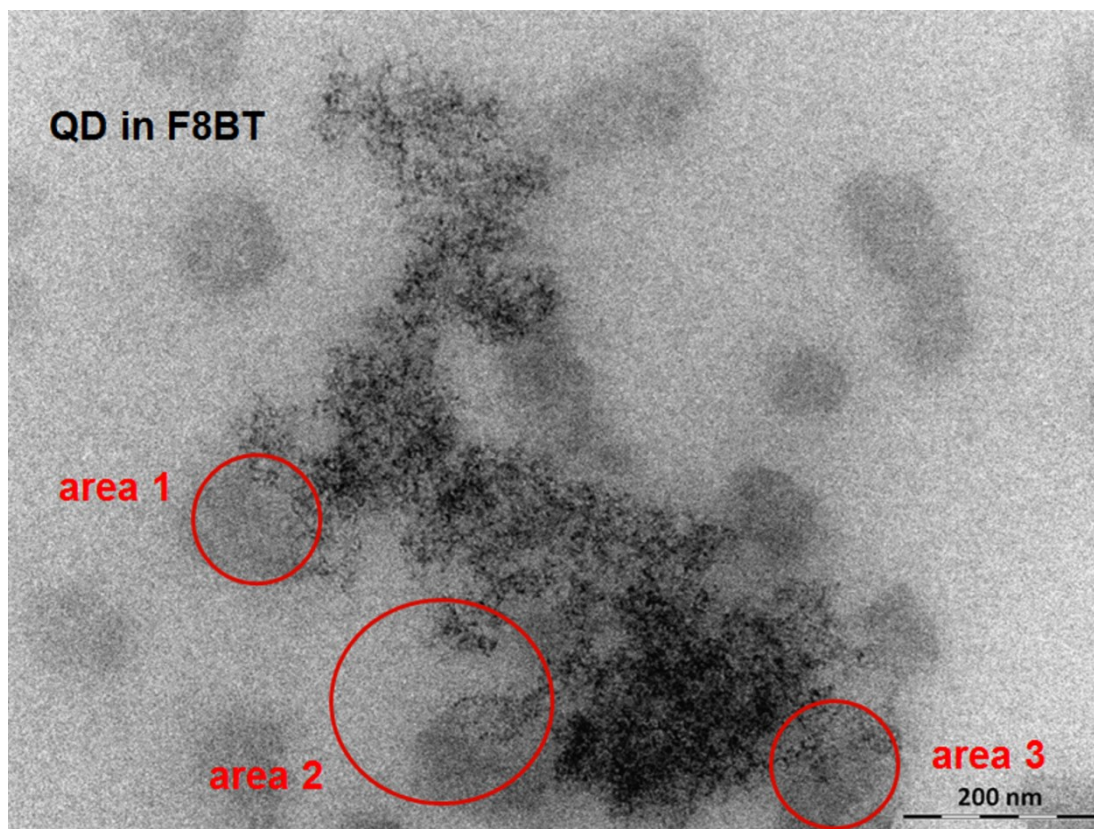


**Figure 5.23** Mass-thickness contrast TEM image of F8BT:TFB 1:4 thin film with quantum dots. The phase-separated polymer blend domains (clear contrast) and the segregated QDs (dark cloud) are presented in the image. Three different areas in the interface of F8BT and TFB domains were studied for QD detection. The TEM experiment was performed by Marco Bigatti in the School of Physics, the University of Glasgow, Glasgow, UK.

The three different areas highlighted in red circles in Figure 5.23, are presented separately in TEM micrographs of Figures 5.24a, b and c. The rectangle shapes in every TEM image (Figures 5.24a, b and c) highlight isolated quantum dots which lie on the F8BT:TFB interface. According to the literature, these quantum dots would be



functional and enhance the electron mobility in LED and solar cell devices [3], while the QD-rich clusters are not considered to be functional. We note that intensity profiles (insets in Figures 5.24a, b and c) taken across the rectangular shapes identify quantitatively isolated and not segregated quantum dots on the F8BT domains but close to the F8BT-TFB interface. Given the significant higher density of the inorganic quantum dots compared with the polymer blends, lower intensity (less electron diffraction) compared with the polymers is expected at the position of the QD. The intensity profiles revealed that in a lateral distance of 2 – 3 nm the intensity drops significantly. From the CdSe QD supplier we know that the size of the dots is  $\sim 2.1$  nm (Table 5.2). As a result we undoubtedly conclude that isolated dots lie on the F8BT domains and preferentially near the interface with the other polymer. It was almost impossible or very difficult to obtain this piece of information with the use of AFM techniques. AFM studies the free interface which might not be an accurate representation of what is happening inside the film. Furthermore, very small ( $\sim 1 - 10$  nm) lateral size domains within a relatively rough film surface suffer from tip-sample convolution effects.

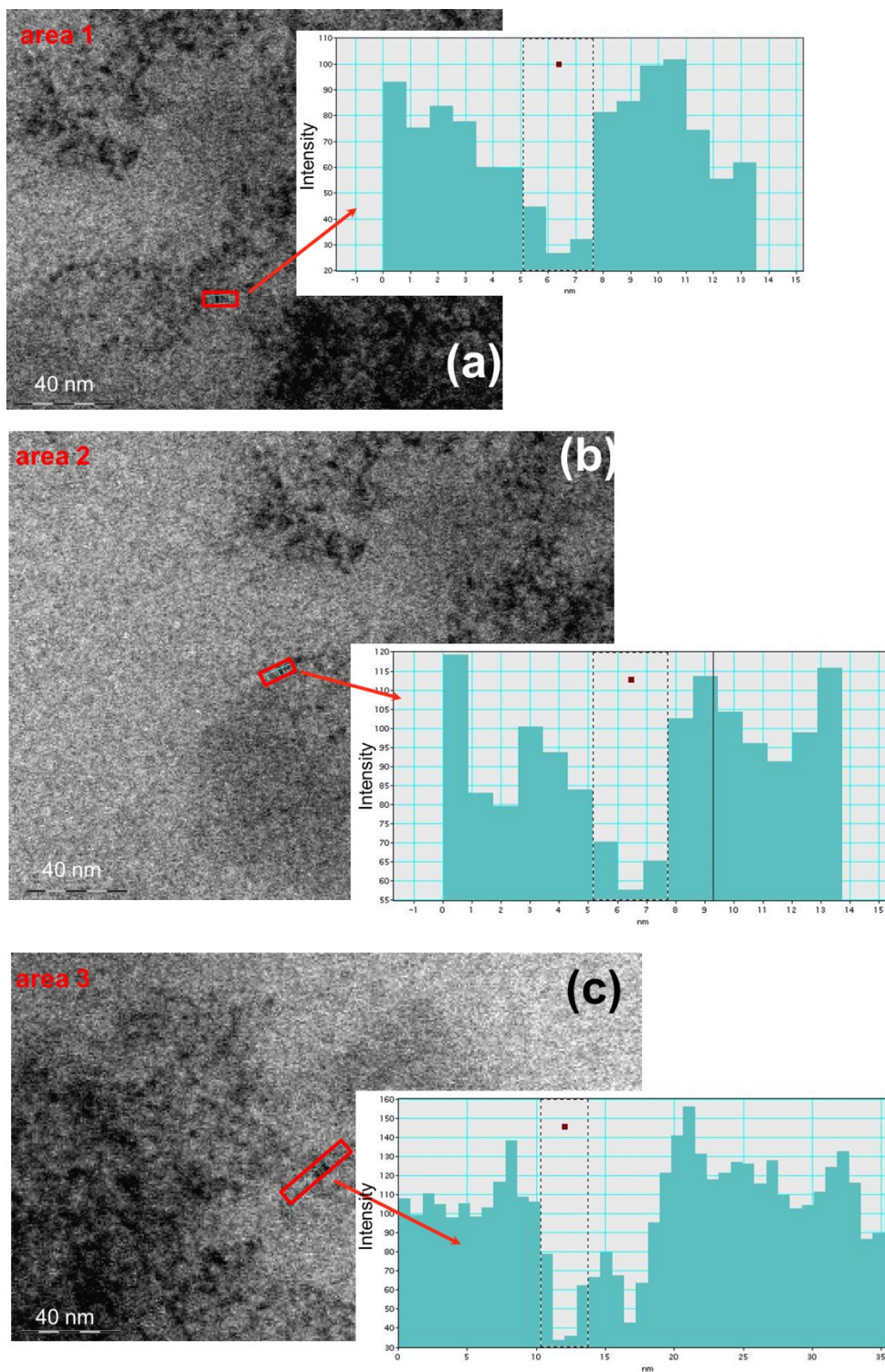


Figure 5.24 (a), (b), (c) Mass-thickness TEM images of F8BT:TFB 1:4 mixed with QDs thin films. Inside the red circles, located near the interface between the F8BT and TFB phases green dashed rectangular shapes contain individual QDs. Intensity profiles across the dash rectangular shapes are also shown.

#### 5.4.4.4 Supplementary Measurements. Optical Fluorescence Imaging and Bright-Field TEM.

Figure 5.25 presents optical microscopy with fitted fluorescence camera images of F8BT:TFB 1:1 without QDs (Figure 5.25a) and with QDs (Figure 5.25b). The fluorescence camera is adjusted to the fluorescence emission of the quantum dots (see Table 5.2). The sample with QDs looks much brighter throughout the sample. The brighter spots of the image in Figure 5.25b correspond to areas where the quantum dots are denser; due to the lateral resolution we mainly observe the denser quantum dot aggregates (not the polymer-related phase separation areas which are at the submicrometre scale).

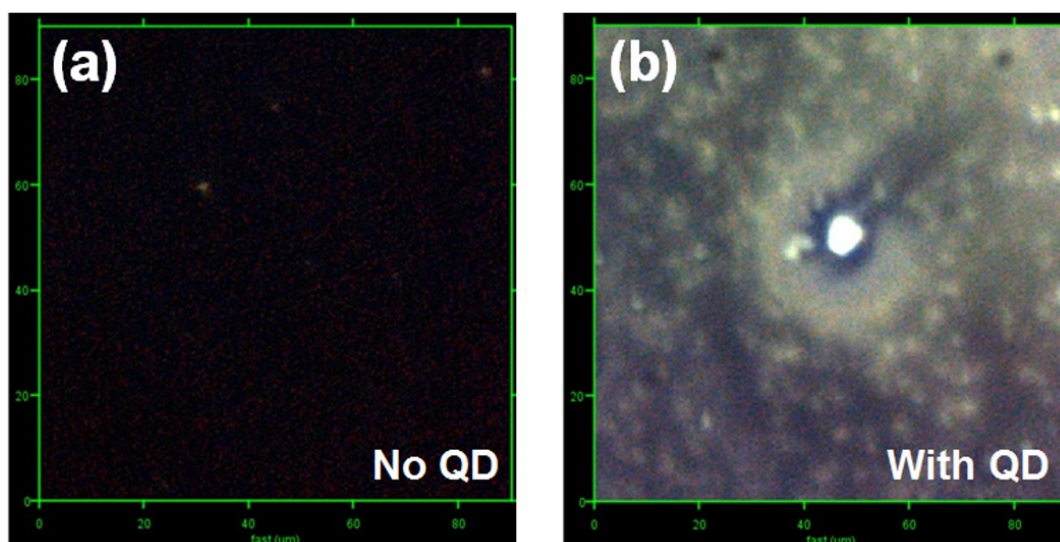
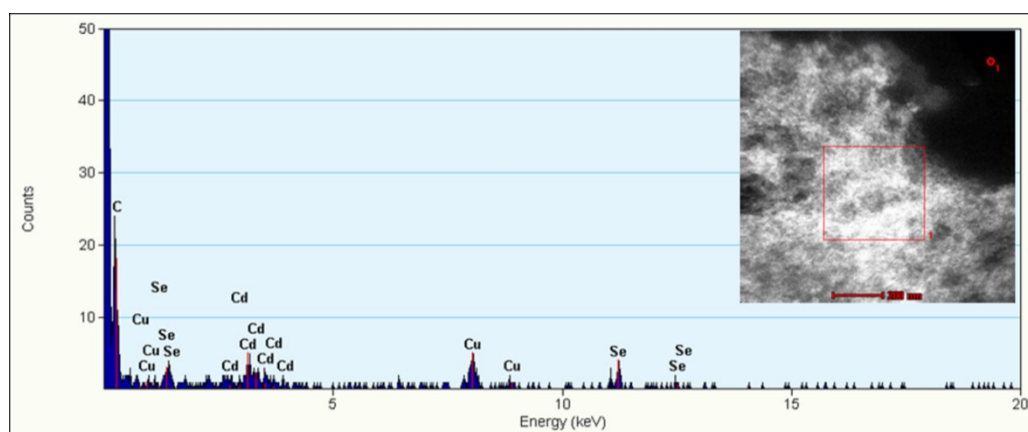


Figure 5.25 F8BT:TFB 1:1 without QDs (a) and with QDs (b) images from optical microscope fitted on the JPK AFM (the AFM images were taken in this sample), featuring a fluorescence camera with the appropriate to CdSe QD ( $\sim 480\text{nm}$ ) fluorescence filters.

Apart from mass-thickness TEM technique, we also applied bright-field TEM to perform element analysis in the big aggregates at the top surface of the film (Figure 5.26). Energy-dispersive *X*-ray spectroscopy (EDX) applied in the bright-

field TEM images, revealed the existence of high concentration in Cd and Se elements at the big aggregates (the data generated by EDX analysis consist of spectra showing peaks corresponding to the elements making up the true composition of a sample being analysed). This verifies further our conclusion that the big clusters at the top surface of the film are QD-rich. Copper (Cu) and carbon (C) elements were also identified due to the TEM copper grid and the polymer blends that lie beneath the aggregates, respectively.



**Figure 5.26** Energy-dispersive X-ray spectroscopy (EDX) used for elemental analysis within the area of the red box at the inset bright-field TEM image. The studied area is focused on the quantum dot clusters at the film surface of F8BT:TFB 1:4 with QD thin films. Cd, Se spikes correspond to the quantum dots, C corresponds to the polymer blends and Cu corresponds to the TEM copper grid.

## 5.5 Conclusions

In this chapter, the thin film morphology of polyfluorene F8BT:TFB blends mixed with inorganic CdSe quantum dots (QD) was investigated for the first time and compared with the corresponding morphology of F8BT:TFB films. We prepared thin films of F8BT:TFB polymer blends (with blend ratio 1:1, 1:2, 1:3, 1:4) (PB) mixed with QDs, in which the weight ratio varied from 28:5 to 14:5 and 14:10. Thin

films of CdSe, F8BT and TFB – only were also prepared. We used AFM, TEM and optical microscopy techniques to study how the quantum dots have affected the phase-separation of the polyfluorenes, as well as to accurately detect the QDs on the film surface and within the film.

We found that in PB:QD thin films, the clear phase-separated domains formed by the polymer blend and studied in the previous chapter, exist only when we mix the polymer blend and the quantum dots in a weight ratio of 28:5. Although the phase-separated domains were present, the size (diameter, height) of the phases was found to be significantly smaller. We attributed this to the higher effective viscosity of the polymer which favourably interacts with the quantum dots, in accordance with earlier similar studies on polymer blend-nanoparticle systems [41,42]. The only exception is the height of the higher-lying F8BT-rich layer in the F8BT:TFB with 1:1 blend ratio. This was found that it has almost the same height of the F8BT-rich layer from 1:1 without QDs thin films.

Force-distance curves and adhesion mapping revealed the existence of two morphology trends. One in the case of thin films with QDs and 1:1 F8BT:TFB blend (F8BT-rich layer formed on the top surface) and the other in the case of thin films with QDs and the weight fraction is  $F8BT/TFB < 1$  (F8BT island-like structures were formed surrounded by a TFB layer). In the first case the quantum dots were spread in the F8BT-rich layer only and in a few cases they formed small aggregates, while in the second case the QDs formed larger aggregates. From these we concluded that the quantum dots find it more favourable to spread on top of an

F8BT-rich layer, while in the case where there is no such layer (weight fraction is  $F8BT/TFB < 1$ ) the QDs prefer to segregate into large structures at the top surface (without of course excluding the presence of isolated QDs within F8BT areas in all cases). The fact that the quantum dots do not prefer the TFB areas is confirmed also by phase and height AFM imaging of TFB-only thin films, which exhibited lateral phase-separation between the QDs and the TFB, while the F8BT-only thin films indicated mixing between F8BT and QDs.

AFM phase imaging revealed that the QDs suppress the formation of the capping layer and enhance the polymer blend phase separation leading to purer domains.

Mass-thickness and bright-field TEM imaging of thin films with QD/PB were also performed to investigate the position of the CdSe quantum dots within the bulk of the film. The clear contrast between the polymer phases confirms the preferential segregation of QDs in the F8BT domains. Furthermore, intensity profiles in different areas of F8BT domains have shown that single quantum dots were lying at the interface of the F8BT polymer parts. These quantum dots are of significance as they are expected to contribute to the functionality of the thin film applied on a device.

Finally, we should highlight the significance of our findings as the main conclusion is that the high electron transporting inorganic quantum dot prefers the surface of the low electron transporting organic F8BT to the surface of TFB. This intriguing conclusion combined with the straight forward mixing process provides a useful strategy to produce LEDs and PV cells with better efficiency compared to the

polymer only devices. However studies concentrated on improving the solubility of the quantum dots in the polymer blend solution have to be performed in the future, in order to avoid the large clustering of the quantum dots which do not contribute favourably to the performance of the devices.

## 5.6 References

1. MacDiarmid AG. *Current Applied Physics* 2001;1(4-5):269-279.
2. Moons E. *Journal of Physics: Condensed Matter* 2002;14(47):12235.
3. Cloutier SG. Hybrid Polyfluorene-Based Optoelectronic Devices. In: Fadhali M, editor. *Advanced Photonic Sciences*. Rijeka, Croatia: InTech, 2012. pp. 177.
4. Tang CW. *Applied Physics Letters* 1986;48(2):183-185.
5. Granstrom M, Petritsch K, Arias AC, Lux A, Andersson MR, and Friend RH. *Nature* 1998;395(6699):257-260.
6. Schwartz BJ. *Annual Review of Physical Chemistry* 2003;54(1):141-172.
7. Shaheen SE, Brabec CJ, Sariciftci NS, Padinger F, Fromherz T, and Hummelen JC. *Applied Physics Letters* 2001;78(6):841-843.
8. Green MA, Emery K, King DL, Igari S, and Warta W. *Progress in Photovoltaics* 2001;9(4):287-293.
9. Huynh WU, Dittmer JJ, and Alivisatos AP. *Science (New York, N.Y.)* 2002;295(5564):2425-2427.
10. Bozano L, Carter SA, Scott JC, Malliaras GG, and Brock PJ. *Applied Physics Letters* 1999;74(8):1132-1134.
11. Yu G, Gao J, Hummelen JC, Wudl F, and Heeger AJ. *Science* 1995;270(5243):1789-1791.



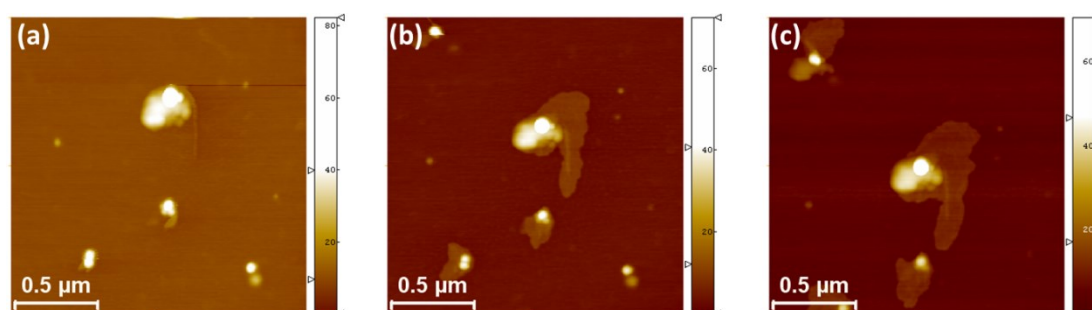
12. Roman LS, Andersson MR, Yohannes T, and Inganás O. *Advanced Materials* 1997;9(15):1164-1168.
13. Dittmer JJ, Marseglia EA, and Friend RH. *Advanced Materials* 2000;12(17):1270-1274.
14. Tsutsui T. *Nature* 2002;420(6917):752-755.
15. Era M, Hayashi S, Tsutsui T, and Saito S. *J. Chem. Soc. Chem. Commun.* 1985:557-558.
16. Era M, Morimoto S, Tsutsui T, and Saito S. *Appl. Phys. Lett.* 1994;65:676-678.
17. Greenham NC, Peng X, and Alivisatos AP. *Physical Review B* 1996;54(24):17628-17637.
18. Ginger DS and Greenham NC. *Physical Review B* 1999;59(16):10622-10629.
19. Rehm JM, McLendon GL, Nagasawa Y, Yoshihara K, Moser J, and Grätzel M. *The Journal of Physical Chemistry* 1996;100(23):9577-9578.
20. Coe S, Woo WK, Bawendi M, and Bulovic V. *Nature* 2002;420(6917):800-803.
21. Peng X, Manna L, Yang W, Wickham J, Scher E, Kadavanich A, and Alivisatos AP. *Nature* 2000;404(6773):59-61.
22. Kharlampieva E, Kozlovskaya V, Zavgorodnya O, Lilly GD, Kotov NA, and Tsukruk VV. *Soft Matter* 2010;6(4):800-807.

23. Kozlovskaya V, Kharlampieva E, Khanal BP, Manna P, Zubarev ER, and Tsukruk VV. *Chemistry of Materials* 2008;20(24):7474-7485.
24. Goodman MD, Xu J, Wang J, and Lin Z. *Chemistry of Materials* 2009;21(5):934-938.
25. Gur I, Fromer NA, Geier ML, and Alivisatos AP. *Science* 2005;310(5747):462-465.
26. Coe S, Woo WK, Bawendi M, and Bulovic V. *Nature* 2002;420:800-803.
27. Medintz IL, Uyeda HT, Goldman ER, and Mattoussi H. *Nat Mater* 2005;4(6):435-446.
28. Saunders BR and Turner ML. *Advances in Colloid and Interface Science* 2008;138(1):1-23.
29. Rossetti R, Nakahara S, and Brus LE. *The Journal of Chemical Physics* 1983;79(2):1086-1088.
30. Jpailee. Exciton energy levels. 2011.
31. Kim Y, Choulis SA, Nelson J, Bradley DDC, Cook S, and Durrant JR. *Applied Physics Letters* 2005;86(6):063502-063503.
32. Ma W, Yang C, Gong X, Lee K, and Heeger AJ. *Advanced Functional Materials* 2005;15(10):1617-1622.
33. Tuinier R, Smith P, A., Poon W, C. K., Egelhaaf S, U., Aarts D, G. A. L., Lekkerkerker H, N. W., and Fler G, J. *EPL* 2008;82(6):68002.

34. McNeill CR, Watts B, Thomsen L, Belcher WJ, Greenham NC, Dastoor PC, and Ade H. *Macromolecules* 2009;42(9):3347-3352.
35. Qu L and Peng X. *Journal of the American Chemical Society* 2002;124(9):2049-2055.
36. Yu WW, Qu L, Guo W, and Peng X. *Chemistry of Materials* 2003;15(14):2854-2860.
37. Glynos E, Chremos A, Petekidis G, Camp PJ, and Koutsos V. *Macromolecules* 2007;40(19):6947-6958.
38. Wang P, Abrusci A, Wong HMP, Svensson M, Andersson MR, and Greenham NC. *Nano Letters* 2006;6(8):1789-1793.
39. Hampton MJ, Templeton JL, and DeSimone JM. *Langmuir* 2010;26(5):3012-3015.
40. Tan Z, Zhang F, Zhu T, Xu J, Wang AY, Dixon JD, Li L, Zhang Q, Mohny SE, and Ruzyllo J. *Nano Letters* 2007;7(12):3803-3807.
41. Chung H-J, Taubert A, Deshmukh RD, and Composto RJ. *EPL (Europhysics Letters)* 2004;68(2):219.
42. Gam S, Corlu A, Chung H-J, Ohno K, Hore MJA, and Composto RJ. *Soft Matter* 2011;7(16):7262-7268.
43. Araki T and Tanaka H. *Physical Review E* 2006;73(6):061506.
44. Ramsdale CM and Greenham NC. *Journal of Physics D: Applied Physics* 2003;36(4):L29.

45. Elias L, Fenouillot F, Majeste JC, and Cassagnau P. *Polymer* 2007;48(20):6029-6040.
46. Ginzburg VV, Qiu F, Paniconi M, Peng G, Jasnow D, and Balazs AC. *Physical Review Letters* 1999;82(20):4026-4029.
47. Tang Y-l and Ma Y-q. *The Journal of Chemical Physics* 2002;116(17):7719-7723.
48. Tanaka H, Lovinger AJ, and Davis DD. *Physical Review Letters* 1994;72(16):2581-2584.
49. Lee BP, Douglas JF, and Glotzer SC. *Physical Review E* 1999;60(5):5812-5822.
50. Karim A, Douglas JF, Nisato G, Liu D-W, and Amis EJ. *Macromolecules* 1999;32(18):5917-5924.
51. Balazs AC, Ginzburg VV, Qiu F, Peng G, and Jasnow D. *The Journal of Physical Chemistry B* 2000;104(15):3411-3422.
52. Balazs AC, Emrick T, and Russell TP. *Science* 2006;314(5802):1107-1110.
53. Yurekli K, Karim A, Amis EJ, and Krishnamoorti R. *Macromolecules* 2003;36(19):7256-7267.
54. Ginzburg VV. *Macromolecules* 2005;38(6):2362-2367.
55. He G, Ginzburg VV, and Balazs AC. *Journal of Polymer Science Part B: Polymer Physics* 2006;44(17):2389-2403.

## Chapter 6      General Conclusions and Future Work



(a) (b) (c) AFM images of polystyrene-*b*-poly(*p*-hydroxystyrene-*g*-ethylene oxide) block-graft copolymer,  $f_{\text{PEO}} = 0.96$ , dip-coated (THF solutions) on mica. Images were captured at the same area, every 20 minutes indicating the wetting evolution of the polymer on the hydrophilic mica.

## **6.1 General Conclusions**

### **6.1.1 Diblock Copolymer Nanostructures Self-Assembled on Mica**

In the third chapter of this thesis, the morphology of thin PI-*b*-PEO diblock copolymer films prepared by spin coating, by varying the crystallisable, hydrophilic and biocompatible block (PEO) volume fraction and the concentration of the polymers in aqueous solutions was investigated. Stable ordered nanodomains immediately after spin coating were observed in all cases, not affected by heating/annealing and ageing. This is a useful result as self-assembled, robust structures based on block copolymers and produced by environmentally-friendly processing routes can be important for many applications. For example, exploiting the biocompatibility of the PEO block and the coupling between microphase separation and dewetting in thin films, in combination with the PEO crystallinity, robust patterns with useful biological/biomedical properties [1] can be produced by water-processing alone.

### **6.1.2 Thin Films of Conjugated Polymer Blends**

In the fourth chapter of this thesis, an extensive investigation in the lateral phase separation and structural behaviour in nanoscale of low molecular-weight F8BT:TFB conjugated polymer thin films, with various blend ratios by weight was performed, using AFM and TEM. Conjugated polymer thin films have been proven to be excellent candidates for replacing the conventional semiconductors used in the LED and photovoltaic (PV) devices. It was observed sub-micrometre phase-separated domains in the morphology of 1:1, 1:2, 1:3 and 1:4 weight ratio F8BT:TFB thin films for first time. These detailed investigations on the F8BT:TFB thin films

are expected to be crucial for the determination of the functionality and the efficiency of the devices, as even a small change in the film morphology in the nanoscale could affect the overall performance of the LEDs/solar cells [6].

### **6.1.3 Thin Films of Conjugated Blend-Nanoparticle Composites**

In the fifth chapter of this thesis, the thin film morphology of polyfluorene F8BT:TFB blends mixed with inorganic CdSe quantum dots (QDs) was extensively investigated for the first time and compared with the corresponding morphology of F8BT:TFB films. It was found that smaller (approximately one order of magnitude smaller) polymer phase-separated domains were formed compared with the polymer blend only thin films. It was also observed, using AFM and TEM techniques, that apart from smaller or bigger quantum dot aggregates which were formed on the top of the film, some individual quantum dots were lying on or embedded in the F8BT polymer. Interestingly, some of them were close to the interface with the other polymer (TFB). No quantum dots were observed on the surface or inside the TFB polymer. These intriguing conclusions combined with the straight forward mixing process provides a useful strategy to produce LEDs and PV cells with better efficiency compared to the polymer only devices.

## **6.2 Future Work**

### **6.2.1 Diblock Copolymer Nanostructures Self-Assembled on Mica**

The need of forming more stable and phase-controlled nanostructures for applications in fields such as drug/gene delivery applications requires studies on even more stable polymer systems than the diblocks. Amphiphilic grafted copolymers

with poly(ethylene oxide) being the hydrophilic side chains, were found to be excellent candidates for the production of stable biocompatible nano/micro-patterns [2]. Their advantage lies in the unique behaviour of these copolymers in solubility, surface wetting, blood compatibility, and crystalline structure [2-4]. Thus, the need of producing thin films of PEO-based amphiphilic grafted copolymers and then investigating their nanostructural morphology by high-resolution imaging techniques such the AFM is of paramount importance. A preliminary study is under way (see AFM images in Chapter's 6 front-page page).

### **6.2.2 Thin Films of Conjugated Polymer Blends**

While in LED applications, the F8BT:TFB blends have excellent performance, a study focused on photovoltaic cell applications reported that replacing the TFB polymer with the PFB polymer in the blend (F8BT:PFB) resulted in increased efficiency [7]. Arias and *co-workers'* work [7] concentrated on the phase-separation of F8BT:PFB thin films and investigated how this affects the photovoltaic performance of the films; however, there are many issues to be resolved, e.g. again low molecular weight performance. We are aiming to prepare several F8BT:PFB thin films with the same preparation protocol with F8BT:TFB thin films, in order to obtain the best control of preparing efficient PV cells based on PFB.

### **6.2.3 Thin Films of Conjugated Blend-Nanoparticle Composites**

Studies concentrated on improving the solubility of the quantum dots in the polymer blend solution have to be performed in the future, with the aim of avoiding



the large clustering of the quantum dots which do not contribute favourably to the performance of the devices.

Finally, after the extensive study in the structural morphology of the inorganic/organic films and the important conclusions that relate to the device performance, we aim to initiate collaborations with appropriate groups and perform several optical and electrical measurements.

### 6.3 References

1. Khor HL, Kuan Y, Kukula H, Tamada K, Knoll W, Moeller M, and Hutmacher DW. *Biomacromolecules* 2007;8(5):1530-1540.
2. Xu P, Tang H, Li S, Ren J, Van Kirk E, Murdoch WJ, Radosz M, and Shen Y. *Biomacromolecules* 2004;5(5):1736-1744.
3. Robinson DN and Peppas NA. *Macromolecules* 2002;35(9):3668-3674.
4. Zhang R, Seki A, Ishizone T, and Yokoyama H. *Langmuir* 2008;24(10):5527-5533.
5. Burroughes JH, Bradley DDC, Brown AR, Marks RN, Mackay K, Friend RH, Burns PL, and Holmes AB. *Nature* 1990;347(6293):539-541.
6. Yim K-H, Doherty WJ, Salaneck WR, Murphy CE, Friend RH, and Kim J-S. *Nano Letters* 2010;10(2):385-392.
7. Arias AC, MacKenzie JD, Stevenson R, Halls JJM, Inbasekaran M, Woo EP, Richards D, and Friend RH. *Macromolecules* 2001;34(17):6005-6013.
8. Kim J-S, Ho PKH, Murphy CE, and Friend RH. *Macromolecules* 2004;37(8):2861-2871.
9. Colvin VL, Schlamp MC, and Alivisatos AP. *Nature* 1994;370(6488):354-357.

**Appendices A & B & C**

---

**Appendix A: Further Images and Height Profiles for PI-*b*-PEO, PEO and PI Thin Films.**

**PI-*b*-PEO block copolymer with  $f_{\text{PEO}} = 0.32$ .** In Figure A1 typical AFM images for three different average polymer thicknesses (APT  $\approx 7$  nm, 13 nm and 41 nm) of the diblock copolymer with the lowest volume fraction of PEO are presented. In all cases, the film morphologies are characterized by the growth of structures, on both lateral and vertical direction on mica. In the APT  $\approx 7$  nm film (Figure A1a) we observe the formation of a semi-continuous flat-layer network with several ‘arms’ at the polymer mica interface with a thickness of  $\approx 17$  nm. At the top of this first layer there is a thicker flat-layer network with a thickness about twice the first layer  $\approx 37$  nm. It is important to point out that some layered and terraced droplets/cone-like structures consisting of more than two layers were observed, with each layer having a thickness from 22 to 37 nm. The APT  $\approx 13$  nm thin film (Figure A1c), exhibits a dendritic layer at the polymer-substrate interface, along with thicker layer islands formed on top. The height profile (Figure A1d) taken across the image of Figure A1c, shows that the thickness of the bottom layer is around 22 nm, while the thicker layer on top has a thickness again about double and of around 39 nm. In Figure A1e, the AFM image presents the typical morphology formed of the thicker film of  $\approx 41$  nm in which the first layer at the polymer-mica interface has covered a bigger surface than the previous films. The first layer is about 24 nm thick. The cone-like structures are more frequent than in the other two films. The height profile presented at Figure A1f shows that the thickness of the first layer is  $\approx 24$  nm, while the subsequent layers at the cone-like structures have thickness  $\approx 41$  nm.

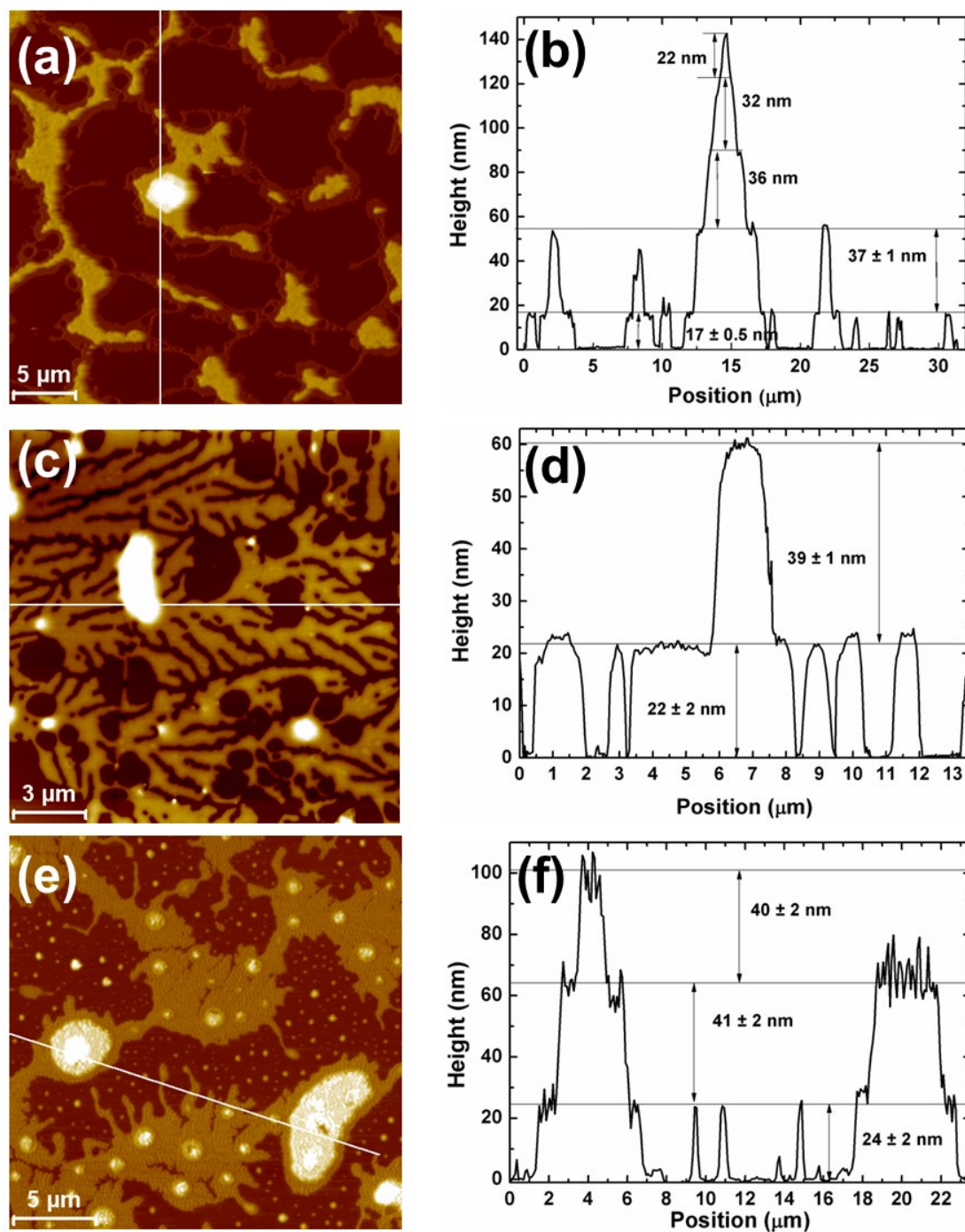


Figure A1 (a, c and e) Typical AFM height images for the PI-*b*-PEO block copolymer with  $f_{\text{PEO}} = 0.32$  of the (a) 7 nm film, (c) 13 nm film and (e) 41 nm film; (b, d and f) the corresponding height profiles indicated with the white lines in the AFM images.

**PI-*b*-PEO block copolymer with  $f_{\text{PEO}} = 0.49$ .** Figure A2 presents the morphologies for the symmetric case of our diblock copolymer for APT  $\approx 7$ , 13 and 41 nm thin films. A dendritic layer was formed over mica surface in the case of the apt  $\approx 7$  nm film (Figure A2a). Above this layer several thicker layer islands spread in some areas of the film. A height profile (Figure A2b) shows that the thickness of the dendritic layer is around 10 nm, while the islands thickness is around 24 nm. The APT  $\approx 13$  nm film formed a flat layer on top of the mica substrate with several thicker structures on top (Figure A2c). Line-scan profile across the image of Figure A2c reveals that the thickness of the first layer is  $\approx 14$  nm and the thickness of each layer on top is  $\approx 25$  nm (Figure A2d). In APT  $\approx 41$  nm film, a much more extensive layer has been formed (full coverage) directly on top of the mica substrate. On top of this layer, a wide and thicker layer was formed followed by another layer (islands) in some locations. In Figure A2e, we present an area in which the mica substrate is visible at the bottom of the film through a small hole in the monolayer, in order to measure the thickness of the monolayer. These areas are scarce. According to the height profile (Figure A2f) the thickness of the first layer is around 15.5 nm, while the thickness of the layers above is  $\approx 28$  nm.

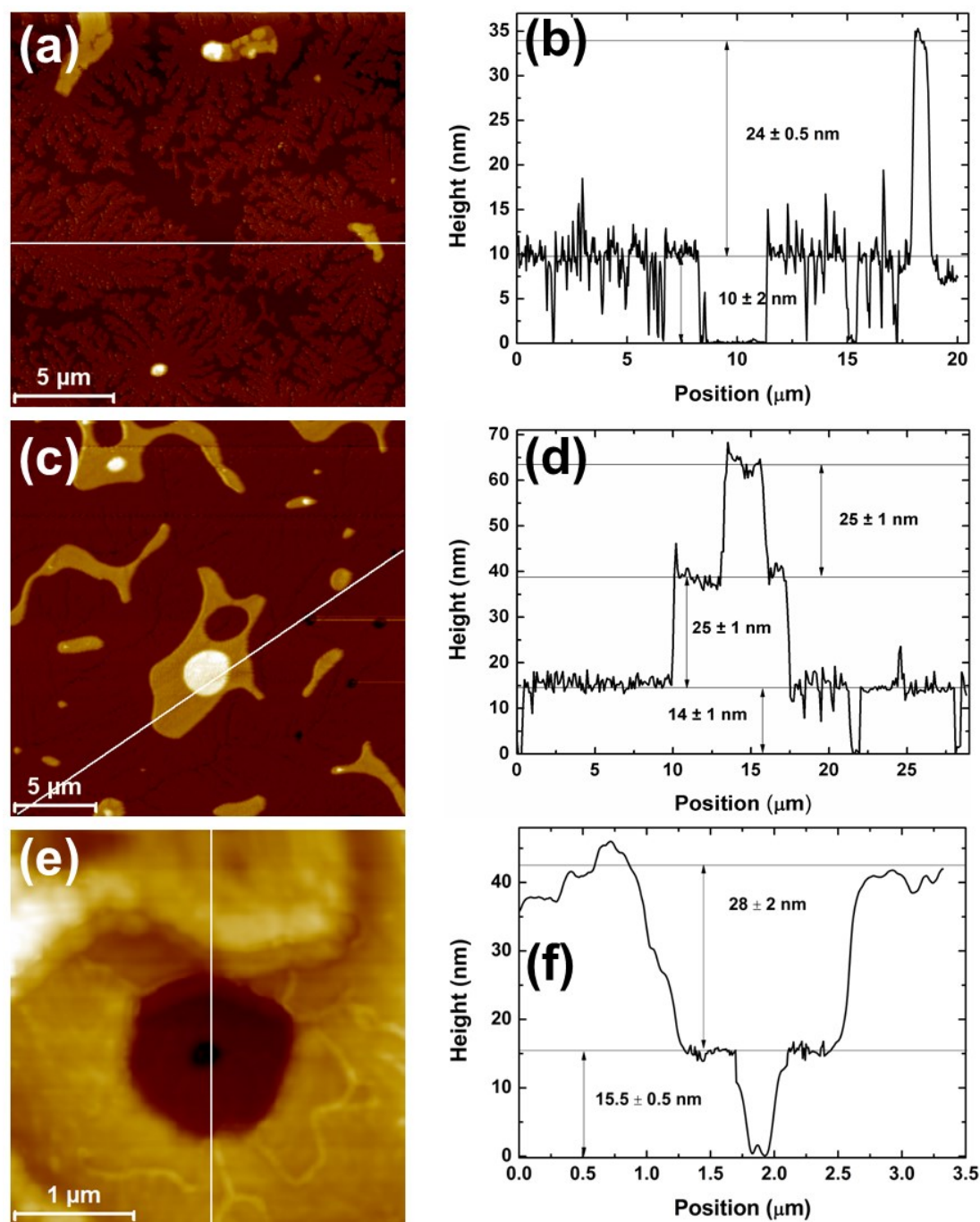


Figure A2 (a, c and e) Typical AFM height images for the PI-*b*-PEO block copolymer with  $f_{\text{PEO}} = 0.49$  of the (a) 7 nm film, (c) 13 nm film and (e) 41 nm film; (b, d and f) the corresponding height profiles indicated with the white lines in the AFM images.

PI-*b*-PEO block copolymer with  $f_{\text{PEO}} = 0.66$ . Figure A3a shows an AFM image of the APT  $\approx 7$  nm film with  $f_{\text{PEO}} = 0.66$ . A dendritic layer was formed across

---

the mica substrate. In some areas, thicker structures were observed on top of the first layer. According to the height profile (Figure A3b) taken across the image of Figure S3a, the thickness of the dendritic layer is around 8 nm, while the thickness of the thicker layer above is around 24 nm. Furthermore, Figure A3c presents the morphological behaviour of the APT  $\approx$  13 nm film with  $f_{\text{PEO}} = 0.66$ . The morphology is mainly characterised by two layers formed over the mica substrate. The bottom layer has a dendritic morphology. Some thicker layers (usually one or two) were developed on top of the dendritic layer. Height profile (Figure A3d), reveals that the dendritic layer has a thickness of  $\approx$  10 nm, while the layer on top have thickness of  $\approx$  27 nm. In Figure A3e, we present an AFM image from an area where the bottom (dendritic layer) of the APT  $\approx$  41 nm film with  $f_{\text{PEO}} = 0.66$  is visible and it is not as dense so that its thickness can be measured. The line scan profile (Figure A3f), shows that the bottom layer has a thickness of around 15 nm and the layer formed above has a thickness of around 30 nm.



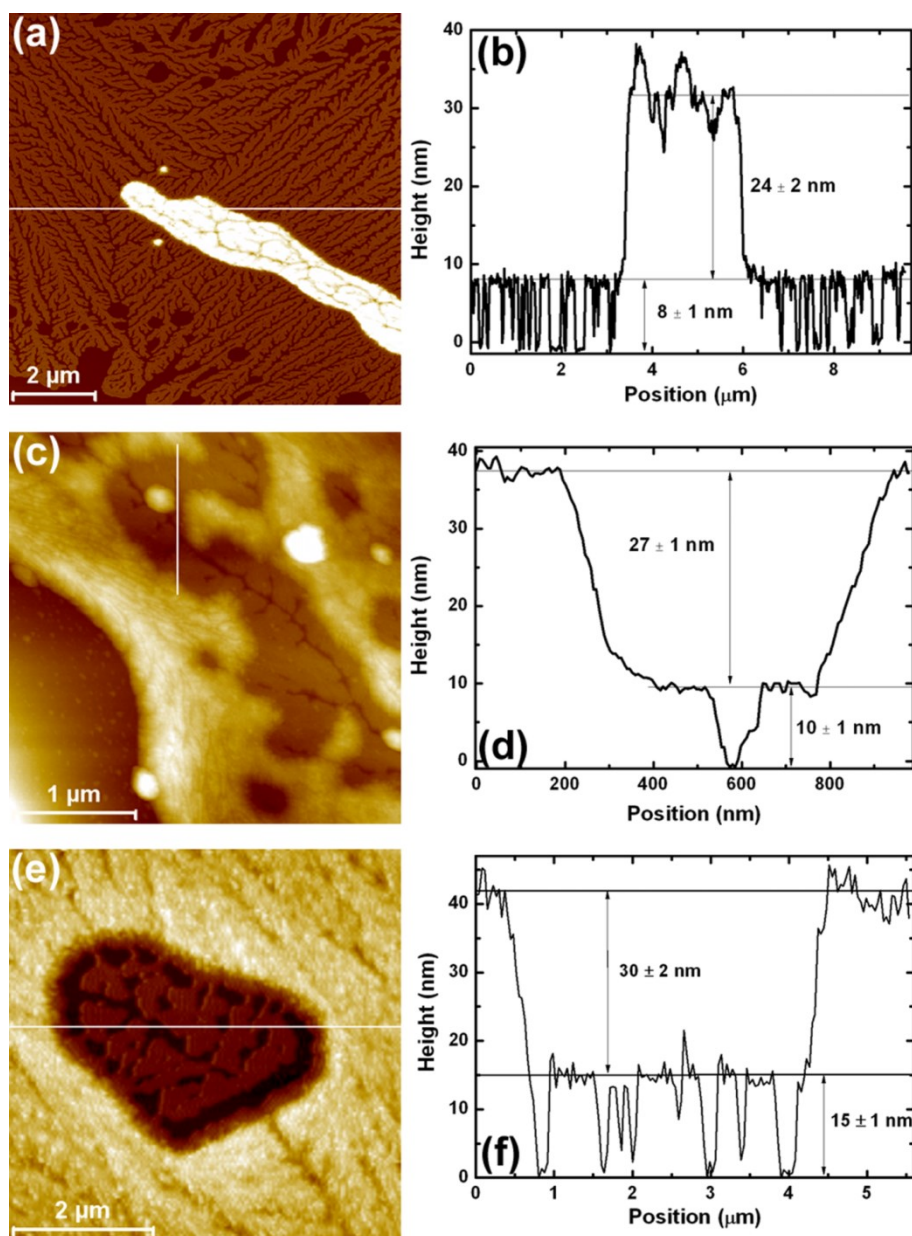


Figure A3 (a, c and e) AFM height images for the PI-*b*-PEO block copolymer with  $f_{\text{PEO}} = 0.66$  of the (a) 7 nm film, (c) 13 nm film and (e) 41 nm film; (b, d and f) the corresponding height profiles indicated with the white lines in the AFM images.

**PEO 8 kg/mol homopolymer thin films.** Figure A4 presents AFM images of the typical morphology of PEO 8 kg/mol (PEO8K) thin films from two concentrations  $10^{-3}$  g/g and  $2 \times 10^{-3}$  g/g, along with the corresponding height

profiles. The typical morphology for the PEO8K thin film from  $10^{-3}$  g/g is characterised by the formation of crystallized islands in a star-like morphology (Figure A4a). Height profile taken across the AFM image revealed that the average thickness of the star-like structures is 6.5 nm (Figure A4b). Furthermore, the morphology of PEO8K from  $2 \times 10^{-3}$  g/g is characterised from the formation of a layer with several fractal structures (Figure A4c). Height profile across the layer showed that the average thickness of the layers is 6.5 nm.

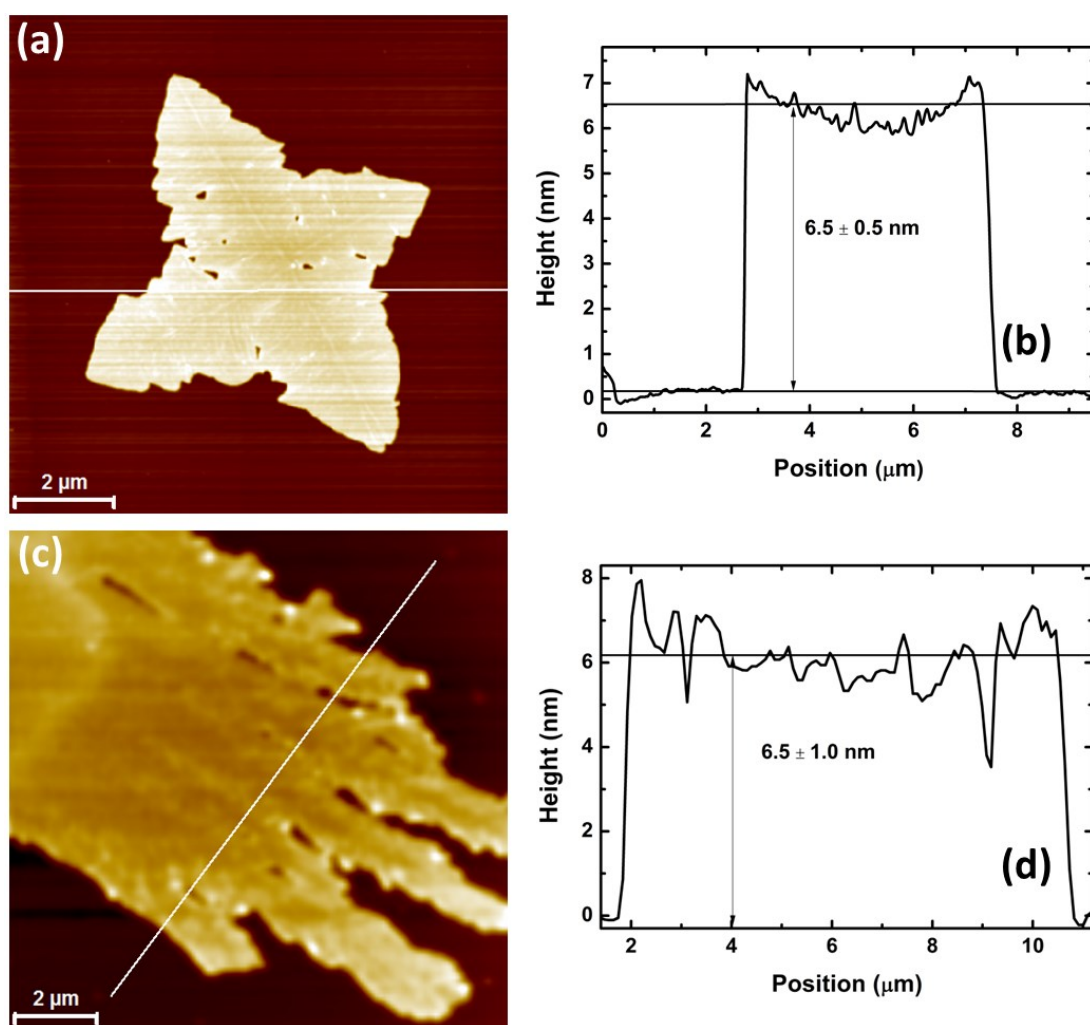


Figure A4 (a) (c) AFM topography images and the (b) (d) corresponding height profiles of PEO (8 kg/mol) homopolymer thin films from (a)  $c = 10^{-3}$  g/g and (b)  $c = 2 \times 10^{-3}$  g/g.

**PEO 14 kg/mol homopolymer thin films.** Figure A5 presents AFM images of PEO 14 kg/mol (PEO14K) thin films from two concentrations  $10^{-3}$  and  $2 \times 10^{-3}$  g/g, along with the corresponding height profiles. The typical morphology for the PEO14K from  $10^{-3}$  g/g is characterised by the formation of dendrite structures on top of the mica (Figure A5a). Height profiles across the dendritic structure showed that its thickness is  $\sim 7$  nm (Figure A5b). In addition, more frequent (compared with the previous case) dendrite structures were formed observed in the morphology of PEO14K thin films from  $2 \times 10^{-3}$  g/g solution concentration (Figure A5c). Height profiles across the image revealed that the thickness of the structure formed on mica is 6.2 nm (Figure A5d).

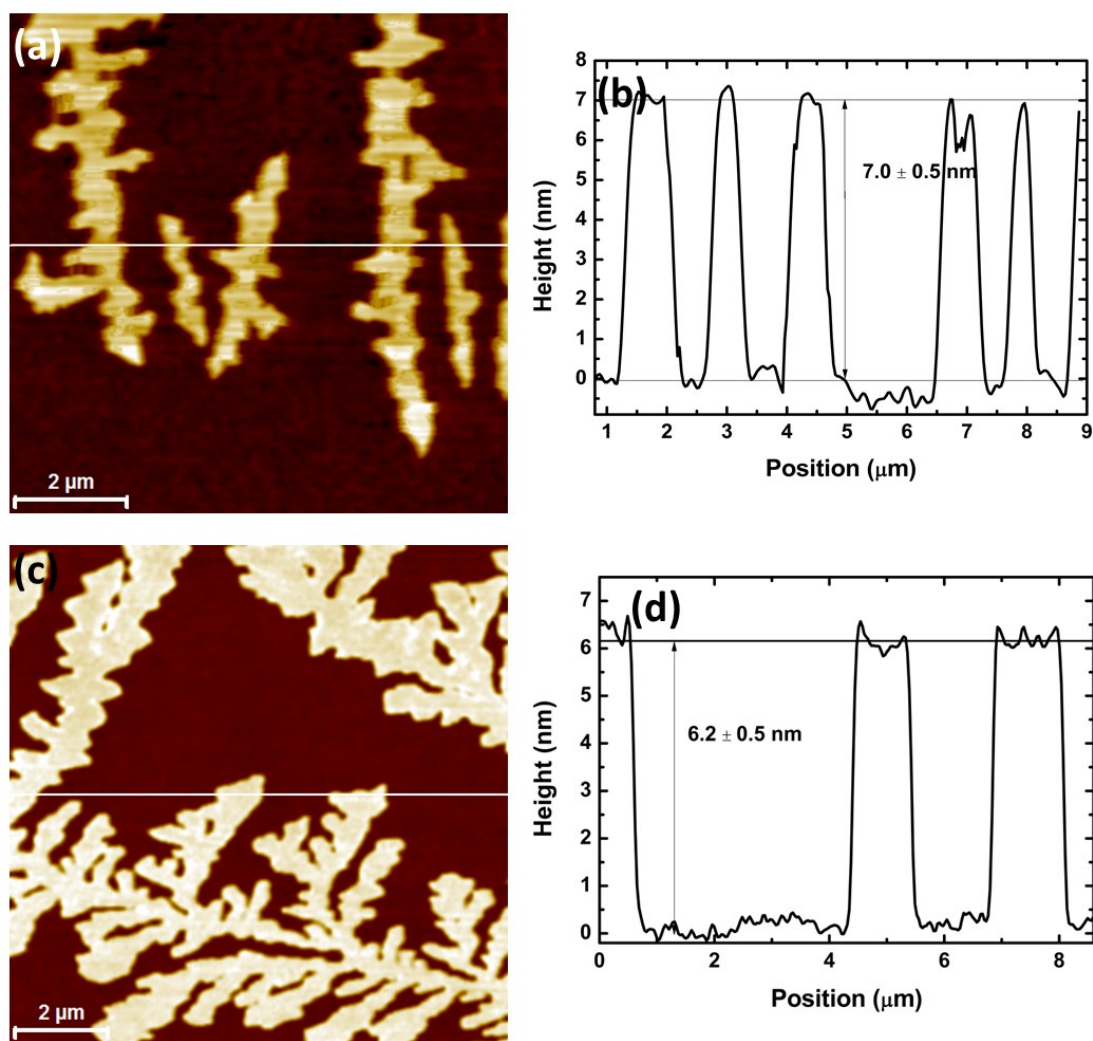
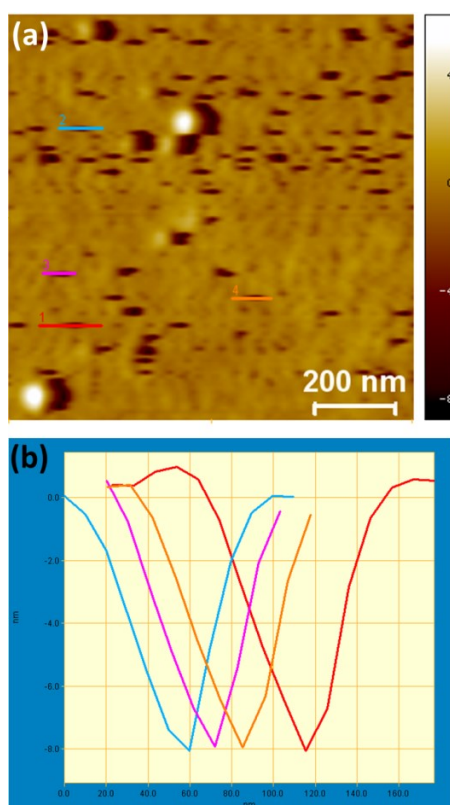


Figure A5 (a) (c) AFM topography images and the (b) (d) corresponding height profiles of PEO (14 kg/mol) homopolymer thin films from (a)  $c = 10^{-3}$  g/g and (b)  $c = 2 \times 10^{-3}$  g/g.

### **Appendix B: Cross-Section Analysis of TFB thin film**

Figure B1a presents the typical morphology of the TFB thin film, spin cast on mica. The morphology is characterised by the formation of a relatively soft layer, with several holes. In the cross sectional analysis of Figure B1b, it is shown that the thickness of the holes is  $\sim 8$  nm. We should note that the shape of the holes and their size, correspond to the characteristic shape and size of the AFM tip used for imaging (RTESP Bruker cantilevers, with nominal tip radius 8 nm).



**Figure B1 (a) Typical AFM image of TFB polymer thin film, spin-coated at 4,000 rpm for 90 seconds; (b) cross sectional analysis of the holes observed at the top surface of the corresponding film.**

---

**Appendix C: Publications, Talks and Presentations based on the present PhD work.**

- “Conjugated Polymer Blend /Quantum Dot Nanoparticle Composites: Thin Film Morphology”, Michail Kalloudis, Marco Bigatti, Joachim Loos Paul Clegg and Vasileios Koutsos. In writing stage for publication for submission to the *Journal of American Chemical Society (JACS)*
- “Thin Films of Poly(isoprene-*b*-ethylene Oxide) Diblock Copolymers on Mica: An Atomic Force Microscopy Study”, Michail Kalloudis, Emmanouil Glynos, Stergios Pispas, John Walker and Vasileios Koutsos. *Langmuir*, 2013, 29, 2339-2349.
- “Amphiphilic Diblock Copolymer Nanostructures on Hydrophilic Surfaces Studied by Atomic Force Microscopy”, Michail Kalloudis, invited talk in European Microscopy Congress (EMC), July 2010, London, UK
- “Amphiphilic Diblock Copolymer Nanostructures on Mica Surfaces studied by Atomic Force Microscopy”, Michail Kalloudis, Emmanouil Glynos, Stergios Pispas, John Walker and Vasileios Koutsos. Poster presentation in the 6<sup>th</sup> International Conference on Nanosciences and Nanotechnologies, Thessaloniki, Greece (13-15 July 2009).
- “Study of Phase Separation in Ultrathin Films of F8BT:TFB Conjugated Polymer Blends by Atomic Force Microscopy”, Michail Kalloudis, Paul Clegg and

Vasileios Koutsos. Poster presentation in Scanning Probe Microscopy Congress, Edinburgh, UK, (22-23 June 2011).

- “Study of Phase Separation in Ultrathin Films of Conjugated Polymer Blends by Atomic Force Microscopy”, Michail Kalloudis. Poster presentation in Bruker Scanning Probe Microscopy Conference and User Meeting, Manchester, UK, (22-23 November 2011).